Infrared Spectroscopy of Molecules in the Gas Phase

by

Keqing Zhang

A thesis

presented to the University of Waterloo

in fulfilment of the

thesis requirement for the degree of

Doctor of Philosophy

in

Chemistry

Waterloo, Ontario, Canada, 1997

The University of Waterloo requires the signatures of all persons using or photocopying this thesis. Please sign below, and give address and date.

Abstract

Fourier transform infrared spectroscopy is applied to the studies of several very different molecular systems. The spectra of the diatomic molecules BF, AlF, and MgF were recorded and analyzed. Dunham coefficients were obtained. The data of two isotopomers, ^{11}BF and ^{10}BF, were used to determine the mass-reduced Dunham coefficients, along with Born-Oppenheimer breakdown constants. Parameterized potential energy functions of BF and AlF were determined by fitting the available data using the solutions of the radial Schrödinger equation.

Two vibrational modes of the short-lived and reactive BrCNO molecule were recorded at high resolution. Rotation-vibration transitions of the fundamental bands of both isotopomers ^{79}BrCNO and ^{81}BrCNO were assigned and analyzed. From the rotational constants, it was found that the Br-C bond length in BrCNO anomalously short when a linear geometry was assumed. This may indicate that BrCNO is quasi-linear, simulating the parent HCNO molecule.

The emission spectra of the gaseous polycyclic aromatic hydrocarbon (PAH) molecules naphthalene, anthracene, pyrene, and chrysene were recorded in the far-infrared and mid-infrared regions. The assignments of fundamental modes and some combination modes were made. The vibrational bands that lie in the far-infrared are unique for different PAHs and allow discrimination among the four PAH molecules. The far-infrared PAH spectra, therefore, may prove useful in the assignments of unidentified spectral features from astronomical objects.

Acknowledgements

I would like to extend my thanks to my supervisor Dr. Peter Bernath for his scientific inspiration, patience, and constant encouragement throughout the course of this research. It was a great pleasure to work with Dr. Bujin Guo on many projects.

I would also like to thank Dr. Nick Westwood and Dr. Tibor Pasinszki for providing expertise and helping to set up the experiments on nitrile oxides.

Finally, I would like thank Pina Colarusso, Zulf Morbi and Chunfeng Zhao for their collaboration and enlightenment.

For my wife Sue

and

my mother and father

Contents

List of Figures

List of Tables

Chapter 1

Introduction

Molecular spectroscopy is a branch of science in which the interactions of electromagnetic radiation and matter are studied. The aims of these studies are to elucidate information on molecular structure and dynamics, the environment of the sample molecules and their state of association, interactions with solvents, and many other topics. The results from spectroscopy have, therefore, played an important role in many disciplines of science, including biochemistry [1], environmental research [2], chemical dynamics [3], astrophysics [4, 5], and atmospheric chemistry [6, 7].

The interaction of the radiation with the molecules is usually expressed in terms of a resonance condition, which implies that the energy difference between two stationary states in a molecule must be matched exactly by the energy of the photon:

$$\Delta E_{molecule} = (h\nu)_{photon} = (hc\sigma)_{photon}, \tag{1.1}$$

where h is the Planck constant, c is the speed of light in vacuum, ν is frequency and σ is the wavenumber which has the unit cm^{-1}. This view of the interaction between light and matter is, however, rather cursory, since radiation interacts with matter even when its wavelength is different from the specific wavelength at which a resonance occurs. These off-resonance interactions between electromagnetic radiation and matter give rise to well-known phenomena such as the Raman effect [8]. The interactions between molecules and photons determine the intensities, widths, and shifts of spectral lines and the intensity and spectral distribution of continuous radiation [9].

Molecular spectroscopy is usually classified by the wavelength range of the electromagnetic radiation, for example, infrared spectroscopy and microwave spectroscopy. This dissertation mainly covers some aspects of infrared spectroscopy. Although vibration-rotation transitions in the infrared are relatively weak [10], when compared with electronic transitions, all molecules except homonuclear diatomic molecules have at least one electric-dipole allowed infrared transition [11]. The universal applicability of infrared spectroscopy is the most attractive property of this spectroscopic technique.

Infrared spectroscopy, particularly emission spectroscopy, faces another serious challenge: blackbody radiation at room temperature. This radiation has a maximum around 1000 cm^{-1}, resulting in a natural elevation of the noise level in infrared spectra. Furthermore, high power, widely tunable lasers are not available to infrared spectroscopy. It was also true that infrared detectors and optics were in general inferior to those accessible in other spectral regions. The demand from

many practical applications of infrared technology, in particular, defense related applications, has changed this situation. Infrared detectors now have quantum efficiencies as high as 70% [12]. In the meantime, the quality of infrared materials and optical coatings has made significant advances as well. The room temperature blackbody radiation can be greatly reduced by the use of cold band pass filters. The application of cold apertures can be used to limit the thermal background radiation. As a result, new techniques of infrared spectroscopy have been developed, and existing techniques have been improved dramatically.

Today, infrared spectroscopy is a discipline in its own right. Spectroscopy is the bridge that connects advanced experimental results to the sophisticated theoretical interpretations of molecular structure. The combination of experiment and theory is very helpful in the synthesis, identification and characterization of new molecules and complex molecules. For small molecules, high resolution spectroscopy is the ideal tool for the determination of geometry. The spectra of small stable molecules at room temperature have been well studied and understood. One new area of research is the study of the spectra of these stable molecules at high temperature, where the excited vibrational levels have very high energy [13]. As the experimental techniques have improved, the high resolution infrared spectra of free radicals [14–16], ions [17] and high temperature molecules [10] have also been recorded. These transient molecules usually exist in low concentrations and in extreme environments. The detection of their spectra often forces the instrumentation to the limits of sensitivity.

Another area that requires significant improvement is far-infrared spectroscopy.

Far-infrared spectra are easily contaminated by the pure rotational transitions of water vapor in the atmosphere. The blackbody radiation often overwhelms the weak far-infrared signals originating from the molecules. Furthermore, far-infrared detectors are the least sensitive ones among the infrared detectors. Despite all of these difficulties, considerable amount of spectroscopic data have been collected in the far-infrared region. Chemists use the far-infrared spectra to study weak chemical bonds. They also use them for studies of molecules with heavy atoms or long chains because many of the infrared bands of these molecules are in the far-infrared region.

The infrared spectroscopic techniques are applied to many different areas. One of the most practical applications is based on the correlation between infrared spectra and chemical functional groups [18]. Group frequencies can be useful aids in identifying an unknown compound by comparison of the same group frequency in a molecule of closely related structure. Alternatively, because of the large number of possible normal vibrational modes for a molecule of even modest size, the infrared spectrum provides a useful fingerprint which is nearly unique for a given molecule.

Infrared spectra also contain quantitative information. The infrared spectroscopic technique is widely used in analytical chemistry [19]. Since spectroscopic techniques are not invasive, they are ideal for remote sensing, such as monitoring the temperature profile of the atmosphere and "greenhouse" gases from space [20]. The combination of gas chromatography [21] and Fourier transform infrared spectroscopy has proven to be a powerful technique for analyzing complex mixtures quickly and accurately. Obtaining the infrared spectra of biological samples is

a new but rapidly expanding field. Infrared spectral differences between healthy and cancerous human colon and cervical cells have been discovered [22]. The infrared spectra of these cells have also been used to help determine the biochemical difference between healthy and malignant cells, and to help model the chemical differences between the DNA in normal and malignant tissue.

The high resolution spectra reported in this study were recorded on a state-of-the-art Fourier transform spectrometer. The development of the Fourier transform spectrometer, is combined with the continuing improvements in infrared detectors. This has opened up the possibility of applying high resolution spectroscopy to many diverse chemical systems. Fourier transform spectrometers are now commonly used for both low and high resolution work. Another advantage of Fourier transform spectroscopy, as illustrated in this thesis, is wide spectral coverage.

1.1 Absorption vs. Emission Infrared Spectroscopy

Traditionally, molecules are studied by means of absorption spectroscopy in the infrared region. In absorption spectroscopy, the light source is directed through a cell containing the sample of interest, and the resulting intensities of the different transitions are measured. The magnitude of an absorption is given by Beer's law,

$$A = -\ln(\frac{I}{I_0}) = \epsilon(\nu)\, c\, l, \tag{1.2}$$

where I refers to the intensity of the light falling on the detector, I_0 is the intensity of the reference beam, $\epsilon(\nu)$ is the molar absorptivity coefficient at a given frequency

ν, c is the concentration of the absorbing material, and l is the path length of light in the cell containing the absorbing material.

For the study of spectra of transient molecules, absorption spectroscopy becomes difficult, partly because transient species often exist at temperatures which are comparable to or higher than the temperature of the absorption source. Infrared emission spectroscopy has emerged as a wonderful tool to study molecules at high temperatures. When one examines the spontaneous emission process, the rate is determined by the Einstein A factor (in s^{-1}), given by the equation [23]

$$A_{ij} = 3.137 \times 10^{-7} \nu^3 |\mu_{ij}|^2, \tag{1.3}$$

where μ_{ij} is the transition dipole moment matrix element in debyes and ν is the transition frequency in cm^{-1}. It is clear that emission rates favor high frequency transitions from the above expression (Equation (1.3)). This is one of the reasons that in the visible and ultraviolet regions of the spectrum, emission spectroscopy is the method of choice. Infrared transition dipole moments are typically 0.1 debyes, while electronic transition dipole moments are on the order of 1 debye. Although infrared transitions are relatively weak, infrared experiments are possible, and a number of high temperature molecules have been recorded in emission.

1.2 Diatomic Molecules

Once a molecular system is observed, the challenge of spectroscopy becomes the extraction of physically relevant information from the spectral line positions, widths,

and intensities. From the recorded line positions, it is possible to model the energy level pattern of the molecular system that is accessed by the experiment. In addition, more direct physical information, such as bond lengths, bond angles and moments of inertia, may be calculated from the line positions.

Diatomic molecules are the simplest molecular systems. The analysis of their spectra has been crucial to the development of theories of molecular structure and chemical bonding [24]. Consequently, many of the prototypical models first developed to describe the vibrational spectroscopy of diatomic molecules have been extended to the study of polyatomic molecules and transient species [25,26].

High resolution spectroscopy has also been critical in the development of theoretical foundation of molecular structure and in the determination of the limitations of these model theories. A good example of the interaction between experimental spectroscopy and theories of chemical structure and bonding is the study of the breakdown of the Born-Oppenheimer description of molecular behavior.

The knowledge of the pattern of rotation-vibration energy levels has several practical and theoretical uses. The most dominant practical use of high resolution spectroscopy is the identification of molecules in various environments. For example, transient molecules, by definition, exist in extreme conditions such as high temperatures and low pressures. Identification of transient molecules by non-spectroscopic means is usually uncertain or not possible. High resolution spectroscopy is often utilized in identification of radicals in flames, the upper atmosphere, and space.

In 1927, Born and Oppenheimer formulated the mathematical separation of

nuclear and electronic motion of a molecular system [27]. The Born-Oppenheimer approximation has electrons moving around fixed nuclei which act as point charges. The neglect of the kinetic energy of the nuclei provides a means to solve the electronic Schrödinger equation, which is otherwise soluble for only a limited number of model problems. The inability of the Born-Oppenheimer solution to the vibration-rotation Schrödinger equation to adequately explain some physical behavior was noted in 1936, shortly after the discovery of deuterium [28]. The nature of its limitations has been well studied [29,30] and mathematically described. Thus the Born-Oppenheimer approximation still plays a crucial role in the development of models of molecular systems.

An important and useful consequence of the Born-Oppenheimer approximation is the internuclear potential energy function [31]. The potential energy function may be thought, in a simplistic way, as describing the behavior of a chemical bond as a function of internuclear distances and angles. A high quality potential energy function will provide a prediction of positions, and with a dipole moment function, intensities of experimentally unobserved transitions. In addition, other experimental observables, like scattering data and transport properties, can be determined from potential energy functions which are derived from spectroscopic data. Potential energy functions can be determined from the inversion of spectroscopic constants to a theoretical model, or from the direct fitting of spectral data to a potential energy function. Potential energy functions can also be determined from ab initio calculations.

Two methods, the Dunham model [32] and the parameterized potential model

[33–36], were used in the reduction of the diatomic data recorded in this study. The Dunham model was developed in 1932, and has been used in the fitting of rotation-vibration data. There are numerous methods used to improve and modify Dunham's original work. In this work, the mass-independent Watson expression with the high order terms constrained, was applied to determine vibrational coefficients. The parameterized potential energy model was also employed. This model is based on the direct fitting of spectral data to a parameterized potential using the radial Schrödinger equation.

1.3 Polyatomic Molecules

The infrared spectra of many, stable and unstable, small molecules have been examined and reexamined. Good infrared spectra are also available for larger molecules with 10 to 20 atoms. In general, as the symmetry of molecules decreases, both the quality and quantity of infrared spectra decrease. One of the trends in modern infrared spectroscopy is toward studying larger molecules, such as polycyclic aromatic hydrocarbon molecules [37,38] and biochemical compounds [39], for which the interpretation of infrared spectra is more difficult.

The structure and spectra of polyatomic molecules are much more complicated than those of diatomic molecules. The number of degrees of freedom in an n-atom molecule is $3n$. When translational and rotational degrees of freedom are excluded, there are $3n - 6$ vibrational modes for a nonlinear molecule, and $3n - 5$ vibrational modes for a linear molecule. It is possible to choose a set of $3n - 6$ (or $3n - 5$ in the linear case) coordinates in such a way that each equation of motion

involves one coordinate only. Then, the vibrational Schrödinger equation can thus be approximately separated into $3n - 6$ independent equations in the same way. Each equation describes a normal mode of vibration, which is a simple harmonic oscillator with a characteristic frequency. The actual motion of each nucleus is a complicated superposition of all the normal modes. In a simple molecule, it is often possible to regard each normal mode as representing either a change in length of the bond between one pair of atoms, i.e. stretching vibration, or a change in the angle between two bonds, i.e. bending vibration. In a more complex molecule, the normal modes may describe vibration either of the whole molecular skeleton, or of particular groups of atoms such as OH and CH_3. Vibrations of the second type are characteristic of the group and almost independent of the particular molecule to which it is attached.

The vibrational frequencies of polyatomic molecules are in the same energy range as those of diatomic molecules. The vibrational bands have a rotational structure as do diatomic molecules. Indeed the band structure of small polyatomic molecules is rather similar to that of diatomic molecules. On the other hand, since large molecules tend to have large moments of inertia and hence small rotational constants, the separation of the rotational lines may become comparable with their intrinsic width, resulting in a continuum-like spectrum. The spectra may be further complicated by the overlapping of different vibrational modes.

Because of their complexity, the interpretation and assignment of vibrational spectra of polyatomic molecules is a difficult and time-consuming process. One very simple approach to describe the molecular vibrations of large organic molecules and

biological macromolecules is to use group frequencies and qualitative correlations. This is certainly worthwhile but has to be viewed as strictly a qualitative tool for structural chemistry. Attempts to corroborate vibrational interpretations on such large systems by normal mode calculations are usually indeterminate since the number of force field constants usually exceeds the number of known vibrational frequencies. A much more rigorous approach is to utilize detailed isotopic data for a vibrational assignment, followed by a thorough normal mode calculation. Enormous effort is required since numerous isotopomers have to be synthesized and analyzed.

Chapter 2

Fourier Transform Infrared Spectroscopy

There are two major types of instruments which are widely used in modern infrared spectroscopy. Diode laser spectrometers [40–42] are mainly used for high resolution spectroscopy, while Fourier transform spectrometers [43–45] are used for both high and low resolution spectroscopy. For high resolution studies, the diode laser provides the spectral brightness necessary for remarkably high sensitivity and narrow spectral line width. Tunable semiconductor diodes supply infrared radiation from 360 to 3500 cm^{-1} [46]. Diode laser spectroscopy is, however, limited by practical difficulties. A single diode can only cover a spectral region of 50 to 100 cm^{-1}, and within that range the coverage is around 30%. Consequently the spectrometer has a very narrow tunable range. The high sensitivity of diode lasers is responsible for their wide-spread use in spectroscopy [47], but the lack of complete spectral coverage is a serious and frustrating defect. Assignments of transitions between rotational

levels in the spectra of new molecules, particularly asymmetric top molecules, are difficult if only a partial spectrum is available. In addition, diode spectrometers have no inherent means of calibration.

Fourier transform spectrometers are less sensitive, but have several inherent advantages that make them ideal for many applications. They can cover a wide spectral range, from far-infrared to near ultraviolet region [45]. By employing He-Ne lasers to control sampling of light signal accurately, Fourier transform spectrometers have built-in high precision frequency calibration. Resolutions ranging from a few wavenumbers to 0.002 cm^{-1} are routinely available, and Fourier transform spectrometers can record samples in gas, liquid or solid phase under a variety of experimental conditions. Although the light source used with Fourier transform spectrometers is inferior to that of diode laser spectrometers, the wide and complete spectral coverage, and a precise internal frequency calibration ensure their important role in spectroscopy [48,49].

2.1 The Michelson Interferometer

The development of Fourier transform spectroscopy is based on the two-beam interferometer that was originally designed by Michelson in 1891 [50,51]. A diagram of the Michelson interferometer is shown in Figure 2.1. The Michelson interferometer consists of four arms. The first arm contains a source of light, the second arm contains a stationary mirror, the third arm contains a movable mirror, and the fourth arm is open. At the intersection of the four arms is a beamsplitter, which is designed to transmit half the radiation that is incident upon it, and to reflect

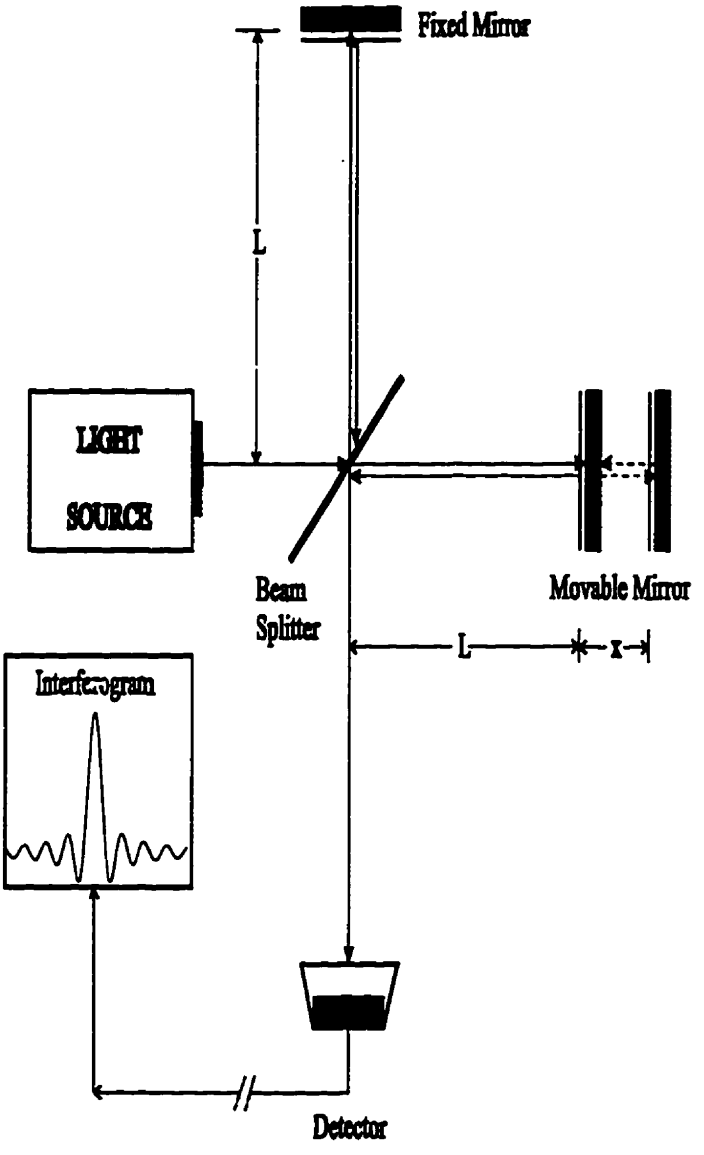

Figure 2.1: The schematic of the Michelson interferometer

half of it. As a result, the light transmitted by the beamsplitter strikes the stationary mirror, and the light reflected by the beamsplitter strikes the movable mirror. After reflecting off their respective mirrors, the two light beams recombine at the beamsplitter, and the recombined beam is directed to the detector.

If the movable mirror and stationary mirror are the same optical distance from the beamsplitter, the distance traveled by the light beams that reflect off these mirrors is the same. This condition is known as zero path difference (ZPD). In a Michelson interferometer, an optical path difference is introduced between the two light beams by translating the moving mirror away from the beamsplitter. The light beam that reflects off the moving mirror will travel further than the light beam that reflects off the stationary mirror. The distance that the mirror is moved from zero path difference is called the mirror displacement x. Since the light beams travel back and forth from the mirrors, the extra distance is twice mirror displacement, and is called optical path difference (OPD).

The variation of light intensity with optical path difference is measured with a detector as an interferogram, which is a plot of light intensity as a function of x. To record a complete interferogram, the moving mirror is translated back and forth once. This is known as a scan. The interferogram [45] is mathematically expressed as

$$I(x) = \int_{-\infty}^{\infty} B(\sigma) \cos 2\pi\sigma x \, d\sigma, \tag{2.1}$$

where $B(\sigma)$ is the flux density at wavenumber σ, x is the mirror displacement, and

$I(x)$ is the interferogram. The inverse Fourier transform is

$$B(\sigma) = \int_{-\infty}^{\infty} I(x) \cos 2\pi\sigma x \, dx. \tag{2.2}$$

The value of x is determined by the product of the constant velocity of the moving mirror and the time since the initial mirror displacement of the scan. The mirror velocity and time are electronically controlled to high precision with the aid of a single-mode He-Ne laser. This precision in the control of mirror displacement provides a built-in frequency calibration of the spectrum. The spectrum, which is a plot of light intensity as a function of frequency, is obtained by calculating the Fourier transform of the interferogram (Equation (2.2)).

2.2 Advantages of Fourier Transform Spectroscopy

Michelson was aware of the potential use of his interferometer to obtain spectra, and manually measured many interferograms [52]. Unfortunately, the time consuming calculations required to convert an interferogram into a spectrum made using an interferometer to obtain spectra impractical. It was the invention of computers and the Fast Fourier Transform algorithm that established the basis for Fourier transform spectroscopy [53].

The ultimate performance of any spectrometer is determined by measuring its signal-to-noise ratio (SNR). SNR is calculated by measuring the peak height of a feature in an infrared spectrum, and ratioing it to the level of noise at some baseline point nearby in the spectrum. Noise is usually observed as random fluctuations

in the spectrum above and below the baseline. For a given sample and set of conditions, an instrument with a high SNR will be more sensitive, and allow spectral features to be measured more accurately than an instrument with a low SNR.

There are two reasons why Fourier transform spectrometers are capable of achieving SNR significantly higher than dispersive instruments. The first advantage is called the multiplex or Fellgett advantage. It is based on the fact that light from the entire spectrum is detected at once, whereas in dispersive scanning spectrometers, only a small wavenumber range at a time is measured. The noise at a specific wavenumber is proportional to the square root of the time spent observing that wavenumber. If the dominant source of noise is from the detectors or the background, then the Fourier transform spectrometer will have a multiplexing advantage. The practical advantage of multiplexing is that a Fourier transform spectrometer can acquire a spectrum much faster than a dispersive instrument. The second advantage is called the throughput or Jacquinot advantage. It is based on the fact that the circular apertures in Fourier transform spectrometers allow a higher throughput of radiation than through the slits used in dispersive spectrometers. There are no slits to restrict the wavenumber range and to reduce the intensity of radiation. The detector, therefore, measures the maximum amount of light at all points during a scan.

The advantages of the Fourier transform spectrometer provide high resolution and good sensitivity. The maximum spectral resolution [12] of an interferometer is inversely proportional to the maximum OPD allowed,

$$\delta\sigma = \frac{0.6}{OPD}. \tag{2.3}$$

It follows that a Fourier transform spectrometer requires a large mirror displacement and accurate control over the moving mirror for recording high resolution spectra.

In an ideal interferometer, the light beam is a perfectly collimated cylinder, and all light rays are parallel to each other. In reality, the optics are not perfect, and the light beam shape is not a cylinder, but usually a cone. The light rays in a beam are not parallel, but form an angle to each other. This phenomenon is known as angular divergence. Because of angular divergence, light on the outside of the beam travels a different distance than light in the center of the beam. These light rays can interfere destructively with each other. Angular divergence increases with optical path difference because the light beam spreads out more the further it travels. Aperture size, therefore, provides a practical limitation on resolution. The achievable resolution [45] from an aperture of diameter d is given by the expression

$$\delta\sigma = \frac{\sigma d^2}{8F^2}, \tag{2.4}$$

where F is the focal length of the interferometer and σ is the wavenumber being analyzed.

The above equation exposes a serious challenge to the high resolution spectroscopist. The largest possible signal is obviously obtained through the use of a large aperture, while conversely, high resolution requires that a small aperture be used. The analysis of transient molecules, which are characterized by low concentrations and small signals, demands that the sensitivity factors be maximized. These factors apart from aperture size, are quality of the light source, efficiency of the beamsplitter, transmittance of the windows, and sensitivity of the detectors.

To obtain improvements in signal, often some sacrifice in resolution needs to be made in order to obtain a useful spectrum. The signal-to-noise ratio can also be improved by co-adding successively recorded interferograms.

2.3 The Bruker Spectrometer

The Bruker IFS 120 HR Fourier transform spectrometer, which has been used through this study, is one of the best and most versatile instruments of its kind available. Its design is optimized for spectroscopic measurements in the entire infrared region at either high or low resolution. By choosing different combinations of light sources, beamsplitters, windows and detectors, the instrument can achieve a resolution of better than 0.002 cm^{-1} in spectral range extending from the far infrared to the near ultraviolet (50 - 40 000 cm^{-1}).

The optical layout of the Bruker spectrometer is shown in Figure 2.2. Radiation from three water-cooled internal sources, or external sources for emission experiments, enters the Michelson interferometer through a circular aperture of a chosen diameter, ranging from 0.5 to 12.5 mm. The Bruker Michelson interferometer has a maximum optical path difference of approximately 4.8 meters, and thus a resolution limit better than 0.002 cm^{-1}. The position and speed of the movable mirror are controlled by a single mode stabilized He–Ne laser. The recombined beam leaves the beamsplitter and passes through an optical filter. The beam is then focused onto one of the available detectors. There are four internal detector positions. Among them, one is used to hold a liquid nitrogen-cooled InSb detector (1800 - 9000 cm^{-1}), and one is used to hold a liquid nitrogen-cooled HgCdTe (MCT) detector (800 -

2000 cm^{-1}). Two external detector positions are available. A liquid helium-cooled boron doped silicon (Si:B) detector (350 - 3000 cm^{-1}) and a liquid helium-cooled bolometer (10 - 360 cm^{-1}) can be mounted at the external positions. The lower limits of InSb, MCT and Si:B detectors are determined by the band gaps of the materials. The upper limits are determined by the start of the next detector. The response of the bolometer is flat over the entire spectral range, however, two cold filters inside the bolometer set the upper limits to be 200 and 360 cm^{-1}, respectively. The entire spectrometer can be evacuated to less than 0.02 Torr. The optical functions of the spectrometer and the collection, handling and output of data are controlled by a personal computer running the OPUS software program which is designed by Bruker.

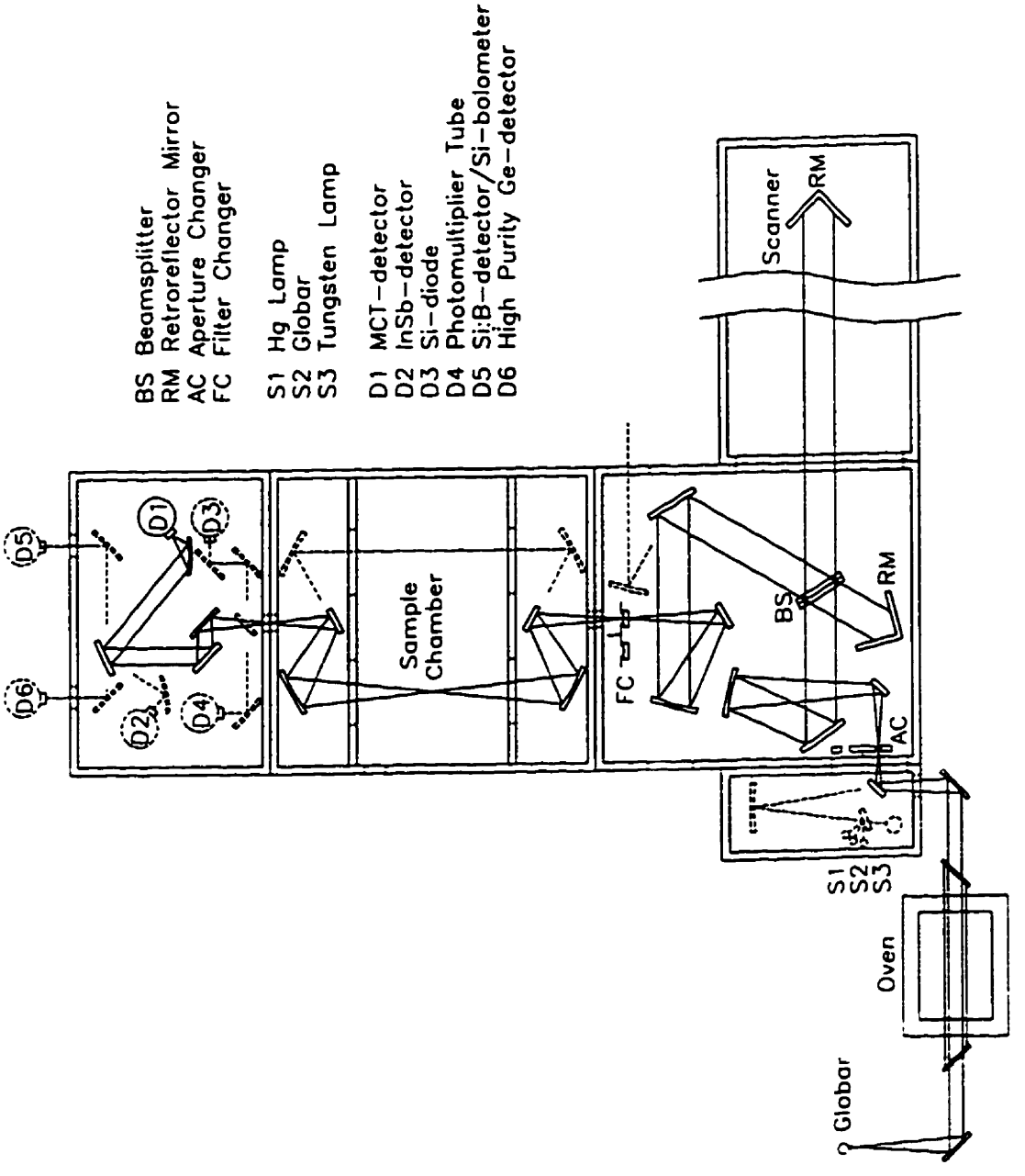

Figure 2.2: The optical layout of the Bruker IFS 120 HR Fourier transform spectrometer

Chapter 3

Infrared Spectroscopy of Diatomic Molecules

A large amount of information on the physical properties of molecular species can be obtained from their spectra. One main objective of spectroscopy is the extraction of concise representations of physically meaningful data from the large number of spectral line positions. The reduction of line positions to spectroscopic constants is accomplished through the use of theoretical models. The set of spectroscopic constants can serve as a compact representation of the experimental observations. A theoretical model can help to derive the structurally relevant information from experimental data, and predict energy levels for unobserved transitions to a certain degree of accuracy. The foundation of most theoretical models is the Born-Oppenheimer description of the molecular system. The use of the Born-Oppenheimer approximation greatly simplifies the Schrödinger equation.

3.1 The Born-Oppenheimer Approximation

The time-independent Schrödinger equation provides a quantum mechanical description of molecular systems:

$$\mathbf{H}\Psi(\{\mathbf{r}_i\},\mathbf{R}) = E\Psi(\{\mathbf{r}_i\},\mathbf{R}), \tag{3.1}$$

where **H** is the Hamiltonian, $\Psi(\{\mathbf{r}_i\},\mathbf{R})$ is the wavefunction, E is the energy, $\{\mathbf{r}_i\}$ is the set of position vectors of the ith electron, and **R** designates the position vectors of the nuclei. For a diatomic molecule, **R** is the vector between the nuclei. By solving the Schrödinger equation for the wavefunctions, all the physical properties of the molecular system can be calculated and interpreted. Unfortunately, the Schrödinger equation can only be solved analytically for simple systems.

The solution of the Schrödinger equation for molecular systems was facilitated by the Born-Oppenheimer description of molecular structure [27]. The Born-Oppenheimer approximation is based on the dynamical approximation that electrons are moving around fixed nuclei which act as point charges. Since the mass of an electron is much lighter than that of a nucleus, the speed of an electron is very large in comparison to the movement of a nucleus, so that the latter may be considered to be stationary. The motion of the nuclei can, therefore, be considered independently of the motion of the electrons.

The separability of nuclear and electronic motions dramatically diminishes the complexity of the mathematical solution of the Schrödinger equation. The total wavefunction can now be expressed as a product of separate nuclear and electronic

wavefunctions

$$\Psi(\{\mathbf{r_i}\}, \mathbf{R}) = \psi_n(\mathbf{R})\psi_e(\mathbf{R}; \{\mathbf{r_i}\}). \tag{3.2}$$

The total energy can be partitioned to

$$E = E_n + U(R), \tag{3.3}$$

where E_n is the nuclear energy and $U(R)$ is the electronic energy. The electronic wavefunction, $\psi_e(\mathbf{R})$ satisfies a unique Schrödinger equation which only represents the motion of electrons

$$\mathbf{H_e}\psi_e(\mathbf{R}; \{\mathbf{r_i}\}) = U(R)\psi_e(\mathbf{R}; \{\mathbf{r_i}\}). \tag{3.4}$$

It is noticed that U and ψ_e are functions of R, so a change in nuclear position results in a corresponding change in the electron charge distribution. The functional dependence of electronic energy on nuclear positions is called the potential energy of nuclear motion.

The solution of the electronic Schrödinger equation is used in the derivation of the nuclear Schrödinger equation. The mathematical procedure is the physical equivalent of stating that nuclear motion takes place in an average field of electron motion. The Schrödinger equation of the molecular system now can be expressed as

$$(\mathbf{T_n} + \mathbf{H_e})\psi_n(\mathbf{R})\psi_e(\mathbf{R}; \{\mathbf{r_i}\}) = E\psi_n(\mathbf{R})\psi_e(\mathbf{R}; \{\mathbf{r_i}\}). \tag{3.5}$$

After the Born-Oppenheimer approximation, the nuclear motion and electronic

motion are separated, the Schrödinger equation of nuclear motion is then

$$\mathbf{T}_n\psi_n(\mathbf{R}) = (E - U(R))\psi_n(\mathbf{R}). \tag{3.6}$$

The nuclear motion can be further separated into rotation and vibration. This is justified because vibration takes place on much shorter time scale than rotation does.

For a diatomic molecule consisting of atoms A and B, the nuclear Hamiltonian is

$$\mathbf{T}_n = \frac{P_A^2}{2M_A} + \frac{P_B^2}{2M_B}, \tag{3.7}$$

where M_A and M_B are the nuclear mass of atoms A and B respectively, and P_A and P_B are the momenta of the nuclei of atoms A and B respectively. The electronic Hamiltonian is

$$\mathbf{H}_e = \sum_i \frac{P_i^2}{2m_e} + \frac{e^2}{4\pi\epsilon_0}\left(\frac{Z_A Z_B}{R} - \sum_i \frac{Z_A}{R_{iA}} - \sum_i \frac{Z_B}{R_{iB}} + \sum_i \sum_{i\neq j} \frac{1}{r_{ij}}\right), \tag{3.8}$$

where e, and m_e are charge and mass of an electron, R is the internuclear separation of A and B, Z_A and Z_B are nuclear charge of A and B, R_{iA} and R_{iB} are the distances between ith electron and A or B, ϵ_0 is the permittivity of vacuum, and r_{ij} is the distance between the ith and jth electrons.

In the case of a $^1\Sigma^+$ electronic state, the wavefunction of nuclear motion is

$$\psi_n(R) = R^{-1}\psi_{v,J}(R)Y_{l,m} \tag{3.9}$$

where $Y_{l,m}$ are the spherical harmonic functions, which are the angular part of the rotational wavefunction. The remaining task is to solve for the radial part of the wavefunction $\psi_{v,J}(R)$ from the effective one-dimensional Schrödinger equation [31]

$$-\frac{\hbar^2}{2\mu}\frac{d^2}{dR^2}\psi_{v,J}(R) + [U(R) + \frac{J(J+1)\hbar^2}{2\mu R^2}]\psi_{v,J}(R) = E(v,J)\psi_{v,J}(R), \qquad (3.10)$$

where μ is the reduced mass.

An important consequence of the Born-Oppenheimer approximation is the concept of the internuclear potential function $U(R)$. This function is the average field of electrons, in which the nuclear motion takes place. There is no universal analytical expression for $U(R)$. Closed form mathematical expressions for $U(R)$ may be determined for systems individually. But such procedures are very complex and have only been derived for very simple systems. Equation (3.10) may then be solved usually by numerical methods using a function $U(R)$. $U(R)$ may be determined empirically, or from the solution of the electronic Schrödinger equation by a variety of methods, or by combinations of both.

The choice of model for the potential energy function used to solve the nuclear Schrödinger equation is critical in the analysis of the rotation-vibration spectra of diatomic molecules. Rotation-vibration spectra experimentally sample the separation between energy levels of nuclei in different rotational and vibrational states. An empirical $U(R)$ may be constructed from the separation of energy levels elucidated in spectra. High quality theoretical $U(R)$ allow for the accurate extrapolation of empirical potential functions to energy levels beyond those observed experimentally.

3.2 Born-Oppenheimer Breakdown

The limits of the Born-Oppenheimer approximation and the concept of the internuclear potential energy function have been revealed through the interaction of spectroscopy and theory. Evidence of Born-Oppenheimer breakdown was first systematically studied by van Vleck [28] after the discovery of deuterium. As the m_e/M ratio has its greatest value for hydrogen, the effects of Born-Oppenheimer breakdown were most obvious in hydrides.

Many studies on the nature and the magnitude of the Born-Oppenheimer breakdown in various molecules have been carried out [29, 30]. Breakdown effects are detected through the failure of theoretical relationships between spectroscopic constants to describe experimentally derived constants. For example, let i and j be two isotopomers of a molecule, the relationship between their rotational constants B_e is theoretically given by

$$\frac{B_{ei}}{B_{ej}} = \frac{\mu_j}{\mu_i}. \tag{3.11}$$

For hydride and deuteride isotopomers, the breakdown of this relationship was reported in the 1930's [54]. As spectroscopic techniques become more accurate, this breakdown is also observed in heavier molecules [55]. Other experimental examples of the Born-Oppenheimer breakdown include the failure of relationships between lower and higher order spectroscopic constants of a single isotopomer, the coupling or perturbation between different electronic states in the molecule.

Breakdown effects may be characterized into two different categories: adiabatic and non-adiabatic [30]. Adiabatic corrections are necessary to account for the effect of the neglected kinetic energy of the nuclei within each electronic state. In infrared

spectroscopy, adiabatic corrections are the result of the coupling between nuclear motion and electronic motion in the isolated electronic state. Non-adiabatic corrections are necessary to account for interactions with other electronic states. Local non-adiabatic breakdowns are regularly detected experimentally in the spectra of rotationally and vibrationally highly excited molecules, made visible as perturbations in the observed line positions. When the effects of non-adiabatic coupling are significant, the concept of $U(R)$, which is only responsible for nuclear motion in an isolated electronic state, does not provide an adequate explanation of physical processes. The remedy is to solve the Schrödinger equation for complete wavefunctions that explain nuclear motion and electronic motion simultaneously.

3.3 The Dunham Potential Model

The Dunham model was developed by J.L. Dunham in 1932 [32]. It has been widely used ever since its introduction. The Dunham energy level formulation has been adopted for the analysis of rotation-vibration spectra in both high resolution infrared spectroscopy and microwave spectroscopy. Improvements in spectroscopic techniques have resulted in the determination of numerous limitations of the model, spurring the modification of the original Dunham expressions.

Dunham chose to represent $U(R)$ as a Taylor series expansion about the equilibrium internuclear separation R_e, where $U(R_e) = 0$,

$$U(R) = a_0\xi^2(1 + a_1\xi + a_2\xi^2 + a_3\xi^3 + \cdots), \tag{3.12}$$

where

$$\xi = \frac{R - R_e}{R_e} \tag{3.13}$$

and the set of $\{a_i\}$ are the Dunham potential parameters. Using Equation (3.12) for $U(R)$, Dunham solved the first-order semi-classical Wentzel-Kramer-Brillouin (WKB) quantization condition [31]

$$(\frac{2\mu}{\hbar^2})^{\frac{1}{2}} \int_{R_+}^{R_-} [E(v,J) - U(R)]^{\frac{1}{2}} dR = (v + \frac{1}{2})\pi \tag{3.14}$$

to determine $E(v,J)$, where R_+ and R_- are the classical turning points for the potential curve at energy $E(v,J)$. The result was the compact energy level expression

$$E(v,J) = \sum_{i,j} Y_{ij} (v + \frac{1}{2})^i [J(J+1)]^j, \tag{3.15}$$

where the Y_{ij} Dunham coefficients are explicitly known functions of the potential expansion parameters $\{a_i\}$.

One benefit of the Dunham model is the approximate equivalence of the Y_{ij} coefficients to the conventional empirical constants appearing in the rotational and vibrational term energy expressions:

$$\begin{array}{llll} Y_{10} \approx \omega_e & Y_{20} \approx -\omega_e x_e & Y_{30} \approx \omega_e y_e & Y_{40} \approx \omega_e z_e \\ Y_{01} \approx B_e & Y_{11} \approx -\alpha_e & Y_{12} \approx \gamma_e & \\ Y_{02} \approx -D_e & Y_{12} \approx -\beta_e & & \\ Y_{03} \approx -H_e. & & & \end{array} \tag{3.16}$$

The expressions for the conventional empirical constants all include the reduced

mass of the molecule. The values of the Y_{ij} coefficients are also dependent on the reduced mass of the molecule, and therefore, different isotopomers of a molecule must have different sets of Dunham coefficients. Within the first-order of WKB approximation and the Born-Oppenheimer approximation, the reduced mass dependency of the Y_{ij} coefficients can be factored out and the energy levels expressed in terms of mass-independent Dunham coefficients U_{ij},

$$E(v,J) = \sum_{i,j} \mu^{-(i+2j)/2} U_{ij} (v+\frac{1}{2})^i [J(J+1)]^j. \tag{3.17}$$

When the fitting of spectroscopic data on multiple isotopomers of the same species to Equation (3.17) fails, it reveals the failure of the Born-Oppenheimer approximation. This is so because the derivation of the Dunham energy level expression is based on this approximation. The fact that the Born-Oppenheimer approximation is not fully valid means that the approximate relation

$$U_{ij} = \mu^{(i+2j)/2} Y_{ij} \tag{3.18}$$

is observed to breakdown. The above expression has routinely failed to explain the relationships between the experimentally derived constants within the experimental errors.

The effects of Born-Oppenheimer breakdown are taken care of by the introduction of a correction term to the expansion of Equation (3.17):

$$E(v,J) = \sum_{i,j} \mu^{-(i+2j)/2} U_{ij} (v+\frac{1}{2})^i [J(J+1)]^j [1 + \frac{m_e}{M_A}\Delta_{ij}^A + \frac{m_e}{M_B}\Delta_{ij}^B], \tag{3.19}$$

where the Δ_{ij} parameters are mass-independent breakdown constants. Equation (3.19) was first introduced by Ross and co-workers [56]. Later, it was theoretically justified by both Watson [57,58] and Bunker [59]. Equation (3.19) is usually referred to as the Watson modified mass-independent Dunham expression because of Watson's major contribution.

The Δ_{ij} parameters are empirical constants which take account of the Born-Oppenheimer breakdown. They are expected to be close to unity for a well isolated electronic state. The Δ_{ij} parameters are the sum of the adiabatic correction term, the non-adiabatic correction term, and the Dunham correction term [32],

$$\Delta_{ij}^{k} = (\Delta_{ij}^{k})_{adiabatic} + (\Delta_{ij}^{k})_{non-adiabatic} + (\Delta_{ij}^{k})_{Dunham}. \tag{3.20}$$

The Dunham correction term $(\Delta_{ij}^{k})_{Dunham}$ takes into account the failure of the semi-classical WKB quantization condition to fully explain all quantum mechanical effects [57,58].

The most well understood Born-Oppenheimer correction term is Δ_{01}, which is independent of the potential parameters $\{a_i\}$. Tiemann [60] has studied the value of the Δ_{01} parameters in diatomic molecules with 10 valence electrons. For the case of Δ_{01}, the very small Dunham correction term may be calculated from

$$(\Delta_{01}^{k})_{Dunham} = \frac{\mu \Delta Y_{01}^{(D)}}{m_e B_e}, \tag{3.21}$$

where ΔY_{01} is the Dunham correction to the rotational constant B_e. The non-

adiabatic contribution may be determined from

$$(\Delta_{01}^{k})_{non-adiabatic} = \frac{(\mu g_J)_B}{m_p}, \tag{3.22}$$

where m_p is the mass of the proton and g_J is the rotational g factor measured in a Zeeman experiment. The $(\Delta_{01}^{k})_{adiabatic}$ term has no comparable independent method of calculation. On average, the value of $(\Delta_{01}^{k})_{adiabatic}$ is less than 30% of the total Δ_{01}^{k} value. It is predominantly characteristic of the atomic mass, and therefore is independent of the bonding partner.

One trend was the determination of abnormally large Δ_{01} parameters for heavy atomic centers [60]. Tiemann studied this enlargement of Δ_{01}, and attributed it to the effects of an isotopic field shift [61–64]. For large nuclei such as Pb and Tl [62], the difference in the Coulomb potential of the two isotopes results in a corresponding energy shift of the observed line positions. The field shift was characterized by mathematical expressions [64].

While the effects of field shift are not often applied to the examination of Δ_{01} parameters directly, they do illustrate the limitation of Equation (3.19). The Δ_{ij} are empirical parameters, so that they cannot distinguish between different failures of the Born-Oppenheimer approximation and the Dunham model. The values, therefore, lack physical significance.

The Dunham potential parameters a_i are functions of the energy level coefficients:

$$a_0 = \frac{Y_{10}^2}{4Y_{01}}$$

$$a_1 = \frac{Y_{11}Y_{10}}{6Y_{01}^2} - 1$$
$$a_2 = \frac{2Y_{20}}{3Y_{01}} + \frac{5a_1^2}{4}. \tag{3.23}$$

As Dunham stated in his original paper, the Dunham potential can be expressed entirely by the Y_{i0} and Y_{i1} coefficients. The immediate implication is that all Y_{ij} coefficients with $j \geq 2$ can be expressed in terms of the Y_{i0} and Y_{i1} coefficients [58]. These constraints can act as tests to confirm that the empirically obtained parameters agree with the physical model of the Dunham internuclear potential energy function.

The mass dependence of the Dunham coefficients can be derived directly from expressions of $\{a_i\}$ given in Equation (3.23), by using the relationship in Equation (3.18). Consequently, the theoretical relationships between U_{ij} coefficients can be established, for example,

$$U_{02} = -\frac{4U_{01}^3}{U_{10}^2}. \tag{3.24}$$

These relationships are only approximate if these U_{ij} constants have absorbed the Δ_{ij} corrections. The Δ_{ij} terms in Equation (3.19) correct for the effects of Born-Oppenheimer breakdown, so that equations like (3.24) become exact. In this case, the values of the U_{ij} coefficients with $j \geq 2$ are calculated as functions of empirically determined U_{i0} and U_{i1} coefficients.

In spite of its wide spread application and constant improvement, there are several limitations to the Dunham model. The major problem is that the Dunham model is a poor choice of potential energy function. In practice any Dunham series is truncated to a finite number of terms, and this polynomial diverges as

the internuclear separation increases, i.e., $R \rightarrow \infty$, while the realistic potential function is bounded by the dissociation energy. Thus, the Dunham model cannot accurately describe the high vibrational states because the long range interactions between atoms are poorly expressed. Because the Dunham potential is inadequate, the Dunham coefficients are not ideal for analyzing highly vibrationally excited states, and cannot reliably extrapolate to energy levels beyond the range covered by experimental observation.

3.4 The Parameterized Potential Model

Another approach to reduce spectroscopic data to molecular constants is to use the parameterized potential model. In this model, the observed line positions are fit directly to the eigenvalues of the radial Schrödinger equation containing an empirical, or a semi-empirical parameterized potential function. Synthetic spectra are produced by numerically solving the Schrödinger equation for all eigenstates involved in the spectra. Then the agreement with experiment is optimized by varying the parameters used to define a model potential for $U(R)$. This method was used for atom-molecule van der Waals complexes [65]. The method was first applied to diatomic molecules by Kosman and Hinze [66], and was termed "inverse perturbation approach", or "IPA". There was significant refinement of this technique by Bunker and Moss [33], and more recently by Coxon and Hajigeorgiou [34–36]. This procedure has not been widely adopted, and the simpler semi-classical Rydberg-Klein-Rees (RKR) approach is still commonly used.

The direct determination of a parameterized potential from experiment has sev-

eral advantages over the Dunham model. The parameters defining the potential function are determined by solving the Schrödinger equation of the molecular system. The errors that are associated with the WKB approximation are avoided. It has become possible to incorporate into the analysis sophisticated physical behaviors determined from non-spectroscopic techniques. The resulting potential functions are more reliable at long range. They can be used to predict observables such as transition frequencies between unobserved levels [23], bulk properties of the system, and collisional phenomena [67].

An inherent limitation of the parameterized potential model is the assumed functional form of the interaction potential. Given a particular functional form, there exists no general proof that the resulting parameterized potential is a unique representation of the experiment. Since the model needs to be general, the functional form for the potential must have flexibility. The functional form should be flexible enough to describe the physical information contained in the data while not introducing large statistical inter-parameter correlations. A good functional form will be optimized in the region where data are observed, but will also provide meaningful information for the internuclear separations not sampled by the observed data.

The functional form used in this study was provided by Dulick [68–70]. It is a modification of a function used by Coxon and Hajigeorgiou to fit a wide range of spectroscopic data [34–36]. The function is contained within the effective radial

Schrödinger equation for a diatomic molecule in the $^1\Sigma^+$ electronic states, given by

$$-\frac{\hbar^2}{2\mu}\frac{d^2}{dR^2}\psi_{v,J}(R) + [U^{eff}(R) + \frac{\hbar^2}{2\mu}(1+q(R))\frac{J(J+1)}{R^2}]\psi_{v,J}(R) = E(v,J)\psi_{v,J}(R). \tag{3.25}$$

A centrifugal correction factor $1 + q(R)$ is introduced to take account of rotational Born-Oppenheimer breakdown effects. The effective internuclear potential for purely vibrational motion $U^{eff}(R)$ is given by

$$U^{eff}(R) = U^{BO}(R) + \frac{U_A(R)}{M_A} + \frac{U_B(R)}{M_B} \tag{3.26}$$

where U^{BO} is the Born-Oppenheimer potential, and U_A and U_B are the correction functions for each atomic center respectively. U^{BO} is chosen to be a modified Morse function [68–70],

$$U^{BO}(R) = D_e[\frac{1-e^{-\beta(R)}}{1-e^{-\beta(\infty)}}]^2, \tag{3.27}$$

where D_e is the dissociation energy of the molecule, and is used as a fixed constraint in the fitting of data. The $\beta(R)$ term is the variable Morse curvature function, which accounts for radial dependence of the anharmonicity functions. $\beta(R)$ is given as a polynomial expansion

$$\beta(R) = z\sum_{i=0}^{n}\beta_i z^i. \tag{3.28}$$

$\beta(\infty)$ is given by

$$\beta(\infty) = \sum_{i=0}^{n}\beta_i, \tag{3.29}$$

and

$$z = \frac{R - R_e}{R + R_e} \tag{3.30}$$

is one-half of the Ogilvie-Tipping variable. The parameterized Morse function gives excellent convergence and has been shown to behave well for large internuclear separation R.

Through fitting data to Equation (3.25) using the potential given by Equation (3.26), the correction terms are divided into vibrational and rotational Born-Oppenheimer breakdown terms. As the energy of vibrational motion increases, nuclear excitation moves to the electron cloud, thereby coupling the electrons from distant Σ states to the ground Σ state. These homogeneous, non-adiabatic effects along with any J-independent adiabatic effects are accounted for by the U_A and U_B functions. These two functions are given by power series expansions:

$$U_A(R) = \sum_{i=1}^{n} u_i^A (R - R_e)^i \tag{3.31}$$

and

$$U_B(R) = \sum_{i=1}^{n} u_i^B (R - R_e)^i. \tag{3.32}$$

The u_i coefficients are isotopically invariant. As the energy of rotational motion increases, nuclear angular momentum moves to the valence electrons, resulting in a net non-zero electronic angular momentum as the electron distribution along the internuclear axis becomes distorted. The electronic angular momentum imparts a partial Π character into the Σ state, thereby resulting in coupling of the ground electronic state with distant Π states. These heterogeneous non-adiabatic effects

are accounted for by

$$q(R) = \frac{q_A(R)}{M_A} + \frac{q_B(R)}{M_B} = \sum_{i=1}^{n} q_i^A (R - R_e)^i + \sum_{i=1}^{n} q_i^B (R - R_e)^i. \qquad (3.33)$$

3.5 Infrared Emission Spectroscopy of BF and AlF

Since the BF spectrum was first observed by Dull [71] in 1935, BF has been subject to numerous spectroscopic studies [72–81]. The electronic emission spectra of BF were recorded in many laboratories, but it was not until 1969 that Caton and Douglas [79] first studied electronic absorption spectra of BF. In their report, Caton and Douglas gave an excellent overview of the electronic spectra. They not only clarified the assignments of the electronic states, but also they observed a series of Rydberg states approaching the ionization limit, which enabled them to determine the ionization potential (I.P.) very accurately. Their value of I.P. (11.115 ± 0.004 eV) agrees well with the values obtained from electron impact mass spectrometry (11.06 ± 0.10 eV) [82] and photoelectron spectroscopy (11.12 ± 0.01 eV) [83]. Lovas and Johnson [84] recorded the first microwave spectrum of BF. They measured the $J = 1 \rightarrow 0$ transitions of ^{11}BF and ^{10}BF and analyzed the hyperfine structure. They reported a dipole moment for $v = 0$ of 0.5 ± 0.2 D for BF. Recently, Cazzoli et al. extended the frequency coverage of the microwave spectrum and obtained more transitions [85]. Nakanaga et al. measured 12 vibration-rotation transitions of ^{11}BF fundamental band using a diode laser [86].

The vibrational band strength of ^{11}BF was measured, and the value of $d\mu/dr$ was found to be 4.9 $\pm$ 0.8 D/Å [87].

Since BF is a member of the interesting isoelectronic group of molecules N_2, CO and BF, several detailed theoretical calculations of the properties of the ground and excited states have also been carried out [88–95]. The spectroscopic constants are in good agreement with the experimental values, including the value for $d\mu/dr$. The value of the calculated dipole moment is about twice the experimental value, so it has been suggested that Lovas and Johnson underestimated μ_0 in their experiment.

During the course of this experiment, an improved spectrum of AlF was recorded as impurity. This spectrum was also analyzed to produce updated spectroscopic constants and potential function.

3.5.1 Experiment

BF was generated inadvertently during our spectroscopic study of the CaF [96] free radical. A mixture of a trace amount of boron and 40 g of CaF_2 powder was contained in a carbon boat, which was placed in a reaction cell. The reaction cell consisted of a 1.2 meter long alumina (Al_2O_3) tube sealed with two KRS-5 windows at both ends. The alumina tube was further protected from the corrosive effects of the CaF_2 salt by a carbon liner tube. The central portion of the cell was situated inside a CM Rapid Temp furnace (Figure 3.1). The furnace was heated by eight molybdenum disilicide elements. A Honeywell universal digital controller was used to provide control over the temperature of the heating system. The maximum heating rate which will prevent the alumina tube from cracking is 200°C per hour.

The cell was first heated under vacuum up to 500°C, and was then pressurized with 5 Torr of argon to prevent deposition of solid material onto the cell windows which were at room temperature. Stainless steel threaded caps that held the cell windows were placed on the end of the tubes. Copper cooling coils that surrounded the end caps prevented them from overheating and melting the rubber O-rings. There are two ports attached to the cell. One is for the gas inlet, which allows the introduction of argon gas into the cell, the other is connected to a vacuum pump. The alumina cell was aligned to the optical axis of the spectrometer through the use of an external globar lamp. When the cell temperature reached 1600°C, strong emission of BF and AlF was detected.

When the temperature was below 1400°C, strong absorption of BF_3 bands was observed. The original experiment was to record spectra of CaF_2 and CaF. But no band of CaF_2 was found in the survey spectra. As the temperature increased, the intensity of BF_3 absorption bands decreased, and BF started to form. The high resolution spectrum of BF was recorded at a resolution of 0.01 cm^{-1}. A liquid nitrogen-cooled HgCdTe detector, a KBr beamsplitter, and a KRS-5 entrance window were used. The lower limit of the spectral bandpass was set by the detector response at 850 cm^{-1} while the upper limit was set by a red pass optical filter with a cut-off wavenumber of 1670 cm^{-1}. The final spectrum of BF was a result of co-adding 40 scans in about 40 minutes. A section of the spectrum is shown in Figure 3.2. AlF emission spectrum was obtained in a similar way except a Si:B photodetector was used.

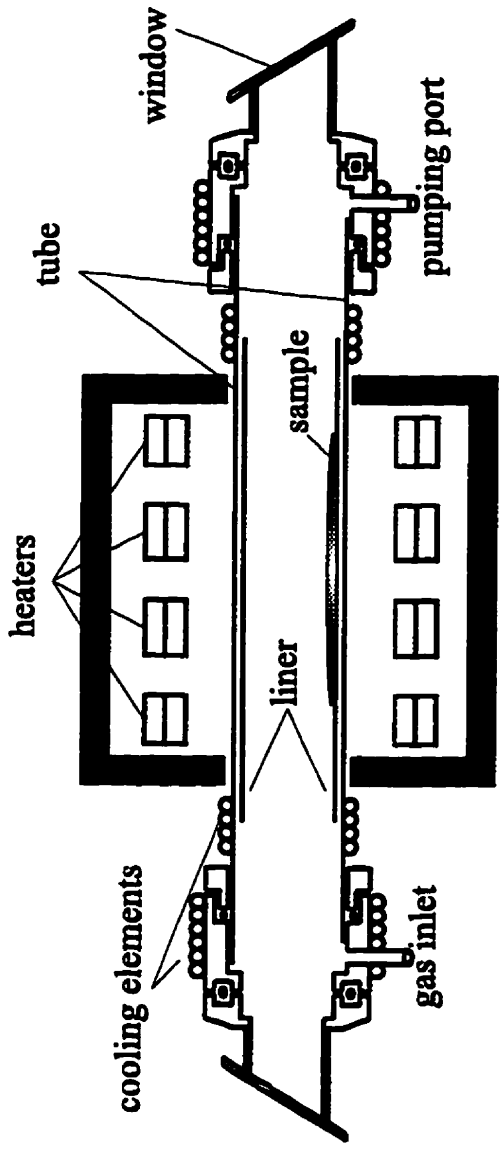

Figure 3.1: The schematic of CM Rapid Temp furnace

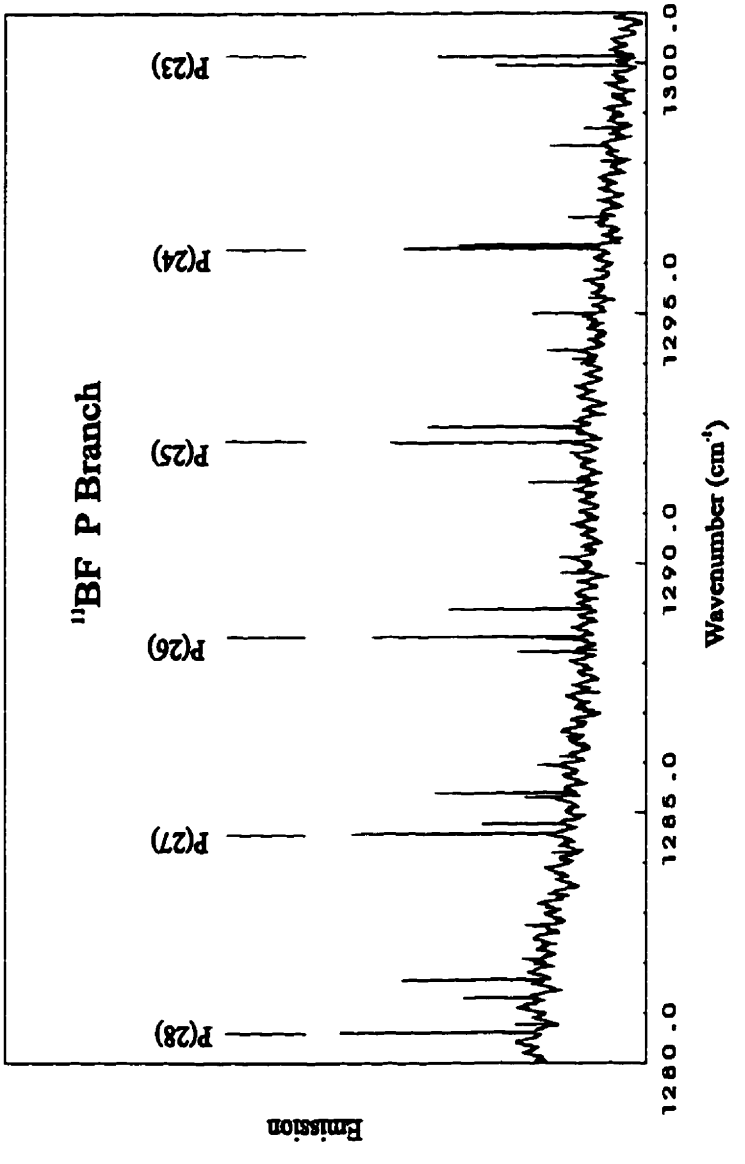

Figure 3.2: An expanded view of the P branch of the BF $v = 1 \rightarrow 0$ band

3.5.2 Results and Discussion

Since BF_3 was present in the cell when the spectrum was taken, part of the R branches of ^{11}BF and all of the R branches of ^{10}BF were buried in the absorption of the ν_3 band of BF_3.

The rotational lines are measured using the computer program PC-DECOMP developed by J.W. Brault. From the displayed experimental spectra, the user chooses a baseline and selects spectral features of interest. The program then fits each line profile to a Voigt line shape function, which is a convolution of Gaussian and Lorenzian line shape functions. The separation of different vibrational bands and the assignment of the rotation-vibration transitions are facilitated by LOOMIS-WOOD, an interactive color graphics program developed by C.N. Jarman.

The pure rotational lines of HF which were present in the spectra as an impurity, were used to calibrate the BF and AlF spectra [97]. The error in the calibrated line positions is estimated to be 0.0002 cm^{-1} for ^{11}BF and 0.0005 cm^{-1} for ^{10}BF and AlF. Five bands of ^{11}BF from $v = 1 \rightarrow 0$ to $v = 5 \rightarrow 4$ are analyzed, while three bands of ^{10}BF from $v = 1 \rightarrow 0$ to $v = 3 \rightarrow 2$ are studied. The line positions of BF are given in Table A.1

Dunham Model

^{11}BF and ^{10}BF Dunham Y_{ij} coefficients were determined from the observed line positions from a linear least-squares fit. Microwave measurements of the ^{11}BF and ^{10}BF pure rotational transitions, with hyperfine structure corrected by Cazzoli et al. [85], were also added as input to the linear fit. The Dunham coefficients for both

isotopomers are listed in Table 3.1, while the mass-reduced Dunham U_{ij} coefficients are listed in Table 3.2. In Table 3.2, under the column heading "unconstrained", the U_{ij} coefficients were obtained from a combined fit of isotopomer data to Equation (3.17).

Since only one naturally occurring isotope of fluorine exists, all isotopic information on Born-Oppenheimer breakdown is confined to the boron atom. Therefore, only Δ_{ij} for the boron atom were determined from the least-squares fit of the data. Finally, the set of U_{ij} under the column heading "constrained" in Table 3.2 were obtained from a fit where the U_{ij} for $j \geq 2$ were treated as independent parameters while all remaining U_{ij} were fixed to values determined from the constraint relations implicit in the Dunham model [98]. The reduced χ^2 of the "unconstrained" and "constrained" fits are 0.9727 and 0.9667 respectively. It is believed that the constrained fit is more meaningful since it uses fewer parameters. Indeed the Δ_{ij}^B parameters for the constrained fit have much more reasonable values.

Parameterized Potential Model

In order to estimate information on the high-lying rotation-vibration levels of the ground state, a reliable internuclear potential energy function is required. Such a potential function can be determined from a least-squares fit [98] of the combined ^{11}BF and ^{10}BF data to the eigenvalues of the radial Schrödinger equation.

Our fitting procedure is similar to the method reported by Coxon and Hajigeorgiou and is described in greater detail elsewhere. None of the q parameters that correct for J-dependent Born-Oppenheimer breakdown in the centrifugal term could be determined using our data set. Results of the potential fit are given in

Table 3.1: Dunham Y_{ij} coefficients for ^{10}BF and ^{11}BF in cm^{-1}.

Coefficient	^{10}BF	^{11}BF
Y_{10}	1445.6660(10)	1402.15865(26)
Y_{20}	-12.57365(61)	-11.82106(15)
Y_{30}	0.059565(97)	0.051595(35)
$10^4 \times Y_{40}$	-	3.464(29)
Y_{01}	1.61228632(86)	1.51674399(21)
Y_{11}	-0.0208783(16)	-0.01904848(22)
$10^5 \times Y_{21}$	6.736(92)	5.8464(76)
$10^6 \times Y_{31}$	1.38(13)	1.2899(73)
$10^6 \times Y_{02}$	-8.0208(59)	-7.09528(35)
$10^8 \times Y_{12}$	1.191(48)	0.9605(52)
$10^9 \times Y_{22}$	0.74(16)	1.05(14)

Table 3.2: Mass-reduced Dunham coefficients and Born-Oppenheimer breakdown constants for the boron atom in cm^{-1}.

Constant	Unconstrained	Constrained
U_{10}	3701.6995(32)	3701.6938(21)
U_{20}	-82.3937(10)	-82.39384(97)
U_{30}	0.94859(64)	0.94852(63)
U_{40}	0.01702(14)	0.01707(14)
U_{01}	10.572952(33)	0.572893(22)
U_{11}	-0.350748(61)	-0.350606(13)
$10^3 \times U_{21}$	2.8422(37)	2.8540(25)
$10^4 \times U_{31}$	1.6520(94)	1.6134(88)
$10^4 \times U_{02}$	-3.4673(73)	-3.45017003
$10^6 \times U_{12}$	1.2359(68)	1.30362995
$10^7 \times U_{22}$	3.518(47)	3.04905340
$10^8 \times U_{32}$		1.39465056
$10^{10} \times U_{03}$		7.31811680
$10^{11} \times U_{13}$		2.86741980
$10^{11} \times U_{23}$		4.31289760
$10^{13} \times U_{04}$		-1.44942336
$10^{14} \times U_{14}$		1.97762269
$10^{15} \times U_{24}$		1.95249239
$10^{18} \times U_{05}$		-2.29286491
$10^{18} \times U_{15}$		2.54097932
$10^{23} \times U_{06}$		1.06645896
$10^{22} \times U_{16}$		1.40418786
$10^{26} \times U_{07}$		2.04263339
$10^{30} \times U_{08}$		1.99636817
Δ^B_{10}	0.832(17)	0.865(10)
Δ^B_{01}	-1.838(61)	-1.718(40)
Δ^B_{11}	-12.3(34)	-3.38(65)
Δ^B_{02}	-116.(42)	-7.62(83)

Table 3.3. The potential energy curve of BF is shown in Figure 3.3. Potential parameters that were statistically determined are listed along with their uncertainties quoted to one standard deviation. The value of D_e was fixed to that given in Huber and Herzberg [99]. The standard deviation of the fit is 1.5864.

The analysis of AlF spectrum was similar to that of BF. Hot bands of AlF up to $v = 9 \rightarrow 8$ were measured. The updated Dunham coefficients for AlF are listed in Table 3.4 together with those reported in Ref [100]. Although the highest vibrational energy level accessed is $v = 5$ in the previous work [100] while transitions involving up to $v = 9$ were measured in this study, the changes in the Dunham coefficients are very small. This indicates that the Dunham model is adequate for a moderately heavy molecule such as AlF. A parameterized potential was also determined, and the potential energy parameters for AlF are given in Table 3.5. The value of D_e was also fixed to that given in Huber and Herzberg [99].

Relative Transition Dipole Moment

The experimental intensity parameters are very important in the evaluation of abundances and temperatures of gaseous species by spectroscopic means. Measuring line intensities are also important for the understanding of the variation of the molecular dipole moment with respect to normal coordinates, i.e. the dipole moment function [101]. However, rotation-vibration line intensities of free radicals are difficult to measure because of the small and uncertain column densities.

In our spectroscopic study of BF, we obtained a relatively high signal-to-noise spectrum (Figure 3.2), thus enabling us to investigate the line intensities of BF. Since there was no means of obtaining the concentration of BF present in the

Table 3.3: Internuclear potential energy parameters for BF.

Parameter	Value	Uncertainty
$D_e/10^4$ cm^{-1}	6.36	
R_e/Å	1.262711672	4.23×10^{-7}
β_0	4.51429026	2.30×10^{-6}
β_1	1.4509287	5.42×10^{-5}
β_2	0.098562	8.13×10^{-4}
β_3	3.8626	1.48×10^{-2}
β_4	26.402	1.42×10^{-1}
β_5	69.05	1.74
u_1^B/cm^{-1}Å^{-1}	-208.93	1.93
u_2^B/cm^{-1}Å^{-2}	790.04	5.41
u_3^B/cm^{-1}Å^{-3}	-310.16	4.27
$M_A(^{19}F)$/amu	18.99840322	
$M_B(^{11}B)$/amu	11.0093054	
$M_B(^{10}B)$/amu	10.0129369	

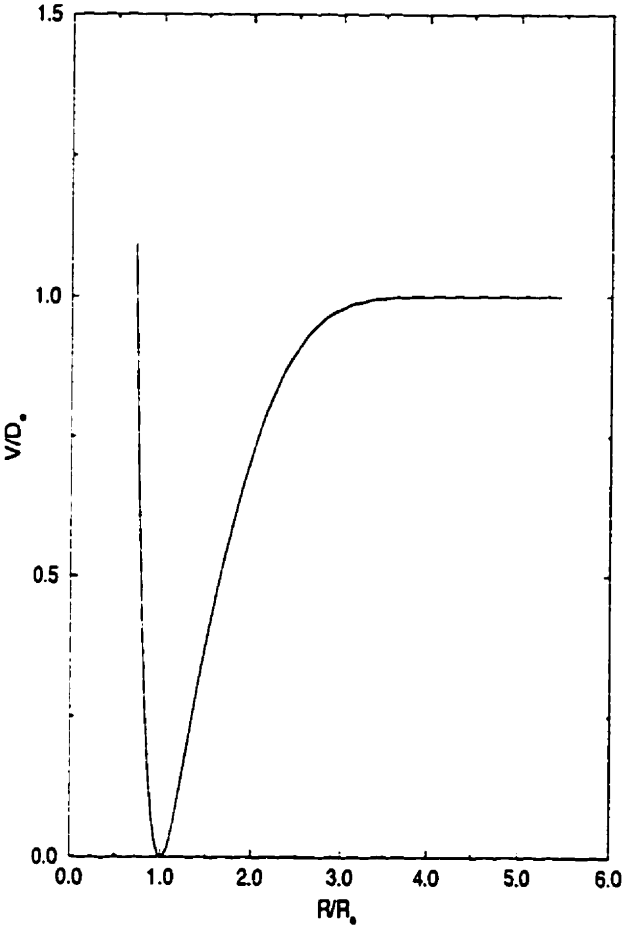

Figure 3.3: The Born-Oppenheimer potential energy function for BF

Table 3.4: Dunham Y_{ij} coefficients for AlF in cm^{-1}.

Coefficient	This Work	HB†
Y_{10}	802.32447(11)	802.32385(15)
Y_{20}	-4.849915(44)	-4.849536(98)
Y_{30}	0.0195738(68)	0.019497(24)
$10^5 \times Y_{40}$	3.407(35)	2.95(20)
Y_{01}	0.552480208(65)	0.552480296(49)
$10^3 \times Y_{11}$	-4.984261(44)	-4.984214(60)
$10^5 \times Y_{21}$	1.7215(95)	1.7153(22)
$10^8 \times Y_{31}$	4.022(57)	5.03(24)
$10^6 \times Y_{02}$	-1.047999(51)	-1.048280(68)
$10^9 \times Y_{12}$	1.7814(93)	1.8548(80)
$10^{11} \times Y_{22}$	6.578(75)	3.01(19)
$10^{13} \times Y_{03}$	-3.674(49)	-3.050(93)
$10^{15} \times Y_{22}$	9.55(74)	-

† Hedderich and Bernath, J. Mol. Spec. 153, 73 (1992)

Table 3.5: Internuclear potential energy parameters for AlF.

Parameter	Value	Uncertainty
$D_e/10^4$ cm^{-1}	5.60	
R_e/Å	1.6543689056	6.95×10^{-8}
β_0	4.561386175	4.87×10^{-7}
β_1	0.4435571	2.62×10^{-5}
β_2	0.805792	1.88×10^{-4}
β_3	8.12058	7.96×10^{-3}
β_4	11.0386	5.02×10^{-2}
$M_A(^{19}F)$/amu	18.99840322	
$M_B(^{27}Al)$/amu	26.9815386	

high temperature cell, only the relative intensities of the ^{11}BF rotational lines were measured. Due to the fact that the transmission of the optics, the efficiency of the beamsplitter and the response of the detector vary with frequency, a narrow wavenumber range was chosen. The choice of wavenumber range was somewhat arbitrary, but it was chosen in such a way that there were intense lines within the range, and the line intensities can be measured readily, i.e. there were no blended lines and the continuum level could be determined to a high degree of accuracy. Consequently, the range between 1280 and 1300 cm^{-1} was selected. Since $v = 5 \rightarrow 4$ band is weak, only four bands from $v = 1 \rightarrow 0$ to $v = 4 \rightarrow 3$ were compared. Equation (3) in Ref [102] was applied to convert rotational line intensities to transition dipole moments. The measured average transition dipole moments were normalized to that of $v = 1 \rightarrow 0$ band, their values are listed in Table 3.6 together with the ab initio predictions obtained from Refs [95] and [93] There is a good agreement between our experimental values and the ab initio results. The ab initio calculations of the dipole moment function are clearly of high quality.

3.5.3 Conclusion

Fourier transform infrared emission spectroscopy is a very useful technique for recording high resolution vibration-rotation spectra of high temperature molecules. Our infrared data on ^{11}BF and ^{10}BF together with existing microwave data, were converted to spectroscopic constants in two ways. The first approach utilized the traditional Dunham model extended to include data from different isotopomers. It is evident that imposing constraints on the Dunham coefficients improves con-

Table 3.6: Relative transition dipole moments of ^{11}BF.

Band	This Work	HHB*	RWG†
$1 \rightarrow 0$	1	1	1
$2 \rightarrow 1$	1.42	1.44	1.44
$3 \rightarrow 2$	1.71	1.78	1.79
$4 \rightarrow 3$	2.13	-	2.10

⋆ Honigmann, Hirsch and Buenker, Chem. Phys. 172, 59 (1993)
† Rosmus, Werner and Grimm, Chem. Phys. 92, 250 (1982)

sistency among the parameters. The second approach employed a parameterized potential model which uses a direct comparison between the experimental data and solutions to the Schrödinger equation. The second model can predict higher lying rotation-vibration energy levels of the electronic ground state that are at least qualitatively correct. The traditional Dunham model is inadequate when extrapolating far beyond the range of experimental measurements. Finally, the relative transition moments were also measured, and the values agree with the ab initio calculation satisfactorily. Provided that spectra with good signal-to-noise ratio are available, the relative transition dipole moments of other transient molecules can be determined, and possibly the dipole moment functions.

The BF experiment proves once again that the superior spectral coverage of the Fourier transform spectrometer is important for recording new spectra. The original experiment to obtain spectra of CaF [96] was carried out near 600 cm^{-1}, but the BF band was recorded near 1300 cm^{-1}. The ability to survey a wide range of frequencies in a short period of time makes the Fourier transform spectroscopy the ideal technique to investigate new spectra.

3.6 Infrared Emission Spectroscopy of MgF

The electronic and microwave spectra of alkaline earth monohalides have been studied extensively [103–106]. However, little is known about the infrared spectra of these molecules. During our systematic investigation of the infrared spectra of the alkaline earth monofluorides, the high resolution vibration-rotation emission spectrum of MgF was recorded for the first time.

The rotational analysis of the electronic spectrum of MgF was performed by Barrow and Beale [107]. The structure and bonding of MgF was determined from its millimeter-wave spectrum [108,109]. MgF, like all the other alkaline earth monohalides, is found to be highly ionic [110]. When compared with the other heavier alkaline earth monofluorides, MgF has a greater degree of covalent bonding as determined by the hyperfine structure.

Ionic molecules are suitable candidates for testing simple semi-classical bond models [111–115]. Because MgF and the other alkaline earth monohalides are mainly ionic molecules, a Rittner-type model for the potential energy was developed by Torring et al. [112,113]. But as Bauschlicher et al. [114] pointed out, when more accurate polarizabilities are used, the model by Torring et al. fails completely. Refined ab initio calculations [111,115] were also carried out.

3.6.1 Experiment

The experimental arrangement was similar to that described in a published paper [116]. A sample of 30 g of MgF_2 was contained in a carbon boat placed in the center of a carbon liner that was housed inside of a mullite ($3Al_2O_3{\cdot}2SiO_2$) tube. The central 50 cm portion of the mullite tube was heated by a CM Rapid Temp furnace. The ends of the mullite tube were water-cooled and sealed with KRS-5 windows. The tube was heated up to 1550°C at a rate of 200°C per hour. The sample cell was pressurized with 10 Torr of argon gas to prevent condensation of salt vapors on the cell windows.

The infrared radiation emitted from the furnace was introduced through the

emission port into a Bruker IFS 120 HR Fourier transform spectrometer. The infrared emission spectrum was recorded with a liquid helium-cooled Si:B detector and a KBr beamsplitter.

The bands of MgF_2 were found but could not be analyzed because of their complexity. The best spectrum of MgF was recorded at 1550°C, with 50 scans co-added in about 50 minutes at a resolution of 0.01 cm^{-1} in the spectral range from 350 to 1000 cm^{-1}. A portion of the infrared emission spectrum of MgF is shown in Figure 3.4. Rotational lines are well resolved, but the spin-rotation splitting in the $X^2\Sigma^+$ state was not resolved.

3.6.2 Results

Rotational spectral lines were measured by using the program PC-DECOMP written by J.W. Brault. Centers of lines were determined by fitting line profiles to Voigt line shape functions. Rotational lines of HF, which were present in our spectrum as an impurity, were used to calibrate MgF line positions [97]. The assignment of the MgF spectrum was facilitated by an interactive color Loomis-Wood program. The accuracy of most calibrated line positions is 0.001 cm^{-1}. More than 800 spectral lines of bands from $v = 1 \rightarrow 0$ to $v = 7 \rightarrow 6$ were assigned. The line positions are listed in Table B.1.

Since the spin-rotation splitting was not resolved in the spectrum, the ground state of MgF was treated as if it were a $^1\Sigma^+$ state. Dunham Y_{ij} constants for MgF were obtained by fitting the observed frequencies and available microwave data to

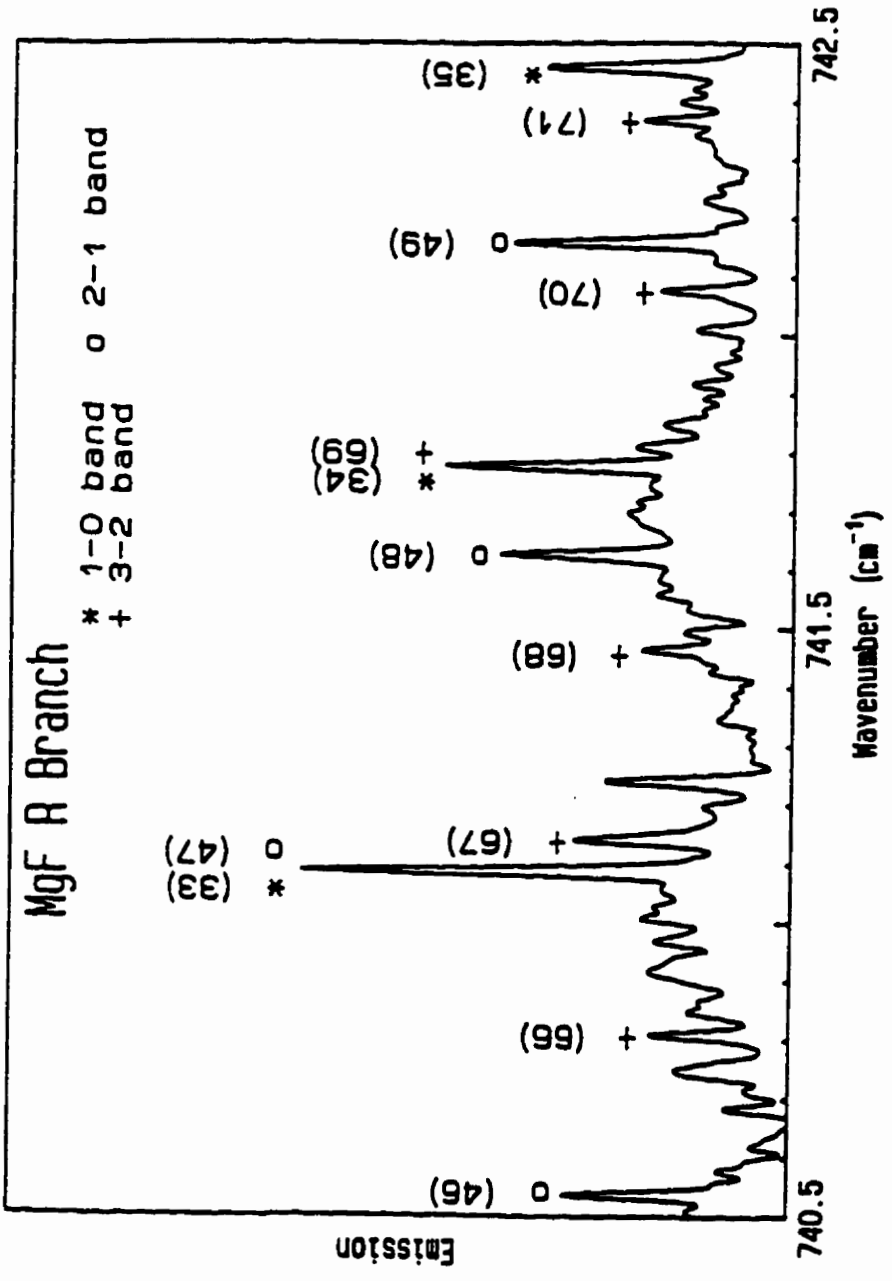

Figure 3.4: A portion of the high resolution emission spectrum of MgF

the energy expression

$$E(v,N) = \sum_i \sum_j Y_{ij}(v+\frac{1}{2})^i[N(N+1)]^j. \qquad (3.34)$$

Pure rotational transitions [110] were corrected for the effect of the fine structure and hyperfine structure and included in the final fit. The Dunham coefficients are listed in Table 3.6.2. The R_e value calculated from Y_{01} is 1.749937(1) Å.

Table 3.7: Dunham Y_{ij} coefficients for MgF in cm^{-1}.

Coefficient	Value
Y_{01}	0.519272510(42)
$10^6 \times Y_{02}$	-1.08079(16)
$10^{13} \times Y_{03}$	1.78(20)
Y_{10}	720.14042(30)
$10^3 \times Y_{11}$	-4.717446(43)
$10^9 \times Y_{12}$	-3.229(14)
Y_{20}	-4.26018(16)
$10^5 \times Y_{21}$	1.7529(10)
$10^{11} \times Y_{22}$	2.69(27)
$10^2 \times Y_{30}$	1.6509(32)
$10^5 \times Y_{40}$	-4.19(21)

Chapter 4

High Resolution Infrared Spectroscopy of Nitrile Oxides

Most nitrile oxides (RCNO) are short-lived, and reactive species. They are structurally isomeric with isocyanates (RNCO), and cyanates (ROCN). The parent members of the series, fulminic acid (HCNO), and cyanogen di-N-oxide (ONCCNO) are explosive and have to be handled with great caution. Since nitrile oxides dimerize via a cycloaddition to furoxans, they are widely used in synthetic chemistry for 1,3-dipolar cycloadditions by in situ generation and subsequent reaction in solution [117–119]. Little is known, however, about their structure and spectroscopy. Because the reactivity of nitrile oxides is very high, their isolation was considered to be difficult. There has been some success in isolating nitrile oxides in low temperature inert gas matrices. Maier and Teles [120] have reported the first infrared spectra of ClCNO, BrCNO and NCCNO in argon matrices at 10 K.

Although experimental difficulties prevented Maier and Teles [120] from collect-

ing detailed spectroscopic data on nitrile oxides, quantum mechanical calculations can provide information on the properties of these molecules. The parent species, fulminic acid HCNO is one of the few nitrile oxides to have been subjected to intense experimental scrutiny by means of infrared and microwave spectroscopy [101,120]. The investigation was focused on its quasi-linear behavior, and alternative isomeric forms. It is difficult to determine from ab initio calculations whether HCNO has a bent or linear equilibrium structure. Increasingly extensive ab initio studies have shown that both geometries are possible, depending on the level of theory. For the BrCNO molecule, ab initio calculations have been carried out at the levels of HF, MP2, MP3, MP4SQD, and MP4SDTQ [121]. The calculated structure of BrCNO, depending on the level of theory chosen, can be either linear or bent.

As with all large-amplitude molecular motions, quasi-linearity is associated with an anharmonic potential energy function, and cannot be explained by infinitesimal rectilinear coordinates. The quasi-linear bending motion is the only large-amplitude molecular motion that characterizes a molecular system assuming two entirely different geometries. A linear molecule has 2 rotational and $3n-5$ vibrational degrees of freedom, and a bent planar molecule has 3 rotational and $3n-6$ vibrational degrees of freedom. It is clear that there is a smooth transition between these two cases through the behavior of quasi-linear bending. However, the typical treatments which are constantly applied to rigid molecules, are not very useful here. These methods include separation of rotational and vibrational motion as an essential assumption. The bending motion and rotation about the axis of least moment of inertia, are so strongly coupled in quasi-linear molecules that they must be treated

together.

The spectra of quasi-linear bending fundamental modes are anomalous, as are the spectra of combination modes that involve quasi-linear bending. High resolution studies are necessary to identify details in the vibration-rotation spectra. However the high resolution infrared spectroscopy alone cannot fully explain the quasi-linear bending motion. Microwave spectroscopy and other techniques, such as photoelectron spectroscopy, also play an important role.

4.1 Experiment

Pasinszki and Westwood [121] have devised good methods for the generation of NC-CNO and ONCCNO molecules in the gas phase. Their work led to recording high resolution infrared spectra of ONCCNO [122] and NCCNO [123], and microwave spectra of NCCNO [124]. Encouraged by their success, Pasinszki and Westwood have recorded the first gas phase spectra of BrCNO [121]. An obvious challenge to high resolution spectroscopy of reactive molecules is maintaining sufficient concentration of sample in the cell for an extended period of time. Because of its reactive nature, the sample constantly disappears, and therefore, must be generated continuously. This requires that a large amount of precursor must be prepared before the experiment.

There are two convenient ways of generating BrCNO. One method is pyrolysis of dibromoformaldoxime (Br_2C=NOH), and the other is pyrolysis of the furoxan-like dimer of BrCNO. In this study, the BrCNO molecule was generated in situ using gas phase pyrolysis of dibromoformaldoxime, Br_2C=NOH.

The experimental setup was typical for absorption work using a single-pass sample cell and a glower (Figure 4.1). The infrared glower was collimated with a parabolic mirror and passed through a 120 cm long absorption cell sealed with two KRS-5 windows. The infrared radiation was then collected with a 45° off-axis parabolic mirror, and entered the Fourier transform spectrometer through the emission port. There are two ports attached to the absorption cell. One is for the gas inlet, and the other is the pumping port. The pyrolysis apparatus was connected to the gas inlet, and the pyrolysis products were pumped slowly out of the sample cell with the cell pressure maintained at about 250 mTorr.

The pyrolysis was carried out in a 15 cm long quartz tube with 8 mm inner diameter. For more efficient thermal contact, the tube was loosely packed with quartz chips. The quartz tube was placed inside a small furnace whose temperature was controlled by manually adjusting the voltage. Dibromoformaldoxime had adequate vapor pressure at room temperature, and its vapor was introduced into the furnace. Dibromoformaldoxime started to decompose at 300°C. The pyrolysis produced a large number of species, with relative amounts that varied as the temperature of pyrolysis increased. At 500°C, the yield of BrCNO was abundant with small amounts of CO, CO_2, HCNO, HNCO present in the spectra either as the side products of the thermolysis or from the subsequent destruction of BrCNO.

The high resolution absorption spectra were recorded with a Bruker IFS 120 HR spectrometer. The resolution of the spectra was 0.004 cm^{-1}. Although a higher resolution would be desirable, the period of time that the sample would last forced some sacrifice in resolution. A KBr beamsplitter was used for all experiments. The

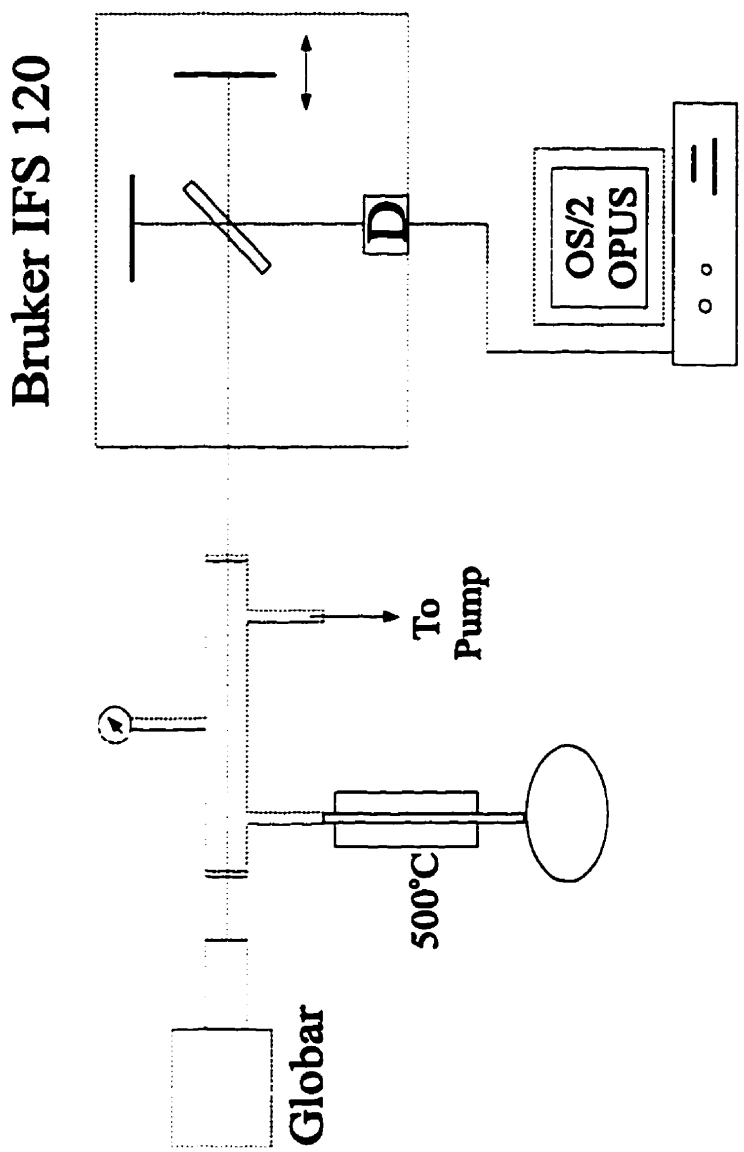

Figure 4.1: Setup for the BrCNO absorption experiment

ν_1 mode, near 2200 cm^{-1}, was recorded with a liquid nitrogen-cooled InSb detector. A total of 60 scans were co-added in the 1800-2900 cm^{-1} region, which was limited by a red-pass filter with a cutoff at 2900 cm^{-1} and the response of the InSb detector. The ν_2 mode, near 1300 cm^{-1}, was recorded with a liquid nitrogen-cooled MCT detector. The lower limit of the spectrum was determined by the response of the MCT detector, while the upper limit was set by a red-pass filter with a cutoff at 1672 cm^{-1}. In total, 50 scans were co-added.

4.2 Results and Analysis

The spectral line measurements were made with the spectral analysis program PC-DECOMP, developed by J.W. Brault. The peak positions were determined by fitting a Voigt line shape function to each spectral feature. The signal-to-noise ratio for the strong lines in both spectra was about 5:1 and the precision of the line position measurement was about 0.0005 cm^{-1} for these lines. Since bromine has two nearly equally abundant isotopes with similar atomic mass, the rotational constants for both isotopomers of BrCNO are very close. This situation caused the spectra to be severely blended in many regions. The precision is, therefore, 0.001 cm^{-1} for the many blended and weak features.

In order to sort out the branches and to help in the assignment of the spectra, an interactive color Loomis-Wood computer program was utilized. The calibration of the ν_1 mode was carried out using the CO lines in the spectrum [125]. The ν_2 mode was calibrated with the water lines in the spectrum [126].

Figure 4.2 shows an overview of the high resolution spectrum of the ν_1 mode of

BrCNO. This mode overlaps with a mode of HCNO [127] on the high wavenumber side. while it overlaps with a mode of HNCO [128] on the low wavenumber side. Figure 4.3 shows a detailed portion of the R branch.

It is clear from Figure 4.2 that there are many lines from hot bands. This effectively obscured the position of the band origin of the fundamental mode. The difficulty in the analysis was further compounded by the presence of two different isotopomers. ^{79}BrCNO and ^{81}BrCNO.

The unambiguous J assignments of the ν_1 mode were accomplished with the help of a small local perturbation in the upper level at $J' = 60$ for ^{79}BrCNO and $J' = 61$ for ^{81}BrCNO. These assignments were confirmed by comparing the lower state combination differences of the ν_1 and ν_2 modes. The observed line positions of the two modes are listed in Tables C.1 and C.2.

Based on the appearance of the spectra. BrCNO molecule seemed to be linear. The rotational line positions of the two observed bands were fitted together using a least-squared fit program. The standard energy level expression

$$F(J) = \nu_0 + BJ(J+1) - D[J(J+1)]^2 \tag{4.1}$$

was used. The results are listed in Table 4.2.

The rotational analysis of the two vibrational modes as well as the previous low resolution infrared spectra and ab initio calculations [121] indicate that the BrCNO molecule is not bent: however. the possibility of quasi-linear behavior cannot be ruled out at this stage of the analysis. The two rotational constants obtained in this work (one for each isotopomer) are insufficient to provide the geometry of

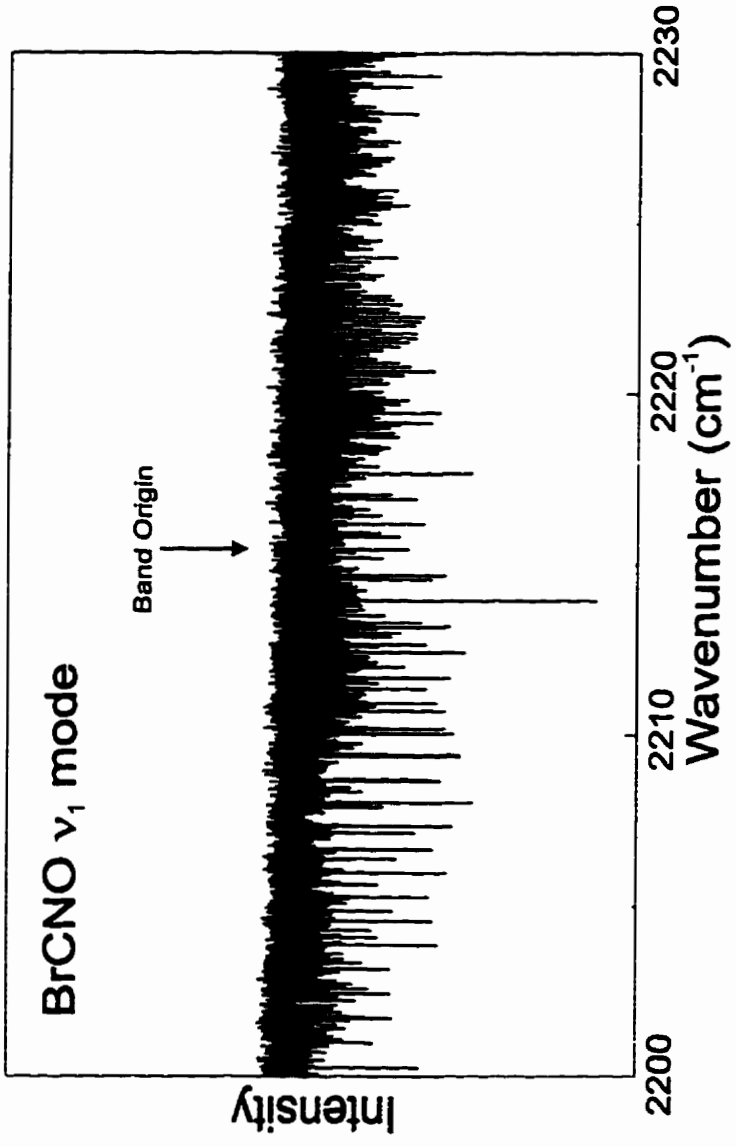

Figure 4.2: The overview of the high resolution spectrum of BrCNO ν_1 band

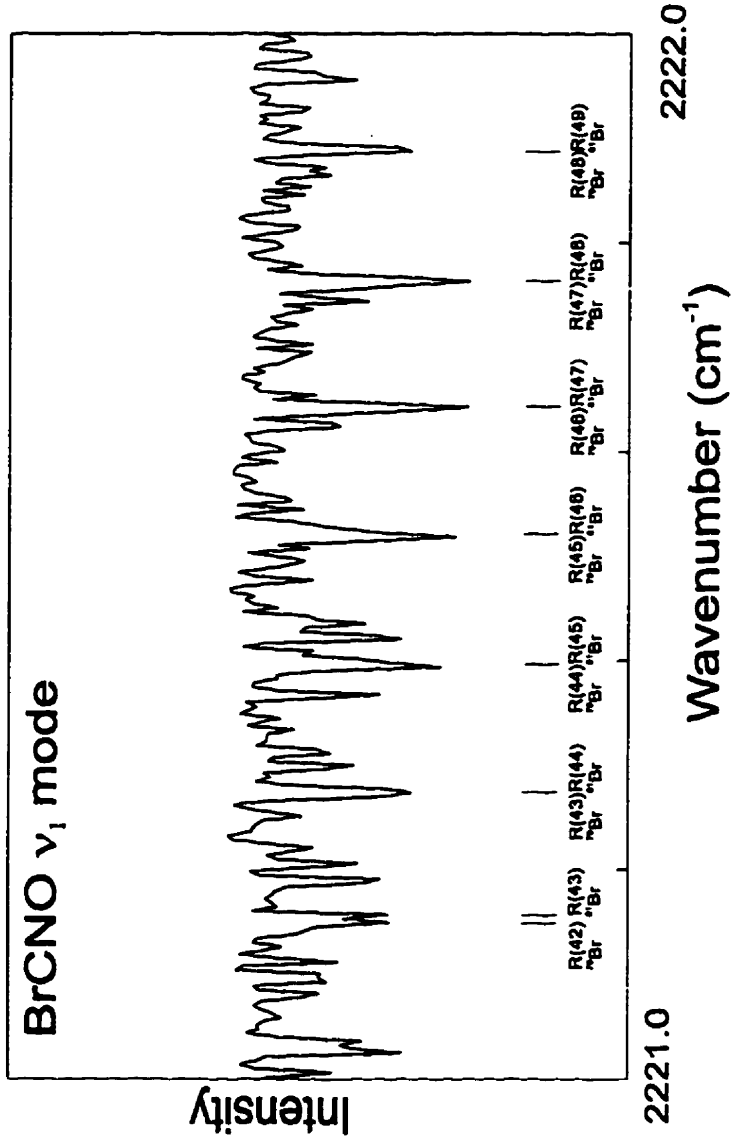

Figure 4.3: The expanded view of BrCNO ν_1 band R branch

Table 4.1: The spectroscopic constants for BrCNO (in cm^{-1}).

^{79}BrCNO

Level	E	B	D ($\times 10^{-9}$)
Lower State	0	0.0585152(11)	8.79(13)
ν_1	2215.99493(15)	0.0585825(11)	8.59(15)
ν_2	1323.32788(11)	0.0583208(11)	8.93(12)

^{81}BrCNO

Level	E	B	D ($\times 10^{-9}$)
Lower State	0	0.0580803(12)	8.61(15)
ν_1	2215.91256(19)	0.0581510(12)	8.91(17)
ν_2	1323.21591(12)	0.0578882(12)	8.81(14)

Values inside brackets are one standard deviation errors.

BrCNO without some assumptions. One approach to this problem is to assume a linear structure and to use the known NO bond length of the HCNO or CH_3CNO molecules. This, of course, assumes that the NO bond length is transferable from HCNO or CH_3CNO. The ab initio calculations of substituted nitrile oxides [129] have indicated that the NO bond length is less sensitive to substituent effects than that of CN. The calculations also indicate that the NO bond length in BrCNO is expected to be between that of HCNO and CH_3CNO. In Table 4.2, structures I and II show the structure of BrCNO predicted by this method, and also a comparison of the derived bond lengths with those of related molecules BrCCH, BrCN, HCNO, and CH_3CNO.

From Table 4.2 it can be seen that the BrC bond length derived from the B_0 rotational constants is anomalously short compared to that of BrCN and BrCCH, and the CN bond length is anomalously long compared to that of HCNO and CH_3CNO. This is similar to the case of HCNO, another floppy molecule, where an anomalously short CH bond length has been derived assuming a linear structure and a rigid bender model [132] (see Table 4.2). A reliable geometry and a good fit for the bending energy levels could only be achieved using the semi-rigid bender model, which makes possible the introduction of the bending angle dependencies of the bond lengths and bending reduced mass; these effects are important because of the large amplitude of the bending motion [133].

Clearly, experimental and theoretical studies on BrCNO have a long way to go before a full characterization will be achieved. To this end it is important to record the microwave and infrared spectra of isotopically substituted derivatives and to

Table 4.2: Comparison of the bond lengths in BrCNO (in Å).

Molecule	Method	Br-C	C-N	N-O	Comments
BrCCH	MW Ref. [130]	1.7916	-	-	r_S
BrCN	MW Ref. [131]	1.789	1.158	-	r_e [a]
BrCNO	B3-LYP	1.8007	1.1616	1.2041	r_e [b]
	struct. I	1.6843	1.2131	1.1994[c]	
	struct. II	1.6922	1.1915	1.2189[c]	
HCNO	MW Ref. [132]	(1.0266)[d]	1.1679	1.1994[c]	r_S [e]
	MW Ref. [133]	(1.060)[d]	1.16919	1.199	r_S [f]
CH_3CNO	MW Ref. [134]	-	1.1671	1.2189	r_S

a) 6-311G(2d) basis set used. molecule is quasi-linear at this level of theory.
b) 6-311G(2d) basis set used. molecule is linear at this level of theory.
c) fixed parameter.
d) C-H bond length.
e) structure derived from a linear model.
f) structure derived from a semi-rigid model.

include large amplitude effects in the structural analysis. To aid future workers, the equilibrium BrCN bending potential, and the dependence of bond lengths on the BrCN angle (Table 4.2) were calculated by Pasinszki.

4.3 Conclusion

The reactive BrCNO molecule can be produced in the gas phase by vacuum thermolysis of dibromoformaldoxime. The high resolution spectra of the two most intense vibrational modes have been recorded. The assumption that the structure of the molecule is linear, was made during the rotational analysis of these two modes. Due to the complexity of the spectra, only two bands have been analyzed, and several hot bands and the fundamental bands associated with these modes have yet to be analyzed.

The lower state B_0 constant is in good agreement with the ab initio prediction. The rotational constants were useful in the search for the microwave spectrum of BrCNO. Based on this work, microwave spectra of BrCNO were recorded by other workers. Preliminary results indicated that the bands analyzed here were not the fundamental bands. More analysis will be carried out to determine the fundamental infrared bands. Until the pure rotational spectrum is obtained and analyzed for several additional isotopomers, a reliable structure of BrCNO remains to be determined.

Table 4.3: Theoretical structure of BrCNO using the B3-LYP/6-311G(2d) method (bond lengths in Å, bond angles in degrees, total energy in atomic units).

Br-C-N	Br-C	C-N	N-O	C-N-O	Total Energy
180	1.7963	1.1587	1.2051	180	-2742.1498299
170	1.7993	1.1599	1.2048	177.31	-2742.1498611
165.35	1.8007	1.1616	1.2041	176.04	-2742.1498661
160	1.8050	1.1641	1.2029	174.78	-2742.1498231
150	1.8165	1.1705	1.2001	172.29	-2742.1493821
140	1.8322	1.1788	1.1964	170.39	-2742.1479620
130	1.8555	1.1882	1.1923	169.16	-2742.1449741

Chapter 5

Vibrational Spectroscopy of Polycyclic Aromatic Hydrocarbon Molecules

The vibrational motion of polyatomic molecules is, in general, very complicated. For a non-linear polyatomic molecular system consisting of n atoms, there are 3 degrees of freedom for translation, and another 3 degrees of freedom for rotation. Subtracting these from the total degrees of freedom, $3n$, the number of vibrational degrees of freedom is $3n-6$. To gain insight into the complex problem of molecular vibrations, a classical model is usually used. The molecule is approximated by a system of point particles with masses, which are held in their equilibrium positions by springs obeying Hooke's law. This model system has normal modes of vibration similar to the vibrating molecule.

5.1 Classical Mechanical Treatment of Molecular Vibration

The classical treatment [135] starts with the classical Hamiltonian given by

$$H = T + V, \tag{5.1}$$

where V is the potential energy and T is the kinetic energy, and

$$T = \frac{1}{2}\sum_i m_i(\dot{x}_i^2 + \dot{y}_i^2 + \dot{z}_i^2), \tag{5.2}$$

where $(\dot{x}_i, \dot{y}_i, \dot{z}_i)$ are a set of Cartesian coordinates of the ith particle, and the dot notation indicates derivative with respect to time, e.g. $\dot{x}_i = dx_i/dt$.

Next, the problem is expressed in terms of mass-weighted Cartesian coordinates q_i. The reason for this is that the amplitude of a particle's oscillation depends on its mass. When mass-weighted coordinates are used, all amplitudes are properly adjusted for the different masses of particles. Let

$$q_i = \sqrt{m_i}x_i. \tag{5.3}$$

Then the kinetic energy can be written as

$$T = \frac{1}{2}\sum_{i=1}^{3n}\dot{q}^2. \tag{5.4}$$

In general, the potential energy V is a complicated function of the Cartesian

coordinates of the atoms. For the purpose of vibrational spectroscopy, the molecule often oscillates with a small amplitude of vibration about the equilibrium position. The potential V can be expanded in a Taylor series in the neighborhood of the equilibrium position. The expansion is

$$V = V_0 + \sum_{i=1}^{3n} \frac{\partial V}{\partial q_i}|_{eq}\, q_i + \frac{1}{2}\sum_{i=1}^{3n}\sum_{j=1}^{3n} \frac{\partial^2 V}{\partial q_i \partial q_j}|_{eq}\, q_i\, q_j + \cdots \tag{5.5}$$

If the zero-point potential energy is chosen to be at the equilibrium, then $V_0 = 0$. By the definition of the equilibrium position, $\partial V/\partial q_i = 0$ at equilibrium. Ignoring the cubic and higher order expansion terms gives the harmonic approximation of the potential energy

$$V = \frac{1}{2}\sum_{i=1}^{3n}\sum_{j=1}^{3n} f_{ij}\, q_i\, q_j, \tag{5.6}$$

where

$$f_{ij} = \frac{\partial^2 V}{\partial q_i \partial q_j}|_{eq}. \tag{5.7}$$

In generalized coordinates, Lagrange's equations are the equivalent to Newton's law of motion. In classical mechanics, Lagrange's equation of motion is

$$\frac{d}{dt}\left(\frac{\partial L}{\partial \dot{q}_i}\right) - \frac{\partial L}{\partial q_i} = 0 \tag{5.8}$$

where L is the Lagrangian

$$L = T(\dot{q}_i) - V(q_i). \tag{5.9}$$

For the vibration of a molecule, substituting

$$L = T - V = \frac{1}{2}\sum_{i=1}^{3n} \dot{q}_i^{\,2} - \frac{1}{2}\sum_{i=1}^{3n}\sum_{j=1}^{3n} f_{ij} q_i dq_j \tag{5.10}$$

into Equation (5.8), the equation of motion becomes

$$\ddot{q}_i + \sum_{j=1}^{3n} f_{ij} dq_j = 0, \tag{5.11}$$

where $\ddot{q}_i$ denotes the second derivative of q with respect to time.

There are $3n$ coupled differential equations (5.11) with constant coefficients. Such a set of equations can be solved by assuming a solution of the form

$$q_i = A_i \cos(\sqrt{\lambda} t + \phi). \tag{5.12}$$

Substituting this solution into Equation (5.11) yields a set of $3n$ homogeneous linear equations

$$-\lambda A_i + \sum_{j=0}^{3n} f_{ij} A_j = 0. \tag{5.13}$$

The non-trivial solution of A_j exists only when the secular equation

$$|f_{ij} - \delta_{ij}\lambda| = 0 \tag{5.14}$$

is satisfied. The solution of this equation gives the eigenvalues λ_i, which are related to the vibrational frequencies of the system. It turns out that six of the eigenvalues are zero for a non-linear molecule. There are three degrees of freedom which are

associated with the translation of the center of mass, and three with rotational motion of the molecule as a whole. Since there is no restoring force acting on these degrees of freedom, their frequencies are zero.

There is a normal mode coordinate Q_i that is related to each eigenvalue λ_i. The set of a coordinates representing normal modes are related to the set of q_i by a linear transformation. The kinetic and potential energies can be written as

$$T = \frac{1}{2}\sum_i \dot{Q}_i^2, \tag{5.15}$$

$$V = \frac{1}{2}\sum_i \lambda_i Q_i^2. \tag{5.16}$$

Since both T and V have no cross-terms that connect different coordinates, the system behaves like a set a $3n-6$ independent harmonic oscillators, each oscillating at a frequency

$$\nu_i = \frac{\sqrt{\lambda_i}}{2\pi}. \tag{5.17}$$

When the higher order anharmonic terms of Equation (5.5) are considered, the normal mode approach is not entirely valid because the normal modes become coupled.

5.2 Quantum Mechanical Treatment of Molecular Vibration

The Born-Oppenheimer approximation is applied to separate the motion of the electrons and nuclei, and the validity of further separation of rotational motion from

vibrational motion is also assumed. Based on the previous classical description, the transition to quantum mechanical treatment is rather straight forward [11]. In normal mode coordinates, the classical Hamiltonian is translated to a quantum mechanical operator by making the usual substitutions

$$\begin{aligned} Q_i &\mapsto \mathbf{Q_i}, \\ P_i &\mapsto \mathbf{P_i} = -i\hbar\frac{\partial}{\partial Q_i}, \end{aligned}$$

where

$$P_i = \frac{\partial L}{\partial \dot{Q}_i} = \dot{Q}_i \tag{5.18}$$

is the classical generalized momentum associated with the normal coordinate Q_i. The quantum mechanical Hamiltonian for vibration is

$$\begin{aligned} \mathbf{H} &= -\frac{\hbar^2}{2}\sum_i \frac{\partial^2}{\partial Q_i^2} + \frac{1}{2}\sum_i \lambda_i \mathbf{Q_i}^2 \\ &= \sum_i \{-\frac{\hbar^2}{2}\frac{\partial^2}{\partial Q_i^2} + \frac{1}{2}\lambda_i \mathbf{Q_i}^2\} \\ &= \sum_i \mathbf{H_i}. \end{aligned} \tag{5.19}$$

In terms of normal coordinates, the Hamiltonian operator (5.19) is just a sum of $3n-6$ independent harmonic oscillator Hamiltonians. It follows that the vibrational wavefunction is just a product of $3n-6$ harmonic oscillator wavefunctions. The total vibrational energy is simply given by the sum of $3n-6$ harmonic oscillator energies:

$$E_{vib} = \sum_i^{3n-6} h\nu_i(v_i + \frac{1}{2}), \tag{5.20}$$

where v_i is the vibrational quantum number.

There are some limitations to this simple harmonic oscillator approach. The vibrational and rotational motions are not always separable. The Coriolis effect [136] is a result of the coupling between rotation and vibration. The separation of the total vibrational wavefunction into the product of wavefunctions associated with only one normal coordinate can break down under certain circumstances. This leads to phenomena such as Fermi resonance [9] and other types of mixing.

5.3 Group Frequencies

One of the most useful aspects of vibrational spectroscopy is the fact that a given group or bond in a molecule will produce spectral features that are characteristic of this group or bond. These spectral features are, therefore, often referred to as group frequencies [137]. Similar group-specific signatures are common in nuclear magnetic resonance, ultraviolet and visible spectroscopy, however, these techniques are qualitative analytical tools. Infrared spectroscopy also permits qualitative identification of compounds by examining their group vibrations. Furthermore, the group frequencies allow for an initial vibrational assignment.

For example, a single C-Br group, or bond produces a strong infrared absorption around 560 cm^{-1} [11], which is more or less independent of the rest of the molecule. This vibration is a group frequency typical of a C-Br group. However, if a molecule possesses two C-Br groups in close proximity, e.g., in a CBr_2 group, a symmetric and an antisymmetric Br-C-Br stretching mode are observed, in addition to a Br-C-Br bending vibration. All of the three are again characteristic group frequencies

of a CBr_2 group.

Although the discussion of molecular vibrations in terms of group vibrations may appear somewhat crude, particularly after the discussions of normal modes of vibration, it is amazing how well the group frequency approach holds, and how frequently it can be used for identification of compounds. For the detailed understanding of vibrational spectroscopy, it is worth noticing that a normal mode of vibration involves the entire molecule, but that the major contribution to a mode may involve just one group, which gives rise to the group frequency.

5.4 Selection Rules for Normal Modes of Vibration

The intensity of an infrared transition is given by the absolute square of the transition moment integral [31]

$$\mathbf{M} = \int \psi_f^* \, \mu \, \psi_i \, d\tau, \tag{5.21}$$

where ψ_f and ψ_i are final and initial vibrational wavefunctions within the same electronic state, μ is the dipole moment function, and the integral is over all vibrational coordinates. The transition moment must be nonzero for the transition to be allowed. The functional form of μ is often difficult to obtain, so it is expressed as a Taylor series expansion

$$\mu = \mu_0 + \sum_{k=1}^{3n-6} \left(\frac{\partial \mu}{\partial Q_k}\right)_{eq} Q_k + \cdots. \tag{5.22}$$

Now Equation (5.21) becomes

$$\mathbf{M} = \mu_0 \int \psi_f^* \, \psi_i \, dQ + \sum_{k=1}^{3n-6} \left(\frac{\partial \mu}{\partial Q_k}\right)_{eq} \int \psi_f^* \, Q_k \, \psi_i \, dQ + \cdots . \tag{5.23}$$

The first term on the right-hand side of the above expression is zero because the vibrational wavefunctions are orthogonal. The vibrational wavefunction is a product of $3n - 6$ harmonic oscillator wavefunctions, therefore, the ground state wavefunction consisting of the product of symmetric Gaussian functions is totally symmetric. For a fundamental vibrational transition, ψ_f differs from ψ_i only in the jth normal mode. Under the harmonic oscillator assumption, the symmetry of the excited state has the symmetry of Q_k itself. This becomes similar to a single harmonic oscillator, the selection rule is $\Delta v_i = \pm 1$. This is only a first order approximation since all the higher order terms are neglected.

From Equation (5.21) the integrand $\psi_f^* \, \mu \, \psi_i$ must be totally symmetric for allowed vibrational transitions. The symmetry of this integrand is $\Gamma(\psi_f^*) \otimes \Gamma(\mu) \otimes \Gamma(\psi_i)$ [138]. For a fundamental transition, ψ_i is totally symmetric while ψ_f^* has the symmetry of the jth normal mode, which is at excited level $v_j = 1$. This indicates that the symmetry of the integrand is

$$\Gamma(\psi_f^*) \bigotimes \Gamma(\mu) \bigotimes \Gamma(\psi_i) = \Gamma(\mu) \bigotimes \Gamma(\psi_i). \tag{5.24}$$

Because electric dipole moment operator is a vector with an expression

$$\mu = \mu_x \hat{\mathbf{i}} + \mu_y \hat{\mathbf{j}} + \mu_z \hat{\mathbf{k}}. \tag{5.25}$$

ψ_f must contain the representation of the symmetries of x, y, or z in order to have an infrared transition. Considerable amount of information of the normal modes of a molecule can be predicted on the basis of symmetries and group frequencies.

5.5 Polycyclic Aromatic Hydrocarbon Molecules in Astronomy

An important question in astronomy is the role of the polycyclic aromatic hydrocarbon (PAH) compounds in the chemistry of the interstellar medium. PAH molecules have been identified in meteorites [139,140] and interplanetary dust particles [141] by mass spectrometry. Several features in the spectra of astronomical objects have also been attributed to neutral or ionized PAHs. These features match the group frequencies of PAH molecules. One example is the unidentified infrared emission bands (UIRs) that are observed in the spectra of objects including planetary nebulae, reflection nebulae and H II regions [142–145]. It has been hypothesized that the UIRs arise because the PAH molecules absorb ultraviolet radiation, undergo internal conversion, and then emit radiation in the infrared region [142–145]. Indeed, the UIR bands (at 3.3 μm, 6.2 μm, 7.7 μm, 8.7 μm and 11.3 μm) [145] resemble some of the characteristic features in the PAH spectra. Other models propose that these features arise from molecular groups attached to carbonaceous dust grains [146], from quenched carbonaceous composites [147,148], or from a mixtures of PAHs and hydrogenated amorphous carbon [149,150].

The argument in favor of the PAH model is that the UIR bands cannot arise

from thermal emission as grains are too cold in most of the regions where these bands are observed. This is particularly true for the 3.3 μm emission band which implies a temperature of about 1000 K for the carriers. For an isolated molecule, such temperatures are easily achieved after the absorption of a single ultraviolet photon. After absorption of the photon, there is a fast internal conversion that converts electronic energy into ground state vibrational energy. Then the cooling process takes place through relatively slow infrared emission [143]. Although the observed UIR bands have characteristic frequencies of the vibrational modes of PAHs, a detailed study of these features is necessary to test the PAH hypothesis. In particular, no laboratory mixtures of PAH molecules have been able to simulate in detail, the observed infrared emission bands. This discrepancy has motivated both laboratory experiments and quantum mechanical calculations.

Schutte et al. [151] have modeled the UIR bands assuming that they are due to fluorescence from a distribution of PAHs embedded in the radiation field of a hot star. The distinct features in the spectra were predicted to occur from relatively small species of size less than 1000 carbon atoms, which upon excitation by absorbing an ultraviolet photon could emit radiation in the infrared. To determine whether the PAH model is valid, it is important to have reliable spectra of a large distribution of PAHs.

Several groups have recorded laboratory spectra of the PAHs in an attempt to assign the unidentified features in astronomical spectra. The easiest way to obtain infrared spectra of PAH molecules is to observe PAH molecules in the solid state or in solvents. Molecular crystals were dispersed in an ionic crystal pellet

(e.g. KBr, CsI) [152–154] or in a solvent (e.g. CCl_4, CS_2). Most of the presently available data on PAHs have been recorded under these conditions, either at room temperature [155] or at elevated temperatures [156, 157]. The major deficiency of these experiments is that the PAH molecules interact with each other in the crystal, and with pellet materials or solvents. The interactions may change the vibrational band positions and intensities. The rotational motion of PAH is quenched in the solid state, and is hindered in solvents.

Another experimental approach is to isolate PAH molecules in rare gas matrices. The vapor of PAH molecules is deposited on a window, which is usually made of KBr or CsI, together with rare gas atoms at temperatures below 20 K [158]. The rare gas atoms interact weakly with the PAH molecules. When the dilution ratio between rare gas atoms and PAHs is high, PAHs are well separated so that the interactions between PAHs are negligible. The vibrational band positions of PAH spectra recorded in matrices are close to those recorded in the gas phase, but the matrix effect is present, and is often difficult to predict. The rotational motion of the PAH molecules is also quenched in matrices at low temperature. The vibrational bands shapes are, therefore, different from those in gas phase spectra.

The interstellar environments that are thought to contain PAHs range from the surfaces of dust grains to the exploding shells of supernovae; this diversity must be approximated for by collecting spectra under a variety of experimental conditions. Thus, in recent years, research efforts were directed into studying PAH molecules in the gas phase. There are in general two ways to excite the vibrational modes of a PAH molecule. One method is direct heating of PAHs, while the other

involves laser ablation and ultraviolet laser excitation. In both cases, the infrared spectra can be recorded. The second technique is probably the best approach toward astronomical conditions, i.e. excitation by high energy ultraviolet photons [159,160]. Unfortunately, this approach was only applied to a small group of PAHs, and the measurements were limited to the spectral region near 3 μm. Saykally and co-workers [161, 162] have improved this technique, and they have measured the infrared emission spectra of naphthalene, perylene, pyrene, and coronene from 3 to 14 μm (3300 - 700 cm^{-1}) using a new infrared photon counting technique.

One most notable shortcoming in ultraviolet photon excitation experiments is that the level of infrared signal is low. There were situations where the infrared single photon counting technique was used. On the other hand, direct heating of PAH molecules can increase the population of vibrationally excited molecules dramatically, and consequently, the amount of infrared radiation emitted from the PAHs. Kurtz recorded the first gas-phase coronene spectra in the region between 400 and 3500 cm^{-1} using this method [163]. Infrared absorption spectra of several other gas-phase PAH molecules were obtained by Joblin et al. in the same wavelength region [164, 165].

To elucidate the chemistry of the PAHs in the interstellar medium, it is necessary to identify the individual PAH molecules. In principle, it is possible to distinguish among the different types of PAHs on the basis of their spectra. Yet the task is not a trivial one, because the PAHs exhibit very similar spectra in the mid-infrared, the region that contains most of the normal vibrational modes. The vibrational assignment, however, may be facilitated through theoretical methods.

Recently, Langhoff [38] calculated the infrared spectra of thirteen neutral and ionized PAH molecules using density functional theory. The calculations confirmed the previous assignments of the PAH spectra. Furthermore, Langhoff pointed out that the far-infrared region, which contains the vibrational frequencies associated with the bending of the aromatic rings, may provide a way to discriminate among the different molecules [38]. Because there were no available far-infrared spectra of isolated PAH molecules, this study was undertaken.

5.6 Laboratory Infrared Experiments on PAHs

In order to obtain the spectra of gas-phase PAH molecules, the mid-infrared and far-infrared emission and absorption were detected with a Fourier transform spectrometer. The use of thermal emission spectroscopy in addition to the traditional absorption technique is unusual [166], but we find emission spectroscopy to be more sensitive, even at long wavelengths. A cell consisting of a stainless steel tube 120 cm long, sealed with a window at each end, was used to contain the samples. The PAH solids were placed near the center of a quartz liner tube 100 cm long, which was inserted into the sample cell. After evacuation, a commercial furnace was used to heat the central 50 cm portion of the sample cell to produce PAH vapor. The two ends of the sample cell were water-cooled to protect the O-ring seals and to prevent deposition on the end windows. Appropriate optics and detectors were used to cover the spectral range from 50 to 4000 cm^{-1}.

Naphthalene, anthracene, pyrene, and chrysene solids (97% pure) were obtained from Aldrich and used without further purification. In every experiment, about 30

g of sample was placed in the central portion of a stainless steel tube lined with pyrex. The stainless tube was sealed with KRS-5 or polyethylene windows at both ends. The transmission range of KRS-5 window is from 250 to over 15 000 cm^{-1}, and that of polyethylene window is from 30 to 625 cm^{-1}. The sample cell was then evacuated. About 15 Torr of argon gas were introduced to the cell to prevent deposition of the sample onto the windows.

The sample was heated slowly up to a maximum of 450°C by a CM Rapid Temp furnace. Spectra were recorded about every 50°C separately in emission and absorption. For both the emission and absorption measurements, the infrared light was directed with a parabolic mirror through an external port of a Fourier transform spectrometer. The regions between the tube and the port were purged with dry nitrogen gas in order to minimize the effect from atmospheric contaminants such as CO_2 and H_2O. After each experiment, the remaining solid sample was analyzed by a mass spectrometer, and no decomposition product was detected.

A KBr beamsplitter (400 - 4800 cm^{-1}) was used for mid-infrared measurements, and a 3.5 μm thick Mylar beamsplitter (100 - 720 cm^{-1}) was used for far-infrared measurements. Liquid nitrogen-cooled MCT and InSb detectors as well as a liquid helium-cooled Si:B detector and a Si bolometer were used to record the spectra. The spectral resolution in all cases was 1 cm^{-1}. The integration time for each spectrum varied from 4 to 10 minutes, and the number of scans co-added ranged from 100 to 200. Background spectra were also recorded in a similar fashion but without a sample in the cell. The final spectra reported here were obtained by dividing the raw spectrum by the background spectrum taken at the same temperature.

5.7 Results

Emission and absorption spectra of gas-phase naphthalene, anthracene, chrysene, and pyrene were obtained over the interval from 50 to 4000 cm^{-1}. Although the spectra were recorded in both emission and absorption, the emission results are presented here because the emission technique provided a higher SNR for most modes, with less atmospheric contamination. Similar results were obtained in the infrared spectra of nucleic acid bases [39]. In PAH nomenclature, naphthalene and anthracene are classified as simple "linear" PAH molecules, chrysene is classified as a typical "non-linear" PAH molecule, and pyrene is classified as a simple compact PAH molecule [38]. The emission spectrum of pyrene in the region above 400 cm^{-1} is similar to the absorption spectrum reported by Joblin et al. [164, 165]. It was observed that there were several strong bands in the interval between 1700 and 2800 cm^{-1}, that must be combination bands because there are no infrared active fundamental transitions in this region. The unambiguous assignment of these vibrational modes is difficult, however, because the number of infrared active modes is large for even a small PAH molecule such as naphthalene. In addition, in the region from 400 to 1700 cm^{-1} where fundamental bands dominate, numerous combination and overtone bands are present. The general similarity between the mid-infrared spectra of different PAHs and the spectral complexity makes it difficult to differentiate between individual types of PAHs.

5.7.1 Far-infrared Region

Each PAH molecule, in contrast, has a relatively simple and characteristic spectrum in the region below 400 cm^{-1}. The far-infrared bands provide a unique fingerprint for each type of PAH. The far-infrared emission spectra of naphthalene, anthracene, pyrene, and chrysene, which are illustrated in Figures 5.1 to 5.4, were recorded at 350°C. Although the pure rotational lines of water are present in the spectra as an impurity, the profiles of the PAH bands can still be recognized. The effect of increasing temperature on the band position is less obvious, but a red-shift of the bands was noticed. Because the number of low-frequency infrared active modes is small, the far-infrared spectra (Figures 5.1, 5.2, 5.3 and 5.4) are less congested than the mid-infrared spectra. Tables 5.1 through 5.4 list the infrared bands of naphthalene, anthracene, pyrene, and chrysene that were measured in these experiments, together with theoretical calculations.

The agreement between the measured band positions and those calculated by Langhoff [38] is remarkably good. All of the relatively strong modes below 400 cm^{-1} that were reported by Langhoff were located in our experiments [38]. Although the far-infrared spectra of PAH molecules are relatively weak, they may provide a region where the different members of the PAH family can be uniquely identified. The far-infrared spectra reported here may help to test the PAH hypothesis for the origin of the unidentified infrared emission bands, as well as for other unassigned features in the spectra of astronomical objects. Although the earth's atmosphere is opaque in the far-infrared region, observations are possible with satellite-based infrared spectrometers such as the ISO, launched in late 1995, and the proposed

Space Infrared Telescope Facility (SIRTF) platform, which have orbits above the earth's atmosphere [167]. Observations will also be possible from high-flying aircraft platforms such as the Stratospheric Observatory for Infrared Astronomy (SOFIA), which will commence operations in the early part of the next century.

5.7.2 Mid-infrared Region

The mid-infrared region is rich in spectral features, and the interpretation of these bands can be difficult. This is illustrated in Figure 5.5. The PAH molecules that were studied have a large number of normal modes ranging from 48 for naphthalene to 84 for chrysene. The situation is made worse by the fact that the majority of the fundamental modes are in the range from 400 to 1800 cm^{-1}. Great care must be taken in the assignment of the mid-infrared spectra.

Molecular symmetry and selection rules play an important role in assigning the PAH spectra. Among the PAHs studied, naphthalene, anthracene and pyrene belong to the D_{2h} point group, and chrysene belongs to the C_{2h} point group. According to the character table, the D_{2h} group has six irreducible representations, which are A_g, A_u, B_{1g}, B_{1u}, B_{2g}, B_{2u}, B_{3g}, and B_{3u}; the C_{2h} group has four irreducible representations, which are A_g, A_u, B_g, and B_u [9]. From symmetry arguments, the product in Equation (5.24) must be totally symmetric to have a transition in the infrared. Since the electric dipole moment contains symmetries of x, y, and z, the modes that have infrared transitions must have the same symmetries. In the D_{2h} group, x, y, and z correspond to irreducible representations B_{1u}, B_{2u}, and B_{3u}; in the C_{2h} group, they correspond to A_u and B_u.

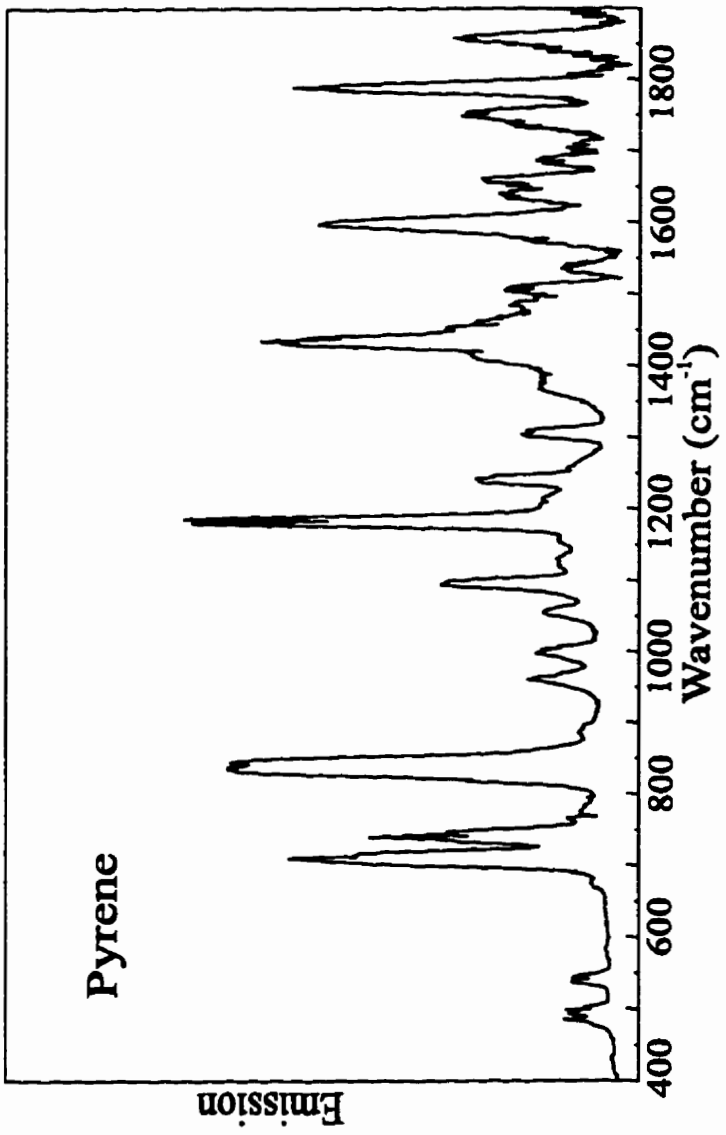

Figure 5.5: Mid-infrared emission spectra of gas-phase pyrene at 350°C. The spectrum was obtained with a liquid helium-cooled Si:B detector.

Table 5.1: Vibrational frequencies (in cm^{-1}) and intensities (in km/mol) of naphthalene.

Mode	Symmetry	Theoretical Frequency	Theoretical Intensity	Matrix Frequency	Gas Phase Frequency
ν_1	a_g	3078			
ν_2	a_g	3049			
ν_3	a_g	1561			
ν_4	a_g	1463			
ν_5	a_g	1364			
ν_6	a_g	1173			
ν_7	a_g	1020			
ν_8	a_g	752			
ν_9	a_g	512			
ν_{10}	a_u	987			
ν_{11}	a_u	839			
ν_{12}	a_u	629			
ν_{13}	a_u	185			
ν_{14}	b_{1g}	944			
ν_{15}	b_{1g}	719			
ν_{16}	b_{1g}	389			
ν_{17}	b_{1u}	3063	78.45	3064	
ν_{18}	b_{1u}	3043	8.89	3061	
ν_{19}	b_{1u}	1593	6.30	1601	1540
ν_{20}	b_{1u}	1400	3.18	1391	1385
ν_{21}	b_{1u}	1270	8.17	1269	1263
ν_{22}	b_{1u}	1132	3.16	1129	1128
ν_{23}	b_{1u}	797	0.25		798
ν_{24}	b_{1u}	361	1.25		352
ν_{25}	b_{2g}	994			
ν_{26}	b_{2g}	886			
ν_{27}	b_{2g}	772			
ν_{28}	b_{2g}	472			
ν_{29}	b_{2u}	3077	71.40	3078	
ν_{30}	b_{2u}	3045	1.35	3028	
ν_{31}	b_{2u}	1508	9.10	1515	1505
ν_{32}	b_{2u}	1358	1.54	1361	
ν_{33}	b_{2u}	1209	1.19	1214	1217

Table 5.1: *(Continued)* Vibrational frequencies (in cm^{-1}) and intensities (in km/mol) of naphthalene.

Mode	Symmetry	Theoretical Frequency	Theoretical Intensity	Matrix Frequency	Gas Phase Frequency
ν_{34}	b_{2u}	1170	1.23	1141	
ν_{35}	b_{2u}	1010	4.10	1012	1007
ν_{36}	b_{2u}	632	3.17	620	620
ν_{37}	b_{3g}	3061			
ν_{38}	b_{3g}	3042			
ν_{39}	b_{3g}	1619			
ν_{40}	b_{3g}	1462			
ν_{41}	b_{3g}	1256			
ν_{42}	b_{3g}	1155			
ν_{43}	b_{3g}	940			
ν_{44}	b_{3g}	513			
ν_{45}	b_{3u}	964	4.35	958	937
ν_{46}	b_{3u}	788	111.32	788	773
ν_{47}	b_{3u}	480	15.97	474	473
ν_{48}	b_{3u}	172	1.95		168

Table 5.2: Vibrational frequencies (in cm^{-1}) and intensities (in km/mol) of anthracene.

Mode	Symmetry	Theoretical Frequency	Theoretical Intensity	Matrix Frequency	Gas Phase Frequency
ν_1	a_g	3078			
ν_2	a_g	3049			
ν_3	a_g	3041			
ν_4	a_g	1541			
ν_5	a_g	1482			
ν_6	a_g	1385			
ν_7	a_g	1266			
ν_8	a_g	1181			
ν_9	a_g	1005			
ν_{10}	a_g	743			
ν_{11}	a_g	638			
ν_{12}	a_g	390			
ν_{13}	a_u	989			
ν_{14}	a_u	856			
ν_{15}	a_u	745			
ν_{16}	a_u	498			
ν_{17}	a_u	121			
ν_{18}	b_{1g}	956			
ν_{19}	b_{1g}	760			
ν_{20}	b_{1g}	476			
ν_{21}	b_{1g}	233			
ν_{22}	b_{1u}	3063	81.34	3062	3048
ν_{23}	b_{1u}	3044	18.69	3032	3048
ν_{24}	b_{1u}	3039	10.68	3022	
ν_{25}	b_{1u}	1620	7.88	1627	1625
ν_{26}	b_{1u}	1456	2.05	1460	
ν_{27}	b_{1u}	1311	1.96	1318	1315
ν_{28}	b_{1u}	1275	10.19	1272	1266
ν_{29}	b_{1u}	1156	4.70	1149	1149
ν_{30}	b_{1u}	908	1.67	908	
ν_{31}	b_{1u}	652	0.62	652	
ν_{32}	b_{1u}	232	1.29	260	
ν_{33}	b_{2g}	991			

Table 5.2: *(Continued)* Vibrational frequencies (in cm^{-1}) and intensities (in km/mol) of anthracene.

Mode	Symmetry	Theoretical Frequency	Theoretical Intensity	Matrix Frequency	Gas Phase Frequency
ν_{34}	b_{2g}	910			
ν_{35}	b_{2g}	836			
ν_{36}	b_{2g}	767			
ν_{37}	b_{2g}	584			
ν_{38}	b_{2g}	267			
ν_{39}	b_{2u}	3078	95.47	3068	3065
ν_{40}	b_{2u}	3048	0.01		
ν_{41}	b_{2u}	1534	4.95	1450	1536
ν_{42}	b_{2u}	1455	3.59	1450	1448
ν_{43}	b_{2u}	1383	0.07	1400	1392
ν_{44}	b_{2u}	1343	4.15	1346	1339
ν_{45}	b_{2u}	1169	0.98	1167	
ν_{46}	b_{2u}	1158	3.37	1151	
ν_{47}	b_{2u}	1001	3.20	1001	992
ν_{48}	b_{2u}	796	0.01		
ν_{49}	b_{2u}	613	7.53	603	601
ν_{50}	b_{3g}	3063			
ν_{51}	b_{3g}	3043			
ν_{52}	b_{3g}	1617			
ν_{53}	b_{3g}	1578			
ν_{54}	b_{3g}	1397			
ν_{55}	b_{3g}	1282			
ν_{56}	b_{3g}	1202			
ν_{57}	b_{3g}	1100			
ν_{58}	b_{3g}	918			
ν_{59}	b_{3g}	530			
ν_{60}	b_{3g}	391			
ν_{61}	b_{3u}	962	8.64	958	952
ν_{62}	b_{3u}	885	63.92	879	874
ν_{63}	b_{3u}	730	76.42	729	722
ν_{64}	b_{3u}	471	17.29	470	465
ν_{65}	b_{3u}	380	0.05		
ν_{66}	b_{3u}	91	1.03		

Table 5.3: Vibrational frequencies (in cm^{-1}) and intensities (in km/mol) of pyrene.

Mode	Symmetry	Theoretical Frequency	Theoretical Intensity	Matrix Frequency	Gas Phase Frequency
ν_1	a_g	3074			
ν_2	a_g	3063			
ν_3	a_g	3046			
ν_4	a_g	1618			
ν_5	a_g	1552			
ν_6	a_g	1390			
ν_7	a_g	1324			
ν_8	a_g	1241			
ν_9	a_g	1151			
ν_{10}	a_g	1066			
ν_{11}	a_g	803			
ν_{12}	a_g	577			
ν_{13}	a_g	406			
ν_{14}	a_u	974			
ν_{15}	a_u	895			
ν_{16}	a_u	678			
ν_{17}	a_u	395			
ν_{18}	a_u	151			
ν_{19}	b_{1g}	909			
ν_{20}	b_{1g}	804			
ν_{21}	b_{1g}	526			
ν_{22}	b_{1g}	247			
ν_{23}	b_{1u}	3074	95.82	3067	
ν_{24}	b_{1u}	3046	0.04		
ν_{25}	b_{1u}	3042	3.55		
ν_{26}	b_{1u}	1586	12.80	1598	1598
ν_{27}	b_{1u}	1445	0.53		
ν_{28}	b_{1u}	1427	11.82	1436	1433
ν_{29}	b_{1u}	1253	3.62	1243	1240
ν_{30}	b_{1u}	1092	4.75	1097	1095
ν_{31}	b_{1u}	997	0.55	1004	998
ν_{32}	b_{1u}	820	3.14	822	830
ν_{33}	b_{1u}	693	0.12	694	

Table 5.3: *(Continued)* Vibrational frequencies (in cm^{-1}) and intensities (in km/mol) of pyrene.

Mode	Symmetry	Theoretical Frequency	Theoretical Intensity	Matrix Frequency	Gas Phase Frequency
ν_{34}	b_{1u}	500	2.50	498	
ν_{35}	b_{2g}	985			
ν_{36}	b_{2g}	966			
ν_{37}	b_{2g}	827			
ν_{38}	b_{2g}	771			
ν_{39}	b_{2g}	579			
ν_{40}	b_{2g}	504			
ν_{41}	b_{2g}	259			
ν_{42}	b_{2u}	3063	94.69	3060	
ν_{43}	b_{2u}	3054	23.18	3008	
ν_{44}	b_{2u}	1597	5.53	1603	
ν_{45}	b_{2u}	1476	3.97	1493	
ν_{46}	b_{2u}	1428	1.21		
ν_{47}	b_{2u}	1315	6.50	1312	1305
ν_{48}	b_{2u}	1207	0.02		
ν_{49}	b_{2u}	1188	10.27	1184	1182
ν_{50}	b_{2u}	1161	1.68		
ν_{51}	b_{2u}	955	0.18		
ν_{52}	b_{2u}	549	2.47	542	540
ν_{53}	b_{2u}	354	1.37		395
ν_{54}	b_{3g}	3054			
ν_{55}	b_{3g}	3042			
ν_{56}	b_{3g}	1571			
ν_{57}	b_{3g}	1498			
ν_{58}	b_{3g}	1415			
ν_{59}	b_{3g}	1362			
ν_{60}	b_{3g}	1251			
ν_{61}	b_{3g}	1184			
ν_{62}	b_{3g}	1107			
ν_{63}	b_{3g}	739			
ν_{64}	b_{3g}	502			
ν_{65}	b_{3g}	456			
ν_{66}	b_{3u}	977	2.44	964	960
ν_{67}	b_{3u}	848	120.54	843	846

Table 5.3: *(Continued)* Vibrational frequencies (in cm^{-1}) and intensities (in km/mol) of pyrene.

Mode	Symmetry	Theoretical Frequency	Theoretical Intensity	Matrix Frequency	Gas Phase Frequency
ν_{68}	b_{3u}	747	9.94	745	741
ν_{69}	b_{3u}	711	32.02	712	711
ν_{70}	b_{3u}	491	1.48	488	491
ν_{71}	b_{3u}	210	7.30		207
ν_{72}	b_{3u}	99	0.45		95

Table 5.4: Vibrational frequencies (in cm^{-1}) and intensities (in km/mol) of chrysene.

Mode	Symmetry	Theoretical Frequency	Theoretical Intensity	Gas Phase Frequency
ν_1	a_g	3102		
ν_2	a_g	3085		
ν_3	a_g	3074		
ν_4	a_g	3056		
ν_5	a_g	3050		
ν_6	a_g	3045		
ν_7	a_g	1609		
ν_8	a_g	1599		
ν_9	a_g	1552		
ν_{10}	a_g	1520		
ν_{11}	a_g	1457		
ν_{12}	a_g	1437		
ν_{13}	a_g	1363		
ν_{14}	a_g	1356		
ν_{15}	a_g	1322		
ν_{16}	a_g	1260		
ν_{17}	a_g	1230		
ν_{18}	a_g	1186		
ν_{19}	a_g	1180		
ν_{20}	a_g	1141		
ν_{21}	a_g	1041		
ν_{22}	a_g	1016		
ν_{23}	a_g	874		
ν_{24}	a_g	770		
ν_{25}	a_g	680		
ν_{26}	a_g	572		
ν_{27}	a_g	481		
ν_{28}	a_g	378		
ν_{29}	a_g	289		
ν_{30}	a_u	989	0.14	1013
ν_{31}	a_u	959	0.22	
ν_{32}	a_u	947	4.03	947
ν_{33}	a_u	864	9.27	

Table 5.4: *(Continued)* Vibrational frequencies (in cm^{-1}) and intensities (in km/mol) of chrysene.

Mode	Symmetry	Theoretical Frequency	Theoretical Intensity	Gas Phase Frequency
ν_{34}	a_u	817	65.29	807
ν_{35}	a_u	763	96.68	747
ν_{36}	a_u	733	0.02	
ν_{37}	a_u	580	5.07	575
ν_{38}	a_u	555	2.19	533
ν_{39}	a_u	431	7.95	426
ν_{40}	a_u	289	0.13	
ν_{41}	a_u	233	4.34	236
ν_{42}	a_u	78	0.20	
ν_{43}	a_u	49	0.13	
ν_{44}	b_g	987		
ν_{45}	b_g	969		
ν_{46}	b_g	940		
ν_{47}	b_g	869		
ν_{48}	b_g	827		
ν_{49}	b_g	778		
ν_{50}	b_g	741		
ν_{51}	b_g	675		
ν_{52}	b_g	510		
ν_{53}	b_g	476		
ν_{54}	b_g	385		
ν_{55}	b_g	174		
ν_{56}	b_g	135		
ν_{57}	b_u	3101	68.44	
ν_{58}	b_u	3085	16.87	
ν_{59}	b_u	3074	84.69	
ν_{60}	b_u	3057	44.69	
ν_{61}	b_u	3049	20.17	
ν_{62}	b_u	3045	0.84	
ν_{63}	b_u	1607	2.00	1614
ν_{64}	b_u	1589	8.17	1595
ν_{65}	b_u	1515	9.39	
ν_{66}	b_u	1485	8.65	1481
ν_{67}	b_u	1434	4.74	

Table 5.4: *(Continued)* Vibrational frequencies (in cm^{-1}) and intensities (in km/mol) of chrysene.

Mode	Symmetry	Theoretical Frequency	Theoretical Intensity	Gas Phase Frequency
ν_{68}	b_u	1426	10.25	1425
ν_{69}	b_u	1348	2.67	
ν_{70}	b_u	1303	0.01	
ν_{71}	b_u	1263	15.88	1258
ν_{72}	b_u	1240	2.97	1231
ν_{73}	b_u	1196	2.33	
ν_{74}	b_u	1171	2.79	1187
ν_{75}	b_u	1158	0.46	1147
ν_{76}	b_u	1078	0.42	1088
ν_{77}	b_u	1032	6.86	1031
ν_{78}	b_u	877	3.61	876
ν_{79}	b_u	850	2.21	856
ν_{80}	b_u	685	10.99	680
ν_{81}	b_u	571	0.78	
ν_{82}	b_u	538	2.10	
ν_{83}	b_u	480	8.49	477
ν_{84}	b_u	185	0.48	

The selection rules for combination and overtone modes can be derived in a similar manner. The symmetry of a combination or overtone mode is obtained by taking the direct product of the symmetries of the fundamental modes involved. For example, the symmetry of a combination mode involving fundamental modes i and j is

$$\Gamma(\psi_{comb}) = \Gamma(\psi_i) \bigotimes \Gamma(\psi_j). \tag{5.26}$$

The direct products for different symmetry groups are usually listed in textbooks [11]. It is interesting to notice that g-u selection rules are

$$g \times g = g, \quad g \times u = u, \quad u \times u = g.$$

Since the infrared active modes of the D_{2h} and C_{2h} groups all have u symmetry, all the first overtone vibrations are not allowed.

It is conventional to use lower case letters to indicate the symmetries of normal modes, i.e. b_{1u} instead of B_{1u}. The normal vibrational modes are listed in Tables 5.1 - 5.4, together with matrix frequencies and gas phase frequencies from this study. The C-H stretching region near 3300 cm^{-1} is too congested to make assignments. In general, the data obtained from this study are in good agreement with theoretical calculations and matrix data. Because of broadening of bands at high temperatures, gas phase bands are not as well defined as matrix bands.

It is noticed that the calculations for naphthalene, anthracene, and pyrene are closer to experimental values, while those for chrysene are in general inferior. Nevertheless, the agreement between experiments and ab initio calculations is remarkable. This is especially so in the far-infrared region where the theoretical predictions are

Table 5.5: Frequencies of combination bands of PAHs in cm^{-1}.

Frequency (cm^{-1})	Assignment
Naphthalene	
825	$\nu_{28} + \nu_{24}$
953	$\nu_{28} + \nu_{47}$
758	$\nu_{16} + \nu_{24}$
1658	$\nu_{15} + \nu_{45}$, $\nu_{26} + \nu_{46}$
1715	$\nu_{43} + \nu_{46}$, $\nu_{14} + \nu_{46}$
1835	$\nu_{5} + \nu_{24}$
1895	$\nu_{16} + \nu_{31}$, $\nu_{44} + \nu_{20}$, $\nu_{26} + \nu_{35}$
1933	$\nu_{15} + \nu_{33}$, $\nu_{25} + \nu_{45}$, $\nu_{40} + \nu_{47}$
Anthracene	
1671	$\nu_{56} + \nu_{64}$
1698	$\nu_{18} + \nu_{15}$, $\nu_{57} + \nu_{49}$
1763	$\nu_{36} + \nu_{47}$
1786	$\nu_{60} + \nu_{43}$, $\nu_{12} + \nu_{43}$
1811	$\nu_{20} + \nu_{44}$, $\nu_{14} + \nu_{18}$
1843	$\nu_{59} + \nu_{27}$
1904	$\nu_{37} + \nu_{27}$, $\nu_{11} + \nu_{28}$
1932	$\nu_{12} + \nu_{41}$, $\nu_{60} + \nu_{41}$
Pyrene	
1055	$\nu_{36} + \nu_{72}$
315	$\nu_{22} + \nu_{72}$
1409	$\nu_{12} + \nu_{32}$
1638	$\nu_{65} + \nu_{49}$, $\nu_{9} + \nu_{70}$
1659	$\nu_{37} + \nu_{32}$
1685	$\nu_{40} + \nu_{49}$
1736	$\nu_{63} + \nu_{31}$
1751	$\nu_{19} + \nu_{67}$
1787	$\nu_{37} + \nu_{66}$

Table 5.5: *(Continued)* Frequencies of combination bands of PAHs in cm^{-1}.

Frequency (cm^{-1})	Assignment
1912	$\nu_{10} + \nu_{67}$
1928	$\nu_{36} + \nu_{66}$
Chrysene	
1683	$\nu_{48} + \nu_{79}$
1721	$\nu_{26} + \nu_{75}$
1745	$\nu_{47} + \nu_{78}$
1771	$\nu_{55} + \nu_{64}$
1819	$\nu_{51} + \nu_{75}$
1881	$\nu_{29} + \nu_{64}$
1906	$\nu_{27} + \nu_{68}$
1938	$\nu_{25} + \nu_{71}$

within 10 cm^{-1}.

After the far-infrared bands were assigned, it became possible to assign some of the combination bands. Tentative assignments are given for combination bands located below 2000 cm^{-1}. This region is chosen to simplify the assignments. It is noted that from symmetry arguments that first overtone transitions are not allowed. All combination bands below 2000 cm^{-1} are considered to be combinations of two fundamental modes, and the combination scheme for higher frequency bands is more complicated and more difficult to predict. The assignments are listed in Table 5.5. It is assumed that a strong infrared mode combined with an infrared inactive mode with g symmetry may produce a band with noticeable intensity. For the D_{2h} group, the a_u mode is neither infrared nor Raman active, but when it is combined with a b_{1g}, b_{2g}, or b_{3g} mode, the resulting combination band becomes infrared active. However, there is no simple way of predicting its intensity. Some combination bands may result from more than one combination mode: such possibilities are also listed in Table 5.5. Because of a lack of symmetry, chrysene has many relatively strong fundamental infrared modes, and the assignments of its combination bands are not very reliable. For completeness, all the observed band positions are listed in Table 5.6. The widths of most bands are also included.

It is concluded that the family of PAH molecules can be identified on the basis of their mid-infrared spectra. However, to further distinguish among the individual PAH species, the far-infrared spectra must be used to complement the mid-infrared results. It is also established that the infrared emission technique is applicable to large molecules, such as the PAH molecules. Finally, the infrared emission technique

is superior to infrared absorption, as most clearly observed.

Table 5.6: Observed band positions of PAHs.

Band	Frequency (cm^{-1})	Width (cm^{-1})
Naphthalene		
comb	825	5.6
comb	953	15.7
ν_{24}	352	17.9
ν_{23}	798	8.2
ν_{22}	1128	32.1
ν_{21}	1263	20.0
ν_{20}	1385	28.7
ν_{19}	1540	15.5
comb	758	11.9
ν_{36}	620	23.1
ν_{35}	1007	22.8
ν_{31}	1505	32.7
ν_{48}	168	29.7
ν_{47}	473	32.9
ν_{46}	773	60.0
ν_{45}	937	16.7
comb	1658	
comb	1715	18.7
comb	1835	8.3
comb	1895	
comb	1933	
Anthracene		
ν_{29}	1149	24.1
ν_{28}	1266	10.5
ν_{27}	1315	
ν_{25}	1625	22.2
ν_{49}	601	
ν_{47}	992	17.0
ν_{44}	1339	

† Unassigned combination bands.

Table 5.6: *(Continued)* Observed band positions of PAHs.

Band	Frequency (cm^{-1})	Width (cm^{-1})
ν_{43}	1392	9.9
ν_{42}	1448	17.8
ν_{41}	1536	17.6
ν_{64}	465	18.1
ν_{63}	722	18.9
ν_{62}	874	21.8
ν_{61}	952	10.3
comb	1671	18.3
comb	1698	9.9
comb	1763	12.7
comb	1786	14.8
comb	1811	12.6
comb	1843	17.7
comb	1904	27.1
comb	1932	17.3
comb †	2015	
comb †	2288	21.8
comb †	2326	45.6
comb †	2537	16.8
Pyrene		
comb	1055	12.3
comb	315	
ν_{32}	830	19.2
ν_{31}	998	14.9
ν_{30}	1095	15.1
ν_{29}	1240	12.9
ν_{28}	1433	21.2
ν_{26}	1598	21.5
ν_{53}	395	16.35
ν_{52}	540	14.4
ν_{49}	1182	15.7
ν_{47}	1305	15.1

† Unassigned combination bands.

Table 5.6: *(Continued)* Observed band positions of PAHs.

Band	Frequency (cm^{-1})	Width (cm^{-1})
comb	1409	6.1
ν_{72}	95	1.2
ν_{71}	207	19.8
ν_{70}	491	22.2
ν_{69}	711	23.2
ν_{68}	741	13.9
ν_{67}	846	17.3
ν_{66}	960	12.9
comb	1638	
comb	1659	
comb	1685	
comb	1736	13.6
comb	1751	15.1
comb	1787	15.9
comb	1912	18.1
comb	1928	15.7
comb †	2240	17.1
comb †	2280	31.1
comb †	2356	22.8
comb †	2496	27.3
comb †	2610	
comb †	2664	20.0
Chrysene		
ν_{32}	236	15.9
ν_{39}	426	20.8
ν_{38}	533	12.3
ν_{37}	575	20.1
ν_{35}	747	
ν_{34}	807	16.4
ν_{32}	947	19.7
ν_{30}	1013	14.6

† Unassigned combination bands.

Table 5.6: *(Continued)* Observed band positions of PAHs.

Band	Frequency (cm^{-1})	Width (cm^{-1})
comb	898	
ν_{83}	477	11.8
ν_{80}	680	12.5
ν_{79}	856	14.8
ν_{78}	876	21.8
ν_{77}	1031	14.8
ν_{76}	1088	
ν_{75}	1147	
ν_{74}	1187	13.0
ν_{72}	1231	36.0
ν_{71}	1258	17.9
ν_{68}	1425	23.0
ν_{66}	1481	10.4
ν_{64}	1595	4.4
ν_{63}	1614	
comb	1683	21.1
comb	1721	7.3
comb	1745	6.2
comb	1771	14.0
comb	1819	20.2
comb	1881	15.0
comb	1906	28.6
comb	1938	16.0
comb †	2451	10.6
comb †	2468	16.5
comb †	2504	15.6
comb †	2548	10.3
comb †	2586	25.5

† Unassigned combination bands.

References

1. *Infrared Spectroscopy of Biomolecules*, edited by J. Liquier and E. Taillandier (Wiley-Liss, New York, 1996).

2. *High Resolution Infrared Remote Sensing for Earth's Weather and Climate Studies*, edited by A. Chedin, M.T. Chahine and N.A. Scott (Springer-Verlag, Berlin, 1993).

3. E. Hirota and K. Kawaguchi, Annu. Rev. Phys. Chem. **36**, 53 (1985).

4. *The Infrared Spectral Region of Stars*, edited by C. Jaschek and Y. Andrillat (Cambridge University Press, Cambridge, 1991).

5. *The Impact of Very High S/N Spectroscopy on Stellar Physics*, edited by G.C. de Strobel and M. Spite (Kluwer Acadamic Publishers, Paris, 1987).

6. D.K. Killinger and A. Mooradian, *Optical and Laser Remote Sensing* (Springer-Verlag, Berlin, 1983).

7. G. Stephens, *Remote Sensing of the Lower Atmosphere* (Oxford University Press, Oxford, 1994).

8. J. Hollas, *High Resolution Spectroscopy* (Butterworths, London, 1982).

9. G. Herzberg, *Molecular Spectra and Molecular Structure* (Krieger Publishing Company, Florida, 1991).

10. P. Bernath, Annu. Rev. Phys. Chem. **41**, 91 (1990).

11. P. Bernath, *Spectra of Atoms and Molecules* (Oxford University Press, Oxford, 1995).

12. M. Birk and J.W. Brault, Mikrochim. Acta **2**, 243 (1988).

13. L. Wallace, P. Bernath, W. Livingston, K. Hinkle, J. Busler, B. Guo and K. Zhang, Science **268**, 1158 (1995).

14. E. Hirota, J. Phys. Chem. **87**, 3375 (1983).

15. E. Hirota, Vib. Spectra Struct. **14**, 1 (1985).

16. E. Hirota and S. Saito, Rev. Chem. Intermed. **7**, 353 (1987).

17. *Ion Cluster and Ion Spectroscopy and Structure*, edited by J. Maier (Elsevier, Amsterdam, 1989).

18. N.B. Colthup, L.H. Daly and S.E. Wiberley, *Introduction to Infrared and Raman Spectroscopy* (Academic Press, San Diego, 1990).

19. A. Haefner, K. Norton, P. Griffiths, S. Bourne and R. Curbelo, Anal. Chem. **60**, 2441 (1988).

20. R. Beer, *Remote Sensing by Fourier Transform Spectrometry* (Wiley, New York, 1992).

21. M. Low and S. Freeman, Anal. Chem. **39**, 194 (1967).

22. P. Wang, S. Lacele and H. Yazdi, Appl. Spec. **47**, 1830 (1993).

23. H. Lefebvre-Brion and R.W. Field, *Perturbations in the Spectra of Diatomic Molecules* (Academic Press, London, 1984).

24. W. Kolos and L. Wolniewicz, J. Chem. Phys. **41**, 3663 (1964).

25. M.S. Child and D.J. Nesbitt, Chem. Phys. Lett. **149**, 404 (1988).

26. D.J. Nesbitt, M.S. Child and D.C. Clary, J. Chem. Phys. **90**, 4855 (1989).

27. M. Born and R. Oppenheimer, Annal. Phys. **26**, 30 (1927).

28. J. van Vleck, J. Chem. Phys. **4**, 327 (1936).

29. R. Herman and A. Asgharian, J. Mol. Spec. **19**, 305 (1966).

30. P. Bunker, J. Mol. Spec. **42**, 478 (1972).

31. I. Levine, *Quantum Chemistry, 4th edition* (Allyn and Bacon, Boston, 1991).

32. J. Dunham, Phys. Rev. **41**, 721 (1932).

33. P. Bunker and R. Moss, Mol. Phys. **33**, 417 (1977).

34. J.A. Coxon and P.G. Hajigeorgiou, Can. J. Phys. **70**, 40 (1992).

35. J.A. Coxon and P.G. Hajigeorgiou, Chem. Phys. **167**, 327 (1992).

36. J.A. Coxon and P.G. Hajigeorgiou, J. Mol. Spec. **150**, 1 (1991).

37. K. Zhang, B. Guo, P. Colarusso and P. Bernath, Science **274**, 582 (1996).

38. S. Langhoff, J. Phys. Chem. **100**, 2819 (1996).

39. P. Colarusso, K. Zhang, B. Guo, and P. Bernath, Chem. Phys. Lett. (in press) (1996).

40. E. Hirota, *High Resolution Spectroscopy of Transient Molecules* (Springer-Verlag, Berlin, 1985).

41. A. Maki, J. Mol. Spec. **102**, 361 (1983).

42. H. Jones and J. Lindenmayer, Chem. Phys. Lett. **135**, 189 (1987).

43. J. Bell, *Introductory Fourier Transform Spectroscopy* (Academic Press, London, 1971).

44. *Vibrational Spectra and Structure vol. 19*, edited by J. Durig (Elsevier, Amsterdam, 1988).

45. P.R. Griffiths and J.A. de Haseth, *Fourier Transform Infrared Spectroscopy* (Wiley, New York, 1986).

46. J.C. Hill and G.P. Montgomery, App. Opt. **15**, 748 (1976).

47. C.B. Carlisle, D.E. Cooper and H. Preier, App. Opt. **13**, 2567 (1989).

48. A.G. Robiette and J.L. Duncan, Annu. Rev. Phys. Chem. **34**, 245 (1983).

49. J. Brault, Philos. Trans. R. Soc. London Ser. A **307**, 503 (1982).

50. A. Michelson, Phil. Mag. **31**, 256 (1891).

51. A. Michelson, *Light Waves and Their Uses* (University of Chicago Press, Chicago, 1902).

52. A. Michelson, *Studies in Optics* (University of Chicago Press, Chicago, 1927).

53. J. Cooley and J. Tukey, Math. Comput. **19**, 297 (1965).

54. J. van Vleck, Phys. Rev. **33**, 467 (1929).

55. R.M. Dale, R. Herman, J.W.C. Johns, A.R.W. McKellar, S. Nagler and I.M. Strathy, Can. J. Phys. **57**, 677 (1979).

56. A. Ross, R. Eng and H. Kildal, Opt. Comm. **12**, 433 (1974).

57. J. Watson, J. Mol. Spec. **80**, 411 (1980).

58. J. Watson, J. Mol. Spec. **45**, 99 (1973).

59. P. Bunker, J. Mol. Spec. **68**, 367 (1977).

60. E. Tiemann, H. Arnet, W.U. Stieda, T. Torring and J. Hoeft, Chem. Phys. **67**, 133 (1982).

61. E. Tiemann, J. Mol. Struct. **97**, 331 (1983).

62. J. Schlembach and E. Tiemann, Chem. Phys. **68**, 21 (1982).

63. H. Knockel and E. Tiemann, Chem. Phys. **68**, 13 (1982).

64. E. Tiemann, H. Knockel and J. Schlembach, Ber. Bunsenges. Phys. Chem. **86**, 821 (1982).

65. R. LeRoy and J. van Kranendonk, J. Chem. Phys. **61**, 4750 (1974).

66. W. Kosman and J. Hinze, J. Mol. Spec. **56**, 92 (1975).

67. G.C. Maitland, M. Rigby, E.B. Smith and W.A. Wakeham, *Intermolecular Forces: Their Origin and Determination* (Clarendon Press, Oxford, 1981).

68. H.G. Hedderich, M. Dulick and P.F. Bernath, J. Chem. Phys. **99**, 8363 (1993).

69. J.M. Campbell, M. Dulick, D. Klapstein, J.B. White and P.F. Bernath, J. Chem. Phys. **99**, 8379 (1993).

70. J.B. White, M. Dulick and P.F. Bernath, J. Chem. Phys. **99**, 8371 (1993).

71. R. Dull, Phys. Rev. **47**, 458 (1935).

72. M. Chretien and E. Miescher, Nature **163**, 996 (1949).

73. M. Chretien, Phys. Acta **23**, 259 (1950).

74. R. Onaka, J. Chem. Phys. **27**, 374 (1957).

75. R.F. Barrow, D. Premaswarup, J. Winternitz and P.B. Zeeman, Proc. Phys. Soc. A **71**, 61 (1958).

76. D. Robinson, J. Mol. Spec. **11**, 275 (1963).

77. S. Krishnamachari and M. Singh, Current Sci. **34**, 655 (1965).

78. J. Czarny and P. Felenbok, Chem. Phys. Lett. **2**, 533 (1968).

79. R. Caton and A. Douglas, Can. J. Phys. **48**, 432 (1970).

80. A.C. Le Floch, J. Lebreton, F. Launay, J. Ferran and J. Rostas, J. Phys. B **13**, 3989 (1980).

81. H. Bredohl, I. Dubois, F. Melen and M. Vervloet, J. Mol. Spec. **129**, 145 (1988).

82. D. Hildenbrand, Int. J. Mass Spectrom. Ion Phys. **7**, 255 (1971).

83. J.M. Dyke, C. Kirby and A. Morris, J. Chem. Soc., Faraday Trans. 2 **79**, 483 (1983).

84. F. Lovas and D. Johnson, J. Chem. Phys. **55**, 41 (1971).

85. G. Cazzoli, L. Cludi, C.D. Esposti and L. Dore, J. Mol. Spec. **134**, 159 (1989).

86. T. Nakanaga, H. Takeo, S. Kondo and C. Matsumura, Chem. Phys. Lett. **114**, 88 (1985).

87. M. Zahniser and M. Gersh, J. Chem. Phys. **75**, 52 (1981).

88. R. Nesbet, J. Chem. Phys. **40**, 3619 (1964).

89. R. Nesbet, J. Chem. Phys. **43**, 4403 (1965).

90. W. Huo, J. Chem. Phys. **43**, 624 (1965).

91. H. Lefebvre-Brion and C. Moser, J. Mol. Spec. **15**, 211 (1965).

92. H. Kurtz and K. Jordon, Chem. Phys. Lett. **81**, 104 (1981).

93. H. W. P. Rosmus and M. Grimm, Chem. Phys. Lett. **92**, 250 (1982).

94. P. Botschwina, J. Mol. Spec. **118**, 76 (1986).

95. M. Honigmann, G. Hirsch and R.J. Buenker, Chem. Phys. **172**, 59 (1993).

96. F. Charron, B. Guo, K. Zhang, Z. Morbi and P.F. Bernath, J. Mol. Spec. **171**, 160 (1995).

97. R. LeBlanc, J. White and P. Bernath, J. Mol. Spec. **164**, 574 (1994).

98. H.G. Hedderich, M. Dulick and P.F. Bernath, J. Chem. Phys. **99**, 8363 (1993).

99. K. Huber and G. Herzberg, *Constants of Diatomic Molecules* (Van Nostrand-Reinhold, New York, 1979).

100. H. Hedderich and P. Bernath, J. Mol. Spec. **153**, 73 (1992).

101. *Molecular Spectroscopy: Modern Research, vol. 3*, edited by R. Rao (Academic Press, New York, 1985).

102. E. Whiting, A. Schadee, J. Tatum, J. Hougen and R. Nicholls, J. Mol. Spec. **80**, 249 (1980).

103. Ch. Ryzlewicz, H.U. Schutze-Pahlmann, J. Hoeft, and T. Torring, Chem. Phys. **71**, 389 (1982).

104. K. Moller, H.U. Schutze-Pahlmann, J. Hoeft, and T. Torring, Chem. Phys. **82**, 399 (1982).

105. Y. Azuma, W.J. Childs, G.L. Goodman and T.C. Steimle, J. Chem. Phys. **93**, 5533 (1990).

106. W.J. Childs and L.S. Goodman, Phys. Rev. Lett. **44**, 316 (1980).

107. R. Barrow and J. Beale, Proc. Phys. Soc. **91**, 483 (1967).

108. M.A. Anderson, M.D. Allen and L.M. Ziurys, J. Chem. Phys. **100**, 824 (1994).

109. M.A. Anderson, M.D. Allen and L.M. Ziurys, Astrophys. J. Lett. **425**, 53 (1994).

110. L. Knight Jr., W. Easley, W. Weltner Jr. and M. Wilson, J. Chem. Phys. **54**, 322 (1971).

111. A.D. Buckingham and R.M. Olegario, Chem. Phys. Lett. **212**, 253 (1993).

112. T. Torring, W.E. Ernst and S. Kindt, J. Chem. Phys. **81**, 4614 (1984).

113. T. Torring, W.E. Ernst and J. Kandler, J. Chem. Phys. **90**, 4927 (1989).

114. C. Bauschlicher Jr., S. Langhoff, T. Steimle and J. Shirley, J. Chem. Phys. **93**, 4179 (1990).

115. S. Meth, R.J. Bartlett and M. Nooijen, private communication .

116. K. Zhang, B. Guo, V. Braun, M. Dulick and P.F. Bernath, J. Mol. Spec. **170**, 82 (1995).

117. C. Grundmann and P. Grunanger, *The Nitrile Oxides: Versatile Tools of Theoretical and Preparative Chemistry* (Springer-Verlag, Berlin, 1971).

118. A. Padwa, *1,2-Cycloaddition Chemistry* (Wiley, New York, 1984).

119. H. Feuer, *Nitrile Oxides, Nitrones, and Nitronates in Organic Synthesis* (VCH Publishers, Inc., New York, 1988).

120. G. Maier and J. Teles, Angew Chem. Int. Ed. Engl. **26**, 155 (1987).

121. T. Pasinszki and N.P.C. Westwood, J. Phys. Chem. **99**, 6401 (1995).

122. B. Guo, T. Pasinszki, N.P.C. Westwood and P. Bernath, J. Phys. Chem. **103**, 3335 (1995).

123. B. Guo, T. Pasinszki, N.P.C. Westwood, K. Zhang and P. Bernath, J. Chem. Phys. **105**, 4457 (1996).

124. Th. Brupbacher, R. Bohn, W. Jager, M.C.L. Gerry, T. Pasinszki and N.P.C. Westwood, J. Mol. Spec. **181**, 316 (1997).

125. A. Maki and J. Wells, Wavenumber Calibration Tables from Heterodyne Frequency Measurements, NIST Special Publication 821 (1991).

126. Toth, J. Opt. Soc. Am. B **8**, 2236 (1991).

127. E. Ferretti and R. Rao, J. Mol. Spec. **51**, 97 (1974).

128. D. Steiner, S. Polo, T. McCubbin and K. Wishah, J. Mol. Spec. **98**, 453 (1983).

129. T. Pasinszki and N.P.C. Westwood, unpublished results .

130. H. Jones, J. Sheridan and O.L. Stiefvater, Z. Naturforsch. **32**, 866 (1977).

131. J. Tyler and J. Sheridan, Trans. Faraday Soc. **59**, 2661 (1963).

132. B.P. Winnewisser, M. Winnewisser and F. Winther, J. Mol. Spec. **51**, 65 (1974).

133. P.R. Bunker, B.M. Landsberg and B.P. Winnewisser, J. Mol. Spec. **74**, 9 (1979).

134. P. Blackburn, R.D. Brown, F. Burden, J. Crofts and I.. Gillard, Chem. Phys. Lett. **7**, 102 (1970).

135. H. Goldstein, *Classical Mechanics* (Addison-Wesley, Reading, 1980).

136. D. Papousek and M. Aliev, *Molecular Vibrational-Rotational Spectra* (Elsevier, Amsterdam, 1982).

137. M. Diem, *Introduction to Modern Vibrational Spectroscopy* (Wiley, New York, 1993).

138. D. Bishop, *Group Theory and Chemistry* (Dover, New York, 1993).

139. J.H. Hahn, R. Zenobi, J.F. Bada and R.N. Zare, Science **239**, 1523 (1988).

140. F. Mullie and J. Reisse, Top. Curr. Chem. **139**, 83 (1987).

141. S. Clemett, C. Maechling, R.N. Zare, P. Swan and R. Walker, Science **262**, 721 (1993).

142. L.P. Allamandola, A. Tielens and J.R. Barker, Astrophys. J. Lett. **390**, 25 (1985).

143. A. Leger and J. Puget, Astr. Astrophys. **137**, 5 (1984).

144. J. Puget and A. Leger, Annu. Rev. Astron. Astrophys. **27**, 161 (1989).

145. L.J. Allamandola, A. Tielens and J.R. Barker, Astrophys. J. Suppl. **71**, 733 (1989).

146. W. Duley and D. Williams, Mon. Notices R. Astro. Soc. **196**, 269 (1981).

147. A. Sakata, S. Wada, T. Tanabe and T. Onaka, Astrophys. J. Lett. **287**, 51 (1984).

148. A. Sakata, S. Wada, T. Onaka and A.T. Tokunaga, Astrophys. J. Lett. **320**, 63 (1987).

149. A. Borghesi, E. Bussoletti and L. Colangeli, Astrophys. J. **314**, 422 (1987).

150. A. Blanco, E. Bussoletti and L. Colangeli, Astrophys. J. **334**, 875 (1988).

151. W.A. Schutte, A. Tielens and L.J. Allamandola, Astrophys. J. **415**, 397 (1993).

152. C. Moutou, A. Leger and L. d'Hendecourt, Astron. Astrophys. **310**, 297 (1996).

153. J.P. Bernard, L. d'Hendecourt and A. Leger, Astron. Astrophys. **220**, 245 (1989).

154. A. Blanco, S. Fonti and V. Orofino, Astrophys. J. **364**, 152 (1990).

155. A. Leger, L. d'Hendecourt and D. Defourneau, Astron. Astrophys. **216**, 148 (1989).

156. G. Flinckinger and T. Wdowiak, Astrophys. J. Lett. **362**, 71 (1990).

157. L. Colangeli, V. Mennella and E. Bussoletti, Astrophys. J. **385**, 577 (1992).

158. R. Clark and R. Hester, *Spectroscopy of Matrix Isolated Species* (Wiley, New York, 1989).

159. J. Shan, M. Suto and L.C. Lee, Astrophys. J. **383**, 459 (1991).

160. J. Brenner and J. Barker, Astrophys. J. Lett. **388**, 39 (1992).

161. S. Schlemmer, D. Cook, J. Harrison, B. Wurfel, W. Chapman and R. Saykally, Science **265**, 1686 (1994).

162. D. Cook, S. Schlemmer, N. Balucani and R. Saykally, Nature **380**, 227 (1996).

163. J. Kurtz, Astron. Astrophys. Lett. **255**, 1 (1992).

164. C. Joblin, L. d'Hendecourt, A. Leger and D. Defourneau, Astron. Astrophys. **281**, 923 (1995).

165. C. Joblin, P. Boissel, A. Leger, L. d'Hendecourt and D. Defourneau, Astron. Astrophys. **299**, 835 (1995).

166. P. Bernath, Chem. Soc. Rev. **25**, 111 (1996).

167. P. Bernath, in *Lecture Notes in Physics, vol. 407*, edited by P. Smith and W. Wiese (Springer-Verlag, Berlin, 1992).

Appendix A

BF Line Positions

Table A.1: Observed line positions of ^{11}BF and ^{10}BF in cm^{-1}.

J′	J″	Observed	O-C†	Δ‡	J′	J″	Observed	O-C†	Δ‡
^{11}BF									
$v = 1 \leftarrow 0$ band									
61	62	1127.1319	-01	02	60	61	1132.1236	04	02
59	60	1137.0882	81	05	58	59	1142.0243	-02	02
57	58	1146.9338	-04	02	56	57	1151.8171	06	05
55	56	1156.6714	04	02	54	55	1161.4972	-03	02
53	54	1166.2960	-01	02	52	53	1171.0662	-02	02
51	52	1175.8083	00	02	50	51	1180.5218	03	02
49	50	1185.2057	-01	02	48	49	1189.8618	05	05
47	48	1194.4876	01	02	46	47	1199.0844	02	02
45	46	1203.6515	00	02	44	45	1208.1892	02	02
43	44	1212.6967	01	02	42	43	1217.1738	-02	02
40	41	1226.0380	-00	02	39	40	1230.4239	-01	02

† Observed minus calculated in units of 10^{-4} cm^{-1}.

‡ Uncertainty in line positions in units of 10^{-4} cm^{-1}.

Table A.1: *(Continued)* Observed line positions of ^{11}BF and ^{10}BF in cm^{-1}.

J′	J″	Observed	O-C†	Δ‡	J′	J″	Observed	O-C†	Δ‡
38	39	1234.7794	00	02	37	38	1239.1038	01	02
36	37	1243.3965	-01	02	35	36	1247.6584	-00	02
34	35	1251.8885	-00	02	33	34	1256.0868	-01	02
32	33	1260.2534	-00	02	31	32	1264.3878	-00	02
30	31	1268.4898	-01	02	29	30	1272.5598	01	02
28	29	1276.5967	-00	02	27	28	1280.6011	01	02
26	27	1284.5721	-01	02	25	26	1288.5101	-01	02
24	25	1292.4151	-00	02	23	24	1296.2865	01	02
22	23	1300.1238	-01	02	21	22	1303.9275	-01	02
20	21	1307.6972	-01	02	19	20	1311.4326	-01	02
18	19	1315.1336	-00	02	17	18	1318.8002	00	02
16	17	1322.4317	-02	02	15	16	1326.0286	-00	02
14	15	1329.5903	-00	02	13	14	1333.1171	03	02
12	13	1336.6078	00	02	11	12	1340.0632	01	02
10	11	1343.4829	03	02	9	10	1346.8658	-03	08
8	9	1350.2129	-07	08	7	8	1353.5244	-03	08
6	7	1356.7993	-00	08	5	6	1360.0381	07	08
4	5	1363.2379	-06	08	3	4	1366.4025	-02	08
2	3	1369.5289	-08	08	1	2	1372.6214	21	08
1	0	1381.6645	20	08	2	1	1384.6041	30	30
3	2	1387.5009	-05	08	4	3	1390.3637	02	08
5	4	1393.1875	06	08	6	5	1395.9718	01	08
7	6	1398.7173	-02	08	8	7	1401.4250	06	08
9	8	1404.0926	05	08	10	9	1406.7201	-02	08
12	11	1411.8595	14	08	13	12	1414.3672	00	08
14	13	1416.8358	-04	08	16	15	1421.6545	07	08
18	17	1426.3052	-38	30	19	18	1428.5772	18	30
23	22	1437.2276	-14	08	28	27	1447.1073	03	08
$v = 2 \leftarrow 1$ band									
59	60	1116.6685	48	30	58	59	1121.5448	-14	03

† Observed minus calculated in units of 10^{-4} cm^{-1}.

‡ Uncertainty in line positions in units of 10^{-4} cm^{-1}.

Table A.1: *(Continued)* Observed line positions of ^{11}BF and ^{10}BF in cm^{-1}.

J′	J″	Observed	O-C†	Δ‡	J′	J″	Observed	O-C†	Δ‡
57	58	1126.3999	-19	30	56	57	1131.2303	00	02
55	56	1136.0317	04	03	54	55	1140.8057	09	08
53	54	1145.5503	-02	02	52	53	1150.2686	02	02
51	52	1154.9566	-14	08	50	51	1159.6189	-06	03
49	50	1164.2525	00	02	48	49	1168.8571	04	03
47	48	1173.4316	-03	02	46	47	1177.9776	-06	04
45	46	1182.4952	-01	02	44	45	1186.9828	-01	02
43	44	1191.4411	01	02	42	43	1195.8695	03	02
41	42	1200.2671	-02	02	40	41	1204.6367	13	08
39	40	1208.9730	-00	02	38	39	1213.2801	-01	02
37	38	1217.5567	01	02	36	37	1221.8022	01	02
35	36	1226.0166	01	02	34	35	1230.1998	02	02
33	34	1234.3510	-02	02	32	33	1238.4716	03	02
31	32	1242.5599	03	02	30	31	1246.6156	-01	02
29	30	1250.6400	02	02	28	29	1254.6315	00	02
27	28	1258.5903	-02	02	26	27	1262.5169	-01	02
25	26	1266.4105	-01	02	24	25	1270.2711	00	02
23	24	1274.0983	00	02	22	23	1277.8917	-02	02
21	22	1281.6522	00	02	20	21	1285.3787	01	02
19	20	1289.0709	-00	02	18	19	1292.7295	02	02
17	18	1296.3531	-01	02	16	17	1299.9426	-00	02
15	16	1303.4974	-01	02	14	15	1307.0177	02	02
13	14	1310.5026	01	02	12	13	1313.9524	01	02
11	12	1317.3657	-09	08	10	11	1320.7456	00	02
9	10	1324.0887	00	02	8	9	1327.3961	01	02
7	8	1330.6672	00	02	6	7	1333.9020	-01	02
5	6	1337.1005	-02	02	4	5	1340.2621	-06	03
3	4	1343.3869	-11	08	1	0	1358.4609	36	30
3	2	1364.2217	-00	02	4	3	1367.0473	03	02
6	5	1372.5836	12	08	7	6	1375.2911	-11	08
8	7	1377.9629	-03	03	9	8	1380.5956	02	02
10	9	1383.1897	13	08	11	10	1385.7421	00	02
12	11	1388.2560	-04	03	13	12	1390.7315	04	02

† Observed minus calculated in units of 10^{-4} cm^{-1}.

‡ Uncertainty in line positions in units of 10^{-4} cm^{-1}.

Table A.1: *(Continued)* Observed line positions of ^{11}BF and ^{10}BF in cm^{-1}.

J′	J″	Observed	O-C†	Δ‡	J′	J″	Observed	O-C†	Δ‡
14	13	1393.1666	06	03	15	14	1395.5604	-05	02
16	15	1397.9168	10	08	17	16	1400.2301	-02	02
18	17	1402.5042	-02	02	19	18	1404.7379	-01	02
20	19	1406.9300	-07	03	21	20	1409.0829	02	02
22	21	1411.1927	-07	03	23	22	1413.2627	-02	02
25	24	1417.2775	-01	02	27	26	1421.1253	00	02
28	27	1422.9870	08	03					
$v = 3 \leftarrow 2$ band									
55	56	1115.7269	21	08	54	55	1120.4446	-03	03
53	54	1125.1369	-06	08	52	53	1129.8037	10	05
51	52	1134.4394	-05	03	50	51	1139.0503	10	05
49	50	1143.6302	-01	02	48	49	1148.1834	03	02
47	48	1152.7072	-00	02	46	47	1157.2045	18	30
45	46	1161.6686	-04	02	44	45	1166.1061	-03	02
43	44	1170.5148	03	02	42	43	1174.8931	01	02
41	42	1179.2420	01	02	40	41	1183.5608	00	02
39	40	1187.8497	-00	02	38	39	1192.1075	-08	03
37	38	1196.3368	02	02	36	37	1200.5344	02	02
35	36	1204.7009	-00	02	34	35	1208.8372	04	02
33	34	1212.9409	-06	03	32	33	1217.0145	-02	02
31	32	1221.0564	-01	02	30	31	1225.0669	02	02
29	30	1229.0447	-01	02	28	29	1232.9907	-02	02
27	28	1236.9048	-00	02	26	27	1240.7865	02	02
25	26	1244.6352	01	02	24	25	1248.4508	-02	02
23	24	1252.2341	-00	02	22	23	1255.9842	02	02
21	22	1259.7004	-02	02	20	21	1263.3834	-02	02
19	20	1267.0332	01	02	18	19	1270.6484	-00	02
17	18	1274.2300	00	02	16	17	1277.7772	00	02
15	16	1281.2905	03	02	14	15	1284.7684	00	02
13	14	1288.2120	01	02	12	13	1291.6206	-00	02

† Observed minus calculated in units of 10^{-4} cm^{-1}.
‡ Uncertainty in line positions in units of 10^{-4} cm^{-1}.

Table A.1: *(Continued)* Observed line positions of ^{11}BF and ^{10}BF in cm^{-1}.

J′	J″	Observed	O-C†	Δ‡	J′	J″	Observed	O-C†	Δ‡
11	12	1294.9937	-04	02	10	11	1298.3328	03	02
9	10	1301.6348	-04	02	8	9	1304.9021	-03	02
7	8	1308.1334	-06	03	6	7	1311.3282	-12	08
5	6	1314.4884	-04	02	4	5	1317.6104	-14	08
3	4	1320.6980	-04	03	2	3	1323.7488	03	02
0	1	1329.7397	20	08	1	0	1335.5790	06	03
3	2	1341.2694	04	02	4	3	1344.0611	34	30
7	6	1352.1952	02	02	8	7	1354.8296	-10	08
9	8	1357.4263	-13	08	10	9	1359.9891	32	30
11	10	1362.5050	00	02	12	11	1364.9857	06	03
13	12	1367.4260	02	02	14	13	1369.8294	25	30
15	14	1372.1884	00	02	16	15	1374.5097	-03	02
17	16	1376.7921	03	02	18	17	1379.0326	-06	03
19	18	1381.2345	-00	02	20	19	1383.3949	-04	02
21	20	1385.5145	-08	05	22	21	1387.5949	01	02
23	22	1389.6333	01	02	24	23	1391.6323	18	30
25	24	1393.5864	00	02	26	25	1395.4990	-19	30
27	26	1397.3730	-08	08	29	28	1400.9954	09	05
30	29	1402.7438	21	30	31	30	1404.4479	12	05
34	33	1409.3086	17	08	36	35	1412.3334	04	10
$v = 4 \leftarrow 3$ band									
50	51	1118.8200	-07	08	49	50	1123.3496	05	08
48	49	1127.8473	-19	10	47	48	1132.3251	36	30
46	47	1136.7668	15	08	45	46	1141.1806	01	02
44	45	1145.5665	-03	03	43	44	1149.9251	06	03
42	43	1154.2523	-05	04	41	42	1158.5524	05	03
40	41	1162.8207	-07	03	39	40	1167.0608	-03	02
38	39	1171.2717	07	03	37	38	1175.4501	-06	03
36	37	1179.5995	-08	05	35	36	1183.7193	00	02
34	35	1187.8073	-02	02	33	34	1191.8655	04	02

† Observed minus calculated in units of 10^{-4} cm^{-1}.

‡ Uncertainty in line positions in units of 10^{-4} cm^{-1}.

Table A.1: *(Continued)* Observed line positions of ^{11}BF and ^{10}BF in cm^{-1}.

J′	J″	Observed	O-C†	Δ‡	J′	J″	Observed	O-C†	Δ‡
32	33	1195.8919	03	02	31	32	1199.8858	-09	05
30	31	1203.8510	04	02	29	30	1207.7833	05	03
28	29	1211.6834	02	02	26	27	1219.3880	-00	02
25	26	1223.1922	02	02	24	25	1226.9628	-07	03
23	24	1230.7019	-03	02	22	23	1234.4077	-06	02
21	22	1238.0800	-11	04	20	21	1241.7209	00	02
19	20	1245.3278	06	03	18	19	1248.8990	-09	05
17	18	1252.4393	04	02	16	17	1255.9436	-03	02
15	16	1259.4141	-06	03	14	15	1262.8520	04	02
13	14	1266.2543	06	03	12	13	1269.6212	-00	02
11	12	1272.9537	-02	02	10	11	1276.2520	01	02
9	10	1279.5145	00	02	8	9	1282.7424	06	03
7	8	1285.9343	07	03	6	7	1289.0894	-02	02
4	5	1295.2945	01	02	3	4	1298.3463	39	30
2	1	1315.8559	-56	30	3	2	1318.6514	-02	02
4	3	1321.4056	14	08	5	4	1324.1167	-22	30
6	5	1326.7939	-19	30	7	6	1329.4343	-04	02
8	7	1332.0355	00	02	9	8	1334.5996	18	30
10	9	1337.1221	05	03	11	10	1339.6066	00	02
12	11	1342.0528	-00	02	13	12	1344.4591	-08	03
14	13	1346.8285	05	03	15	14	1349.1569	03	02
17	16	1353.6961	11	08	18	17	1355.9036	-08	03
19	18	1358.0738	-02	02	21	20	1362.2922	-01	02
22	21	1364.3406	-02	02	23	22	1366.3495	07	03
24	23	1368.3139	-18	30	25	24	1370.2419	00	02
26	25	1372.1278	09	05	27	26	1373.9714	08	03
28	27	1375.7716	-12	05	31	30	1380.9300	06	03
32	31	1382.5643	-00	02	33	32	1384.1575	03	03
34	33	1385.7070	-05	02	35	34	1387.2131	-23	10
36	35	1388.6796	-10	05					

$v = 5 \leftarrow 4$ band

† Observed minus calculated in units of 10^{-4} cm^{-1}.

‡ Uncertainty in line positions in units of 10^{-4} cm^{-1}.

Table A.1: *(Continued)* Observed line positions of ^{11}BF and ^{10}BF in cm^{-1}.

J′	J″	Observed	O-C†	Δ‡	J′	J″	Observed	O-C†	Δ‡
44	45	1125.3707	-10	10	42	43	1133.9564	-00	02
40	41	1142.4262	10	05	39	40	1146.6174	17	10
38	39	1150.7797	32	20	34	35	1167.1199	-02	02
32	33	1175.1087	-09	08	31	32	1179.0580	-01	02
28	29	1190.7149	-11	08	27	28	1194.5383	-06	05
25	26	1202.0895	03	02	24	25	1205.8160	-00	02
23	24	1209.5069	-36	20	22	23	1213.1718	-06	05
21	22	1216.8016	00	02	20	21	1220.3980	00	02
19	20	1223.9621	09	05	18	19	1227.4907	-02	02
17	18	1230.9874	00	02	16	17	1234.4526	24	10
15	16	1237.8777	-15	08	14	15	1241.2741	-01	02
13	14	1244.6352	00	02	12	13	1247.9596	-20	08
11	12	1251.2549	11	10	10	11	1254.5122	11	10
9	10	1257.7346	09	10	7	8	1264.0744	09	10
6	7	1267.1929	24	30	3	4	1276.3210	-63	30
4	3	1299.0780	-60	60	6	5	1304.4171	19	30
8	7	1309.5860	06	10	9	8	1312.1119	-15	08
10	9	1314.6055	22	30	11	10	1317.0555	07	10
12	11	1319.4685	09	10	13	12	1321.8442	23	30
14	13	1324.1824	53	30	15	14	1326.4695	-37	30
16	15	1328.7329	25	30	17	16	1330.9452	-27	30
26	25	1349.1068	-18	30	27	26	1350.9257	18	10
30	29	1356.1223	02	02					

† Observed minus calculated in units of 10^{-4} cm^{-1}.

‡ Uncertainty in line positions in units of 10^{-4} cm^{-1}.

Table A.1: *(Continued)* Observed line positions of ^{11}BF and ^{10}BF in cm^{-1}.

J′	J″	Observed	O-C†	Δ‡	J′	J″	Observed	O-C†	Δ‡
^{10}BF									
$v = 1 \leftarrow 0$ band									
52	53	1198.6323	02	03	50	51	1208.7774	03	03
49	50	1213.8035	08	05	48	49	1218.7951	-17	08
47	48	1223.7589	-05	02	46	47	1228.6883	-18	08
45	46	1233.5891	04	05	44	45	1238.4555	05	05
43	44	1243.2887	-00	02	42	43	1248.0898	00	02
41	42	1252.8574	-04	03	40	41	1257.5939	10	05
39	40	1262.2938	-07	05	38	39	1266.9630	02	05
37	38	1271.5983	12	05	36	37	1276.1981	05	05
35	36	1280.7636	-02	05	34	35	1285.2957	-01	05
33	34	1289.7932	00	05	32	33	1294.2554	-04	05
31	32	1298.6837	01	02	30	31	1303.0765	04	03
29	30	1307.4331	-00	02	28	29	1311.7551	03	02
27	28	1316.0408	01	02	26	27	1320.2898	-06	03
25	26	1324.5038	-03	03	24	25	1328.6815	00	05
23	24	1332.8218	-03	03	22	23	1336.9257	-03	03
21	22	1340.9941	10	08	20	21	1345.0233	04	05
19	20	1349.0137	-15	08	18	19	1352.9702	00	05
17	18	1356.8858	-14	08	16	17	1360.7682	18	20
15	16	1364.6074	00	05	14	15	1368.4104	03	08
13	14	1372.1727	-12	30	11	12	1379.5902	45	20
10	11	1383.2330	01	30					
$v = 2 \leftarrow 1$ band									
43	44	1220.7806	-11	08	41	42	1230.2428	02	02
40	41	1234.9239	-00	02	39	40	1239.5761	39	30
38	39	1244.1872	-01	02	37	38	1248.7684	-05	05

† Observed minus calculated in units of 10^{-4} cm^{-1}.
‡ Uncertainty in line positions in units of 10^{-4} cm^{-1}.

Table A.1: *(Continued)* Observed line positions of ^{11}BF and ^{10}BF in cm^{-1}.

J′	J″	Observed	O-C†	Δ‡	J′	J″	Observed	O-C†	Δ‡
36	37	1253.3172	01	02	35	36	1257.8305	-06	05
34	35	1262.3110	-02	05	33	34	1266.7574	03	02
32	33	1271.1693	07	05	31	32	1275.5451	-01	05
30	31	1279.8863	-08	05	29	30	1284.1934	-05	05
28	29	1288.4655	-00	02	27	28	1292.7011	-05	05
26	27	1296.9021	00	02	25	26	1301.0662	-04	02
24	25	1305.1959	08	05	23	24	1309.2864	-08	05
22	23	1313.3433	03	02	21	22	1317.3657	36	30
20	21	1321.3444	02	05	19	20	1325.2901	08	05
18	19	1329.1974	02	05	17	18	1333.0678	04	05
16	17	1336.8978	-22	30	15	16	1340.6937	-11	05
14	15	1344.4591	75	50	13	14	1348.1706	05	08
12	13	1351.8513	12	10	11	12	1355.4917	02	10
10	11	1359.0936	-02	10	9	10	1362.6569	-03	10
7	8	1369.6651	-11	08					
$v = 3 \leftarrow 2$ band									
37	38	1226.2873	-02	50	35	36	1235.2548	00	10
34	35	1239.6855	25	20	33	34	1244.0784	13	20
31	32	1252.7639	10	10	30	31	1257.0541	01	05
29	30	1261.3097	-06	05	28	29	1265.5325	07	05
27	28	1269.7182	01	02	26	27	1273.8683	-06	03
24	25	1282.0623	-15	08	23	24	1286.1059	-15	08
22	23	1290.1149	00	02	21	22	1294.0868	08	08
20	21	1298.0203	-00	02	19	20	1301.9172	-08	08
18	19	1305.7790	02	02	17	18	1309.6038	14	08
16	17	1313.3902	15	08	15	16	1317.1370	-02	05
14	15	1320.8494	12	08	13	14	1324.5205	-05	08
10	11	1335.3099	-03	02	8	9	1342.3097	01	02

† Observed minus calculated in units of 10^{-4} cm^{-1}.

‡ Uncertainty in line positions in units of 10^{-4} cm^{-1}.

Appendix B

MgF Line Positions

Table B.1: Observed line positions of MgF in cm^{-1}.

N′	N″	Observed	O-C†	N′	N″	Observed	O-C†	N′	N″	Observed	O-C†
$v = 1 \leftarrow 0$ band											
1	0	712.7026	46	3	2	714.7223	36	4	3	715.7179	30
5	4	716.7029	12	6	5	717.6842	53	7	6	718 6459	-07
8	7	719.6108	60	10	9	721.4958	33	11	10	722.4207	-11
12	11	723.3424	07	13	12	724.2495	-22	14	13	725.1544	22
15	14	726.0457	28	16	15	726.9259	21	17	16	727.7993	43
18	17	728.6567	03	19	18	729.5063	-16	20	19	730.3527	30
21	20	731.1817	02	22	21	732.0040	05	23	22	732.8165	10
24	23	733.6155	-21	28	27	736.7284	22	29	28	737.4789	07
30	29	738.2241	38	31	30	738.9509	-11	32	31	739.6747	09
33	32	740.3840	-13	34	33	741.0868	00	35	34	741.7769	-11
36	35	742.4573	-16	37	36	743.1296	-01	38	37	743.7908	05
39	38	744.4395	-08	40	39	745.0798	-04	41	40	745.7113	15
42	41	746.3297	07	43	42	746.9378	00	44	43	747.5358	-02
45	44	748.1246	05	46	45	748.7014	-01	47	46	749.2690	04
48	47	749.8256	05	49	48	750.3702	-09	50	49	750.9050	-15

† Observed minus calculated in units of 10^{-4} cm^{-1}.

Table B.1: *(Continued)* Observed line positions of MgF in cm^{-1}.

N′	N″	Observed	O-C†	N′	N″	Observed	O-C†	N′	N″	Observed	O-C†
51	50	751.4311	-03	52	51	751.9432	-26	53	52	752.4497	01
54	53	752.9425	-01	55	54	753.4257	05	56	55	753.8949	-19
57	56	754.3573	-06	58	57	754.8075	-08	59	58	755.2471	-08
60	59	755.6767	-01	61	60	756.0950	01	62	61	756.5015	-07
63	62	756.8982	-05	64	63	757.2852	08	66	65	758.0228	-01
67	66	758.3750	-09	68	67	758.7170	-09	69	68	759.0467	-24
70	69	759.3680	-12	71	70	759.6790	06	72	71	759.9746	-18
74	73	760.5415	18	75	74	760.8018	-28	76	75	761.0588	03
78	77	761.5330	01	69	70	618.2423	-57	68	69	619.8563	-47
67	68	621.4657	-09	66	67	623.0656	07	65	66	624.6556	-00
64	65	626.2347	-42	63	64	627.8149	02	61	62	630.9421	-13
60	61	632.4965	-01	59	60	634.0425	04	58	59	635.5804	06
57	58	637.1074	-24	56	57	638.6309	-11	55	56	640.1463	-03
54	55	641.6522	-12	53	54	643.1530	06	52	53	644.6418	-16
51	52	646.1270	02	50	51	647.6011	-09	49	50	649.0756	61
48	49	650.5295	07	47	48	651.9811	08	46	47	653.4209	-26
45	46	654.8588	-01	44	45	656.2855	-06	43	44	657.7061	09
42	43	659.1151	-10	41	42	660.5196	06	40	41	661.9142	07
39	40	663.3006	07	38	39	664.6794	14	35	36	668.7682	59
34	35	670.1072	03	33	34	671.4430	-02	32	33	672.7713	02
31	32	674.0902	-03	30	31	675.4015	01	29	30	676.7024	-13
28	29	677.9954	-21	27	28	679.2832	04	26	27	680.5613	18
25	26	681.8270	-04	24	25	683.0865	-02	23	24	684.3373	-01
22	23	685.5797	04	21	22	686.8130	05	20	21	688.0374	05
19	20	689.2553	28	18	19	690.4591	-01	17	18	691.6579	08
16	17	692.8467	06	15	16	694.0278	16	14	15	695.2007	33
13	14	696.3608	13	12	13	697.5118	-09	11	12	698.6572	03
10	11	699.7912	-07	9	10	700.9190	09	8	9	702.0337	-12
6	7	704.2397	-17	5	6	705.3277	-32	4	5	706.4121	09
$v = 2 \leftarrow 1$ band											
10	9	713.0293	-03	11	10	713.9497	-08	12	11	714.8637	19

† Observed minus calculated in units of 10^{-4} cm^{-1}.

Table B.1: *(Continued)* Observed line positions of MgF in cm^{-1}.

N′	N″	Observed	O-C†	N′	N″	Observed	O-C†	N′	N″	Observed	O-C†
13	12	715.7743	09	14	13	716.6564	09	15	14	717.5373	-05
16	15	718.4098	-07	17	16	719.2744	07	18	17	720.1265	-04
19	18	720.9705	01	20	19	721.8001	-40	21	20	722.6277	-04
22	21	723.4419	-04	23	22	724.2495	28	24	23	725.0420	09
25	24	725.8263	06	26	25	726.5979	-24	27	26	727.3658	07
29	28	728.8639	-05	30	29	729.5991	-01	31	30	730.3230	-09
32	31	731.0388	01	33	32	731.7431	-01	34	33	732.4420	43
35	34	733.1253	32	36	35	733.7960	-02	40	39	736.3800	-11
41	40	737.0106	-37	42	41	737.6263	-08	43	42	738.2241	-55
44	43	738.8216	-02	45	44	739.4042	05	46	45	739.9759	07
47	46	740.5352	-09	48	47	741.0868	-00	49	48	741.6258	-12
50	49	742.1565	-02	51	50	742.6761	00	52	51	743.1784	-63
53	52	743.6834	03	54	53	744.1681	-26	55	54	744.6475	-02
56	55	745.1138	-04	57	56	745.5709	07	58	57	746.0132	-21
59	58	746.4497	-02	60	59	746.8740	01	61	60	747.2869	-01
62	61	747.6894	-01	63	62	748.0810	-02	64	63	748.4605	-17
65	64	748.8324	00	66	65	749.1920	02	67	66	749.5397	-06
68	67	749.8784	03	69	68	750.2047	-01	70	69	750.5192	-15
71	70	750.8246	-11	73	72	751.4031	01	74	73	751.6751	-01
86	87	582.4256	-05	85	86	584.1451	05	84	85	585.8577	14
83	84	587.5607	-03	81	82	590.9512	09	80	81	592.6359	13
78	79	595.9842	20	76	77	599.3013	-05	74	75	602.5949	15
73	74	604.2305	21	71	72	607.4739	-30	70	71	609.0866	-37
69	70	610.6957	-08	68	69	612.2955	-00	67	68	613.8855	-16
66	67	615.4714	-00	65	66	617.0485	02	64	65	618.6167	-11
63	64	620.1779	-18	62	63	621.7339	-04	61	62	623.2843	29
60	61	624.8187	-21	59	60	626.3526	-02	58	59	627.8804	31
57	58	629.3953	14	56	57	630.9012	-17	55	56	632.4041	-01
54	55	633.8974	-05	53	54	635.3806	-31	52	53	636.8634	14
51	52	638.3308	-14	50	51	639.7984	37	49	50	641.2498	05
48	49	642.6964	04	47	48	644.1345	-01	46	47	645.5656	01
45	46	646.9916	33	44	45	648.4023	-06	43	44	649.8102	05
42	43	651.2084	00	41	42	652.5985	-03	40	41	653.9819	06
39	40	655.3558	03	38	39	656.7206	-08	37	38	658.0817	24

† Observed minus calculated in units of 10^{-4} cm^{-1}.

Table B.1: *(Continued)* Observed line positions of MgF in cm^{-1}.

N′	N″	Observed	O-C†	N′	N″	Observed	O-C†	N′	N″	Observed	O-C†
36	37	659.4294	06	35	36	660.7694	-06	34	35	662.1042	12
33	34	663.4268	-07	32	33	664.7446	08	31	32	666.0500	-15
30	31	667.3553	43	29	30	668.6434	15	28	29	669.9243	-00
27	28	671.1986	03	26	27	672.4611	-25	25	26	673.7208	03
24	25	674.9684	-03	23	24	676.2091	07	22	23	677.4371	-22
21	22	678.6617	00	20	21	679.8762	10	19	20	681.0814	14
18	19	682.2787	26	17	18	683.4637	03	16	17	684.6432	14
15	16	685.8097	-17	14	15	686.9751	29	13	14	688.1223	-16
11	12	690.4015	06	10	11	691.5261	02	9	10	692.6432	13
8	9	693.7509	20								
$v = 3 \leftarrow 2$ band											
9	8	703.7440	10	10	9	704.6612	-34	11	10	705.5770	-00
13	12	707.3732	01	14	13	708.2588	20	15	14	709.1319	09
16	15	709.9959	03	17	16	710.8500	-04	18	17	711.6953	-04
19	18	712.5288	-25	20	19	713.3598	26	21	20	714.1746	12
22	21	714.9804	06	23	22	715.7750	-14	24	23	716.5630	-03
25	24	717.3407	03	26	25	718.1071	-04	27	26	718.8641	-07
29	28	720.3493	-05	30	29	721.0757	-17	32	31	722.5031	03
33	32	723.1999	-05	34	33	723.8880	-01	35	34	724.5661	04
36	35	725.2330	-01	37	36	725.8899	-06	38	37	726.5378	-00
39	38	727.1751	01	41	40	728.4186	-00	42	41	729.0256	03
43	42	729.6219	02	44	43	730.2064	-13	45	44	730.7829	-05
46	45	731.3490	00	47	46	731.9036	-05	49	48	732.9828	-06
50	49	733.5066	-08	56	55	736.4311	-15	57	56	736.8854	20
58	57	737.3209	-26	59	58	737.7535	03	60	59	738.1718	-03
61	60	738.5792	-13	62	61	738.9788	05	63	62	739.3654	00
64	63	739.7414	-03	65	64	740.1084	10	66	65	740.4605	-18
67	66	740.8082	17	68	67	741.1392	-06	69	68	741.4620	-05
71	70	742.0744	-09	72	71	742.3723	68	73	72	742.6449	01
74	73	742.9141	09	76	75	743.4173	02	77	76	743.6540	14
78	77	743.8801	28	80	79	744.2954	19	83	82	744.8335	-14

† Observed minus calculated in units of 10^{-4} cm^{-1}.

Table B.1: *(Continued)* Observed line positions of MgF in cm^{-1}.

N′	N″	Observed	O-C†	N′	N″	Observed	O-C†	N′	N″	Observed	O-C†
85	84	745.1423	17	86	85	745.2772	04	83	84	580.3048	-02
82	83	581.9866	-15	81	82	583.6636	-07	80	81	585.3334	-03
79	80	586.9965	01	78	79	588.6512	-08	76	77	591.9467	41
73	74	596.8184	-73	72	73	598.4451	57	70	71	601.6475	23
69	70	603.2371	-02	68	69	604.8280	58	67	68	606.3992	-06
66	67	607.9700	-02	65	66	609.5353	19	64	65	611.0925	34
63	64	612.6353	-21	62	63	614.1796	12	61	62	615.7147	02
60	61	617.2396	16	59	60	618.7557	-07	58	59	620.2722	47
57	58	621.7707	-02	56	57	623.2645	-23	55	56	624.7555	04
53	54	627.7097	12	52	53	629.1748	11	51	52	630.6317	06
50	51	632.0787	-20	48	49	634.9564	-02	47	48	636.3824	-03
46	47	637.8004	-06	45	46	639.2114	00	44	45	640.6109	-27
43	44	642.0066	-15	42	43	643.3952	06	41	42	644.7726	-02
40	41	646.1438	06	39	40	647.5100	48	38	39	648.8579	-13
37	38	650.2049	-02	36	37	651.5366	-62	35	36	652.8721	-01
34	35	654.1940	04	33	34	655.5066	01	32	33	656.8113	01
31	32	658.1057	-17	30	31	659.3963	09	29	30	660.6757	07
28	29	661.9459	-02	27	28	663.2084	-04	26	27	664.4631	-00
25	26	665.7091	03	24	25	666.9444	-15	23	24	668.1746	-00
22	23	669.3928	-19	21	22	670.6038	-23	20	21	671.8067	-22
19	20	673.0040	08	18	19	674.1835	-51	17	18	675.3607	-46
16	17	676.5346	12	15	16	677.6955	30	14	15	678.8418	-11
13	14	679.9873	28	12	13	681.1157	-15	11	12	682.2387	-23
10	11	683.3586	26	9	10	684.4626	06				
$v = 4 \leftarrow 3$ band											
1	0	687.8405	-09	3	2	689.8041	-33	5	4	691.7315	-50
6	5	692.6919	46	7	6	693.6262	-22	8	7	694.5615	09
9	8	695.4835	03	10	9	696.3967	02	12	11	698.1961	13
13	12	699.0799	02	14	13	699.9536	-15	15	14	700.8189	-22
17	16	702.5245	-00	18	17	703.3592	-26	19	18	704.1907	11
20	19	705.0075	-01	21	20	705.8162	01	22	21	706.6131	-17

† Observed minus calculated in units of 10^{-4} cm^{-1}.

Table B.1: *(Continued)* Observed line positions of MgF in cm^{-1}.

N′	N″	Observed	O-C†	N′	N″	Observed	O-C†	N′	N″	Observed	O-C†
23	22	707.4032	-07	24	23	708.1855	21	25	24	708.9527	-02
26	25	709.7101	-26	27	26	710.4635	07	28	27	711.2015	-14
29	28	711.9333	-00	30	29	712.6554	15	32	31	714.0651	-01
33	32	714.7561	00	34	33	715.4374	04	35	34	716.1079	02
36	35	716.7694	07	37	36	717.4201	07	38	37	718.0586	-16
39	38	718.6904	-05	40	39	719.3096	-19	41	40	719.9221	00
42	41	720.5237	12	43	42	721.1116	-10	44	43	721.6910	-17
45	44	722.2622	-02	46	45	722.8227	06	48	47	723.9127	21
49	48	724.4392	-02	50	49	724.9579	00	52	51	725.9642	03
53	52	726.4537	25	55	54	727.3939	-09	56	55	727.8524	14
58	57	728.7325	06	59	58	729.1565	-00	60	59	729.5734	26
61	60	729.9757	13	63	62	730.7492	-07	64	63	731.1225	07
65	64	731.4777	-52	66	65	731.8349	13	78	79	581.4105	-17
77	78	583.0458	-06	76	77	584.6652	-85	74	75	587.9073	-01
73	74	589.5139	-00	72	73	591.1156	22	69	70	595.8755	64
68	69	597.4375	-25	67	68	598.9951	-87	66	67	600.5595	-09
65	66	602.1080	-18	63	64	605.1870	03	62	63	606.7151	10
61	62	608.2356	15	60	61	609.7425	-42	59	60	611.2513	-06
58	59	612.7505	08	57	58	614.2386	-13	55	56	617.1978	-00
54	55	618.6663	09	53	54	620.1262	09	52	53	621.5770	-06
51	52	623.0270	47	50	51	624.4591	-01	49	50	625.8877	-07
47	48	628.7233	-01	46	47	630.1306	12	45	46	631.5291	18
44	45	632.9176	03	43	44	634.3028	33	42	43	635.6739	02
41	42	637.0419	19	40	41	638.3983	01	39	40	639.7546	62
38	39	641.0924	20	37	38	642.4270	25	36	37	643.7588	84
35	36	645.0693	11	34	35	646.3776	-01	33	34	647.6784	-07
32	33	648.9716	-06	31	32	650.2585	13	29	30	652.8032	11
28	29	654.0628	09	27	28	655.3139	04	26	27	656.5584	18
25	26	657.7887	-25	24	25	659.0191	15	23	24	660.2364	10
22	23	661.4429	-16	21	22	662.6464	11	20	21	663.8390	16
19	20	665.0220	10	18	19	666.2010	51	15	16	669.6684	-01
14	15	670.8065	-22	13	14	671.9408	07	12	13	673.0607	-20
9	10	676.3753	-21	7	8	678.5425	-03	5	6	680.6787	61
3	4	682.7635	-26	0	1	685.8359	-28				

† Observed minus calculated in units of 10^{-4} cm^{-1}.

Table B.1: *(Continued)* Observed line positions of MgF in cm^{-1}.

N′	N″	Observed	O-C†	N′	N″	Observed	O-C†	N′	N″	Observed	O-C†
$v = 5 \leftarrow 4$ band											
6	5	684.5469	-19	8	7	686.4060	10	9	8	687.3247	56
10	9	688.2270	30	11	10	689.1191	-03	12	11	690.0047	-08
14	13	691.7521	25	15	14	692.5991	-83	16	15	693.4565	06
17	16	694.2950	01	18	17	695.1237	-05	20	19	696.7554	09
22	21	698.3504	38	23	22	699.1287	06	24	23	699.8971	-28
25	24	700.6558	-64	26	25	701.4077	-70	27	26	702.1573	-02
28	27	702.8904	-02	29	28	703.6145	06	31	30	705.0304	-06
32	31	705.7224	-26	34	33	707.0828	-03	35	34	707.7454	-19
36	35	708.4024	07	37	36	709.0447	-12	38	37	709.6797	-06
39	38	710.3020	-27	40	39	710.9177	-12	41	40	711.5213	-20
42	41	712.1158	-17	44	43	713.2740	-18	45	44	713.8369	-28
46	45	714.3935	-00	47	46	714.9372	00	48	47	715.4706	00
49	48	715.9917	-20	50	49	716.5057	-10	51	50	717.0092	-02
52	51	717.5011	-07	53	52	717.9843	03	54	53	718.4544	-13
55	54	718.9212	39	56	55	719.3628	-55	57	56	719.8055	-35
58	57	720.2386	-07	59	58	720.6593	01	62	61	721.8552	-08
63	62	722.2343	03	64	63	722.6038	24	65	64	722.9607	24
66	65	723.3058	13	67	66	723.6429	26	68	67	723.9747	93
74	75	580.6992	-04	73	74	582.2912	-06	72	73	583.8757	-14
71	72	585.4540	-14	70	71	587.0270	03	69	70	588.5903	-05
68	69	590.1419	-61	65	66	594.7785	19	64	65	596.3041	-09
63	64	597.8273	10	62	63	599.3357	-44	61	62	600.8510	41
60	61	602.3491	29	59	60	603.8377	-04	58	59	605.3245	18
57	58	606.8049	50	56	57	608.2759	64	54	55	611.1925	61
52	53	614.0758	28	51	52	615.5048	-00	50	51	616.9300	08
49	50	618.3441	-17	48	49	619.7556	08	47	48	621.1586	26
46	47	622.5475	-18	45	46	623.9342	-07	44	45	625.3150	22
43	44	626.6897	69	42	43	628.0455	06	40	41	630.7429	-23
39	40	632.0845	09	38	39	633.4107	-31	37	38	634.7366	05
36	37	636.0536	32	35	36	637.3569	04	34	35	638.6540	-04

† Observed minus calculated in units of 10^{-4} cm^{-1}.

Table B.1: *(Continued)* Observed line positions of MgF in cm^{-1}.

N′	N″	Observed	O-C†	N′	N″	Observed	O-C†	N′	N″	Observed	O-C†
33	34	639.9460	16	32	33	641.2268	07	31	32	642.4995	-01
29	30	645.0229	09	28	29	646.2708	01	27	28	647.5050	-61
26	27	648.7424	-09	25	26	649.9680	09	24	25	651.1825	00
23	24	652.3905	11	22	23	653.5869	-09	21	22	654.7801	21
20	21	655.9607	12	19	20	657.1328	04	18	19	658.2963	-05
16	17	660.6013	13	15	16	661.7370	-15	14	15	662.8697	12
12	13	665.1027	03								
$v = 6 \leftarrow 5$ band											
16	15	685.3322	29	17	16	686.1582	-21	20	19	688.5968	-00
21	20	689.3934	33	22	21	690.1711	-26	23	22	690.9468	-10
26	25	693.2079	-47	27	26	693.9499	16	28	27	694.6795	52
29	28	695.3912	07	30	29	696.0962	-08	31	30	696.7919	-20
32	31	697.4822	12	33	32	698.1597	14	34	33	698.8234	-23
35	34	699.4799	-35	36	35	700.1296	-16	37	36	700.7682	-08
39	38	702.0157	04	40	39	702.6217	-16	42	41	703.8093	-04
43	42	704.3895	15	44	43	704.9568	07	45	44	705.5132	-09
46	45	706.0618	-04	49	48	707.6474	17	51	50	708.6497	-08
68	69	582.9438	-12	67	68	584.4828	14	66	67	586.0107	01
65	66	587.5316	-10	64	65	589.0442	-33	63	64	590.5587	33
60	61	595.0274	-79	58	59	597.9884	29	57	58	599.4413	-83
56	57	600.8968	-95	54	55	603.7967	-07	53	54	605.2286	-31
52	53	606.6566	-19	51	52	608.0792	13	50	51	609.4920	24
49	50	610.8917	-19	47	48	613.6761	-28	45	46	616.4296	-38
44	45	617.8011	19	43	44	619.1599	29	42	43	620.5138	67
41	42	621.8485	-07	40	41	623.1854	18	39	40	624.5086	-13
37	38	627.1400	08	36	37	628.4462	45	35	36	629.7359	-03
34	35	631.0244	16	32	33	633.5717	00	31	32	634.8361	22
30	31	636.0897	17	28	29	638.5722	07	26	27	641.0236	14
25	26	642.2374	23	24	25	643.4387	-07	22	23	645.8311	75
20	21	648.1741	01	19	20	649.3363	-02	16	17	652.7732	01
15	16	653.9010	-04	14	15	655.0115	-97	13	14	656.1248	-76

† Observed minus calculated in units of 10^{-4} cm^{-1}.

Table B.1: *(Continued)* Observed line positions of MgF in cm^{-1}.

N′	N″	Observed	O-C†	N′	N″	Observed	O-C†	N′	N″	Observed	O-C†
11	12	658.3297	09	9	10	660.4880	-24	8	9	661.5592	10
3	4	666.7640	-02								
$v = 7 \leftarrow 6$ band											
11	10	673.0389	-20	14	13	675.6197	-26	15	14	676.4693	50
16	15	677.2982	13	17	16	678.1131	-69	18	17	678.9294	-46
20	19	680.5342	05	22	21	682.0955	-00	23	22	682.8607	-15
29	28	687.2610	-12	30	29	687.9619	-00	32	31	689.3374	50
34	33	690.6639	01	35	34	691.3152	02	37	36	692.5890	11
39	38	693.8198	-17	42	41	695.6026	46	44	43	696.7349	23
46	45	697.8246	-25	48	47	698.8829	10	50	49	699.8971	08
51	52	600.7378	-23	50	51	602.1395	01	49	50	603.5309	-01
48	49	604.9164	12	47	48	606.2948	31	46	47	607.6653	47
45	46	609.0162	-54	43	44	611.7246	35	42	43	613.0583	-08
41	42	614.3975	79	39	40	617.0263	-04	37	38	619.6345	20
36	37	620.9274	39	30	31	628.5048	30	24	25	635.7871	-08
23	24	636.9773	39	22	23	638.1512	05	21	22	639.3189	-06
20	21	640.4796	-04	19	20	641.6313	-09	17	18	643.9050	-61
13	14	648.3625	-47	12	13	649.4670	71	7	8	654.7945	12
5	6	656.8656	-00	2	3	659.9051	-32				

† Observed minus calculated in units of 10^{-4} cm^{-1}.

Appendix C

BrCNO Line Positions

Table C.1: Observed line positions of ^{79}BrCNO in cm^{-1}.

J′	J″	Observed	O-C†	Δ‡	J′	J″	Observed	O-C†	Δ‡
ν_1 band									
59	60	2209.2211	-1	5	58	59	2209.3334	38	20
57	58	2209.4402	18	10	56	57	2209.5479	6	5
55	56	2209.6551	-12	5	54	55	2209.7632	-23	10
53	54	2209.8739	-9	5	52	53	2209.9827	-16	10
51	52	2210.0927	-13	5	50	51	2210.2041	4	5
49	50	2210.3134	-3	5	48	49	2210.4232	-6	5
47	48	2210.5332	-8	5	46	47	2210.6440	-4	5
45	46	2210.7547	-3	5	44	45	2210.8661	4	5
43	44	2210.9761	-4	5	42	43	2211.0871	-4	5
41	42	2211.1982	-4	5	40	41	2211.3090	-8	5
39	40	2211.4208	-5	5	38	39	2211.5332	3	5
37	38	2211.6449	3	5	36	37	2211.7558	-6	5
35	36	2211.8683	-1	5	34	35	2211.9803	-4	5

† Observed minus calculated in units of 10^{-4} cm^{-1}.
‡ Uncertainty in line positions in units of 10^{-4} cm^{-1}.

Table C.1: *(Continued)*Observed line positions of ^{79}BrCNO in cm^{-1}.

J′	J″	Observed	O-C†	Δ‡	J′	J″	Observed	O-C†	Δ‡
33	34	2212.0926	-3	5	32	33	2212.2059	5	5
31	32	2212.3192	12	5	30	31	2212.4311	4	5
29	30	2212.5440	5	5	27	28	2212.7692	-5	5
25	26	2212.9962	-4	5	24	25	2213.1106	5	5
23	24	2213.2234	-5	5	22	23	2213.3373	-4	5
21	22	2213.4517	0	5	20	21	2213.5654	-5	5
19	20	2213.6793	-9	5	18	19	2213.7947	1	5
17	18	2213.9088	-4	5	16	17	2214.0246	7	5
15	16	2214.1390	3	5	14	15	2214.2538	0	5
13	14	2214.3685	-3	5	12	13	2214.4844	3	5
11	12	2214.6010	15	10	10	11	2214.7142	-8	5
9	10	2214.8325	18	10	8	9	2214.9465	0	5
7	8	2215.0642	17	10	5	6	2215.2934	-14	5
3	4	2215.5287	11	5	1	2	2215.7596	-14	10
0	1	2215.8751	-28	10	4	3	2216.4638	-7	5
5	4	2216.5823	2	5	6	5	2216.6994	-6	5
7	6	2216.8181	2	5	8	7	2216.9365	5	5
9	8	2217.0534	-8	5	10	9	2217.1725	-1	5
11	10	2217.2908	-3	5	12	11	2217.4098	0	5
13	12	2217.5296	11	5	14	13	2217.6493	19	10
15	14	2217.7666	1	5	16	15	2217.8873	17	10
17	16	2218.0037	-11	5	18	17	2218.1241	-2	5
19	18	2218.2428	-11	5	20	19	2218.3613	-22	10
21	20	2218.4833	-1	5	23	22	2218.7223	-11	5
24	23	2218.8432	-4	5	25	24	2218.9627	-12	5
26	25	2219.0843	-1	5	27	26	2219.2051	1	5
28	27	2219.3256	-2	5	29	28	2219.4459	-7	5
30	29	2219.5676	0	5	31	30	2219.6888	1	5
32	31	2219.8107	7	5	33	32	2219.9307	-6	5
34	33	2220.0535	6	5	35	34	2220.1745	0	5
36	35	2220.2959	-4	5	37	36	2220.4171	-11	5
38	37	2220.5410	8	5	39	38	2220.6625	1	5
40	39	2220.7846	-1	5	41	40	2220.9058	-13	5

† Observed minus calculated in units of 10^{-4} cm^{-1}.

‡ Uncertainty in line positions in units of 10^{-4} cm^{-1}.

Table C.1: *(Continued)*Observed line positions of ^{79}BrCNO in cm^{-1}.

J′	J″	Observed	O-C†	Δ‡	J′	J″	Observed	O-C†	Δ‡
42	41	2221.0292	-4	5	43	42	2221.1514	-9	5
44	43	2221.2767	16	10	45	44	2221.3981	1	5
46	45	2221.5225	13	5	47	46	2221.6450	6	5
48	47	2221.7659	-18	10	49	48	2221.8920	8	5
50	49	2222.0154	7	5	51	50	2222.1391	7	5
52	51	2222.2623	0	5	53	52	2222.3854	-9	5
54	53	2222.5109	5	5	55	54	2222.6357	10	5
56	55	2222.7586	-4	5	57	56	2222.8810	-25	10
58	57	2223.0057	-25	10	59	58	2223.1362	33	20
ν_1 band									
81	82	1312.4534	3	5	80	81	1312.6012	-1	5
79	80	1312.7479	-11	5	78	79	1312.8962	-2	5
76	77	1313.1901	1	5	75	76	1313.3355	-7	5
73	74	1313.6275	0	5	72	73	1313.7727	2	5
71	72	1313.9170	-2	5	70	71	1314.0613	-2	5
69	70	1314.2057	3	5	68	69	1314.3490	0	5
67	68	1314.4925	4	5	66	67	1314.6348	-1	5
65	66	1314.7779	7	5	64	65	1314.9184	-9	5
63	64	1315.0606	-3	5	61	62	1315.3428	-2	5
60	61	1315.4833	-2	5	59	60	1315.6231	-5	5
58	59	1315.7636	3	5	57	58	1315.9034	7	5
56	57	1316.0419	4	5	55	56	1316.1818	16	10
54	55	1316.3179	-4	5	53	54	1316.4564	2	5
52	53	1316.5941	5	5	51	52	1316.7297	-9	5
50	51	1316.8673	1	5	49	50	1317.0036	1	5
48	49	1317.1409	14	5	47	48	1317.2742	-8	5
46	47	1317.4110	10	5	45	46	1317.5455	7	5
44	45	1317.6802	10	5	43	44	1317.8132	1	5
42	43	1317.9463	-5	5	41	42	1318.0790	-9	5
40	41	1318.2106	-23	10	39	40	1318.3453	0	5

† Observed minus calculated in units of 10^{-4} cm^{-1}.

‡ Uncertainty in line positions in units of 10^{-4} cm^{-1}.

Table C.1: *(Continued)*Observed line positions of ^{79}BrCNO in cm^{-1}.

J′	J″	Observed	O-C†	Δ‡	J′	J″	Observed	O-C†	Δ‡
38	39	1318.4790	17	10	37	38	1318.6090	0	5
36	37	1318.7401	-2	5	35	36	1318.8706	-6	5
34	35	1318.9997	-20	10	33	34	1319.1298	-21	10
32	33	1319.2624	7	5	31	32	1319.3917	7	5
30	31	1319.5211	11	5	29	30	1319.6473	-13	5
28	29	1319.7768	-1	5	27	28	1319.9048	1	5
26	27	1320.0313	-9	5	25	26	1320.1602	9	5
24	25	1320.2850	-9	5	23	24	1320.4098	-25	10
22	23	1320.5381	-1	5	21	22	1320.6635	-3	5
20	21	1320.7885	-4	5	19	20	1320.9142	5	5
18	19	1321.0386	6	5	17	18	1321.1624	4	5
16	17	1321.2856	-1	5	15	16	1321.4092	4	5
14	15	1321.5315	-2	5	13	14	1321.6544	2	5
12	13	1321.7762	-1	5	11	12	1321.8963	-16	10
10	11	1322.0190	-2	5	9	10	1322.1403	2	5
8	9	1322.2597	-9	5	7	8	1322.3807	0	5
6	7	1322.4990	-15	10	5	6	1322.6197	-2	5
4	5	1322.7389	1	5	0	1	1323.2070	-39	20
1	0	1323.4415	-30	20	3	2	1323.6762	-5	5
4	3	1323.7885	-36	20	5	4	1323.9053	-19	10
6	5	1324.0224	5	5	7	6	1324.1335	-27	10
8	7	1324.2483	-18	10	10	9	1324.4758	-10	5
11	10	1324.5896	1	5	12	11	1324.7022	3	5
13	12	1324.8132	-6	5	14	13	1324.9255	1	5
16	15	1325.1469	-5	5	17	16	1325.2594	17	10
18	17	1325.3685	8	5	19	18	1325.4773	0	5
20	19	1325.5852	-13	5	21	20	1325.6953	-1	5
22	21	1325.8023	-15	5	23	22	1325.9098	-20	10
24	23	1326.0208	14	10	25	24	1326.1246	-21	10
26	25	1326.2351	17	10	27	26	1326.3404	5	5
28	27	1326.4456	-4	5	29	28	1326.5507	-9	5
30	29	1326.6542	-27	10	31	30	1326.7611	-6	5
32	31	1326.8669	6	5	33	32	1326.9697	-6	5

† Observed minus calculated in units of 10^{-4} cm^{-1}.

‡ Uncertainty in line positions in units of 10^{-4} cm^{-1}.

Table C.1: *(Continued)*Observed line positions of ^{79}BrCNO in cm^{-1}.

J′	J″	Observed	O-C†	Δ‡	J′	J″	Observed	O-C†	Δ‡
34	33	1327.0748	9	5	35	34	1327.1786	14	10
36	35	1327.2809	8	5	37	36	1327.3833	7	5
38	37	1327.4852	5	5	39	38	1327.5867	4	5
40	39	1327.6879	3	5	41	40	1327.7880	-5	5
42	41	1327.8884	-5	5	43	42	1327.9872	-18	10
44	43	1328.0875	-12	5	45	44	1328.1879	-1	5
46	45	1328.2870	2	5	47	46	1328.3854	1	5
48	47	1328.4837	3	5	49	48	1328.5813	3	5
50	49	1328.6783	0	5	51	50	1328.7758	7	5
52	51	1328.8722	6	5	53	52	1328.9686	10	5
54	53	1329.0634	2	5	55	54	1329.1590	5	5
56	55	1329.2535	2	5	57	56	1329.3478	1	5
58	57	1329.4418	0	5	59	58	1329.5360	6	5
60	59	1329.6287	1	5	61	60	1329.7217	3	5
62	61	1329.8132	-6	5	63	62	1329.9047	-11	5
64	63	1329.9972	-1	5	65	64	1330.0885	0	5
66	65	1330.1779	-14	5	67	66	1330.2696	0	5
68	67	1330.3587	-8	5	69	68	1330.4491	1	5
70	69	1330.5398	17	10	71	70	1330.6269	0	5
73	72	1330.8026	-4	5	74	73	1330.8902	-2	5
75	74	1330.9763	-12	5	76	75	1331.0638	-3	5
77	76	1331.1509	6	5	78	77	1331.2361	0	5
78	77	1331.2377	15	10	79	78	1331.3219	4	5
80	79	1331.4063	-2	5	81	80	1331.4912	2	5
82	81	1331.5762	10	5	85	84	1331.8230	-21	10
86	85	1331.9068	-7	5	87	86	1331.9876	-19	10
88	87	1332.0703	-9	5	89	88	1332.1513	-11	5
90	89	1332.2327	-5	5	91	90	1332.3119	-17	10
92	91	1332.3924	-11	5	93	92	1332.4714	-15	10
94	93	1332.5520	-1	5	95	94	1332.6304	-3	5
96	95	1332.7087	-3	5	97	96	1332.7871	4	5
98	97	1332.8639	-2	5	99	98	1332.9397	-15	10
100	99	1333.0194	18	10	101	100	1333.0930	-7	5

† Observed minus calculated in units of 10^{-4} cm^{-1}.

‡ Uncertainty in line positions in units of 10^{-4} cm^{-1}.

Table C.1: *(Continued)*Observed line positions of ^{79}BrCNO in cm^{-1}.

J′	J″	Observed	O-C†	Δ‡	J′	J″	Observed	O-C†	Δ‡
102	101	1333.1699	5	5	103	102	1333.2428	-19	10
104	103	1333.3218	23	10	105	104	1333.3947	7	5
106	105	1333.4657	-22	10	107	106	1333.5421	6	5
108	107	1333.6124	-21	10	109	108	1333.6872	0	5
110	109	1333.7587	-8	5	111	110	1333.8319	6	5
112	111	1333.9048	21	10	113	112	1333.9756	20	10
114	113	1334.0463	22	10	115	114	1334.1137	-5	5

† Observed minus calculated in units of 10^{-4} cm^{-1}.

‡ Uncertainty in line positions in units of 10^{-4} cm^{-1}.

Table C.2: Observed line positions of ^{81}BrCNO in cm^{-1}.

J′	J″	Observed	O-C†	Δ‡	J′	J″	Observed	O-C†	Δ‡
ν_1 band									
60	61	2209.0886	-8	10	59	60	2209.2017	48	20
58	59	2209.3039	-7	10	57	58	2209.4148	24	10
56	57	2209.5211	7	5	55	56	2209.6280	-6	10
54	55	2209.7379	11	5	53	54	2209.8450	-3	5
52	53	2209.9538	0	5	51	52	2210.0622	-3	5
50	51	2210.1708	-5	5	49	50	2210.2800	-3	5
48	49	2210.3899	5	5	47	48	2210.4990	3	5
46	47	2210.6090	9	5	45	46	2210.7184	8	5
44	45	2210.8272	-1	5	43	44	2210.9372	1	5
42	43	2211.0466	-6	5	41	42	2211.1575	2	5
40	41	2211.2674	-2	5	39	40	2211.3772	-7	5
38	39	2211.4883	-2	5	37	38	2211.5994	2	5
36	37	2211.7098	-2	5	35	36	2211.8222	12	10
34	35	2211.9299	-22	10	33	34	2212.0413	-21	10
32	33	2212.1529	-19	10	31	32	2212.2668	4	5
30	31	2212.3783	2	5	29	30	2212.4891	-9	5
28	29	2212.6015	-4	5	27	28	2212.7145	4	5
26	27	2212.8269	5	5	25	26	2212.9386	-2	5
24	25	2213.0512	-2	5	23	24	2213.1639	-2	5
22	23	2213.2759	-11	5	21	22	2213.3905	5	5
20	21	2213.5014	-18	10	19	20	2213.6165	1	5
18	19	2213.7277	-22	10	17	18	2213.8437	2	5
16	17	2213.9577	5	5	15	16	2214.0699	-12	5
14	15	2214.1846	-5	5	13	14	2214.2981	-12	5
12	13	2214.4144	9	5	11	12	2214.5281	1	5
10	11	2214.6413	-13	5	9	10	2214.7554	-20	10
8	9	2214.8709	-14	10	6	5	2216.6139	14	5
7	6	2216.7308	12	5	8	7	2216.8472	3	5
9	8	2216.9625	-18	10	13	12	2217.4358	4	5

† Observed minus calculated in units of 10^{-4} cm^{-1}.

‡ Uncertainty in line positions in units of 10^{-4} cm^{-1}.

Table C.2: *(Continued)*Observed line positions of ^{81}BrCNO in cm^{-1}.

J′	J″	Observed	O-C†	Δ‡	J′	J″	Observed	O-C†	Δ‡
14	13	2217.5521	-14	10	15	14	2217.6733	15	10
16	15	2217.7912	10	5	17	16	2217.9087	0	5
18	17	2218.0273	-1	5	19	18	2218.1450	-12	5
21	20	2218.3831	-11	5	22	21	2218.5028	-7	5
23	22	2218.6229	2	5	24	23	2218.7412	-11	5
25	24	2218.8620	1	5	26	25	2218.9821	5	5
27	26	2219.1020	5	5	28	27	2219.2209	-6	5
29	28	2219.3415	-2	5	30	29	2219.4617	-3	5
31	30	2219.5821	-3	5	32	31	2219.7035	6	5
33	32	2219.8235	-1	5	34	33	2219.9443	0	5
35	34	2220.0630	-23	10	36	35	2220.1860	-4	5
37	36	2220.3079	4	5	38	37	2220.4288	-1	5
39	38	2220.5495	-9	5	40	39	2220.6717	-2	5
41	40	2220.7943	7	5	42	41	2220.9150	-5	5
43	42	2221.0380	6	5	44	43	2221.1588	-7	5
46	45	2221.4049	9	10	47	46	2221.5225	-40	20
48	47	2221.6450	-41	20	49	48	2221.7659	-59	30
50	49	2221.8920	-27	10	51	50	2222.0154	-22	10
52	51	2222.1391	-16	10	53	52	2222.2623	-16	10
54	53	2222.3854	-17	10	55	54	2222.5109	3	5
56	55	2222.6328	-14	5	57	56	2222.7586	8	10
58	57	2222.8810	-6	5	59	58	2223.0057	2	5
60	59	2223.1272	-24	10					
ν_2 band									
80	81	1312.5708	-16	10	79	80	1312.7183	-7	5
78	79	1312.8646	-6	5	77	78	1313.0118	6	5
76	77	1313.1548	-18	10	75	76	1313.3017	0	5
74	75	1313.4465	1	5	72	73	1313.7346	-1	5
71	72	1313.8775	-8	5	70	71	1314.0220	6	5
69	70	1314.1635	-8	5	68	69	1314.3059	-8	5

† Observed minus calculated in units of 10^{-4} cm^{-1}.

‡ Uncertainty in line positions in units of 10^{-4} cm^{-1}.

Table C.2: *(Continued)*Observed line positions of ^{81}BrCNO in cm^{-1}.

J′	J″	Observed	O-C†	Δ‡	J′	J″	Observed	O-C†	Δ‡
67	68	1314.4484	-3	5	66	67	1314.5899	-4	5
65	66	1314.7319	3	5	64	65	1314.8733	8	5
63	64	1315.0139	8	5	62	63	1315.1542	10	5
61	62	1315.2933	4	5	60	61	1315.4327	4	5
59	60	1315.5711	-2	5	58	59	1315.7103	4	5
57	58	1315.8485	3	5	56	57	1315.9851	-10	5
55	56	1316.1230	-5	5	54	55	1316.2608	2	5
53	54	1316.3963	-10	5	52	53	1316.5341	5	5
51	52	1316.6682	-14	5	50	51	1316.8045	-7	5
49	50	1316.9388	-16	10	48	49	1317.0729	-23	10
46	47	1317.3420	-18	10	45	46	1317.4756	-19	10
44	45	1317.6106	-2	5	42	43	1317.8776	14	10
41	42	1318.0088	5	5	40	41	1318.1391	-10	5
39	40	1318.2701	-15	10	37	38	1318.5336	4	5
36	37	1318.6642	7	5	35	36	1318.7937	3	5
34	35	1318.9217	-12	5	33	34	1319.0531	10	5
32	33	1319.1806	-2	5	31	32	1319.3087	-4	5
30	31	1319.4367	-4	5	29	30	1319.5650	3	5
28	29	1319.6918	-2	5	27	28	1319.8192	3	5
26	27	1319.9457	4	5	25	26	1320.0721	7	5
24	25	1320.1977	6	5	23	24	1320.3228	3	5
22	23	1320.4462	-12	5	21	22	1320.5712	-7	5
20	21	1320.6954	-7	5	19	20	1320.8201	1	5
18	19	1320.9452	19	10	17	18	1321.0660	-4	5
16	17	1321.1881	-10	5	15	16	1321.3120	7	5
14	15	1321.4340	7	5	13	14	1321.5541	-7	5
12	13	1321.6750	-9	5	11	12	1321.7964	-3	5
10	11	1321.9157	-13	5	9	10	1322.0366	-5	5
8	9	1322.1553	-13	5	7	8	1322.2751	-8	5
6	7	1322.3946	-1	5	5	6	1322.5123	-9	5
4	5	1322.6323	10	5	3	4	1322.7497	7	5
2	3	1322.8642	-21	10	3	2	1323.5638	17	10
4	3	1323.6762	-5	5	5	4	1323.7885	-24	10

† Observed minus calculated in units of 10^{-4} cm^{-1}.

‡ Uncertainty in line positions in units of 10^{-4} cm^{-1}.

Table C.2: *(Continued)*Observed line positions of ^{81}BrCNO in cm^{-1}.

J′	J″	Observed	O-C†	Δ‡	J′	J″	Observed	O-C†	Δ‡
6	5	1323.9053	5	5	8	7	1324.1335	21	10
9	8	1324.2437	-3	5	10	9	1324.3565	1	5
11	10	1324.4667	-16	10	12	11	1324.5783	-15	10
13	12	1324.6905	-4	5	14	13	1324.8025	8	5
15	14	1324.9112	-9	5	17	16	1325.1324	7	5
18	17	1325.2416	7	5	19	18	1325.3501	4	5
20	19	1325.4574	-7	5	21	20	1325.5663	2	5
22	21	1325.6746	8	5	23	22	1325.7819	8	5
24	23	1325.8868	-12	5	25	24	1325.9953	9	5
26	25	1326.0998	-8	5	27	26	1326.2044	-19	10
28	27	1326.3114	-2	5	29	28	1326.4163	-2	5
30	29	1326.5224	15	10	31	30	1326.6252	1	5
32	31	1326.7299	11	5	33	32	1326.8320	-2	5
34	33	1326.9353	2	5	35	34	1327.0389	12	5
36	35	1327.1409	11	5	37	36	1327.2425	8	5
39	38	1327.4429	-11	5	40	39	1327.5452	6	5
41	40	1327.6446	-2	5	42	41	1327.7447	1	5
43	42	1327.8436	-4	5	44	43	1327.9429	0	5
45	44	1328.0407	-9	5	46	45	1328.1392	-5	5
47	46	1328.2364	-11	5	48	47	1328.3334	-15	10
49	48	1328.4323	4	5	50	49	1328.5286	1	5
51	50	1328.6243	-5	5	52	51	1328.7200	-6	5
53	52	1328.8171	11	5	54	53	1328.9120	10	5
55	54	1329.0063	8	5	56	55	1329.1003	5	5
57	56	1329.1939	4	5	58	57	1329.2862	-7	5
59	58	1329.3798	-1	5	60	59	1329.4712	-13	5
61	60	1329.5644	-3	5	62	61	1329.6571	7	5
63	62	1329.7481	3	5	64	63	1329.8383	-5	5
65	64	1329.9298	5	5	66	65	1330.0186	-8	5
67	66	1330.1087	-5	5	68	67	1330.1982	-3	5
69	68	1330.2876	2	5	71	70	1330.4632	-8	5
72	71	1330.5515	-2	5	73	72	1330.6397	8	5
74	73	1330.7254	-4	5	75	74	1330.8116	-6	5

† Observed minus calculated in units of 10^{-4} cm^{-1}.

‡ Uncertainty in line positions in units of 10^{-4} cm^{-1}.

Table C.2: *(Continued)*Observed line positions of ^{81}BrCNO in cm^{-1}.

J′	J″	Observed	O-C†	Δ‡	J′	J″	Observed	O-C†	Δ‡
76	75	1330.8984	1	5	77	76	1330.9837	-2	5
80	79	1331.2377	-7	5	81	80	1331.3219	-3	5
82	81	1331.4063	5	5	83	82	1331.4912	23	10
85	84	1331.6549	10	5	86	85	1331.7356	-2	5
87	86	1331.8164	-9	5	88	87	1331.8979	-4	5
89	88	1331.9770	-19	10	90	89	1332.0598	7	5
91	90	1332.1383	-6	5	92	91	1332.2193	10	5

† Observed minus calculated in units of 10^{-4} cm^{-1}.

‡ Uncertainty in line positions in units of 10^{-4} cm^{-1}.